High Intensity Organic Light-emitting Diodes

by

Xiangfei Qi

A dissertation submitted in partial fulfillment
of the requirements for the degree of
Doctor of Philosophy
(Physics)
in The University of Michigan
2012

Doctoral Committee:

Professor Stephen R. Forrest, Chair
Professor Rachel S. Goldman
Associate Professor Cagliyan Kurdak
Associate Professor Finn Larsen
Associate Professor Max Shtein

To my parents.

ACKNOWLEDGEMENTS

I dedicate my most sincere thanks to my advisor, Prof. Stephen Forrest, who has given me great guidance and support. In the past five years, he challenged my independent thinking, my scientific curiosity, and most important of all, my attitude to do meaningful scientific research. When I had to think about the value of a PhD, he has been the greatest encouragement over the course of time, which eventually turned out to be an invaluable journey of my life.

Prof. Mark Thompson and his group at the University of Southern California have provided the materials and valuable chemical fundamentals. Julie Brown from Universal Display Corp. has helped me with some insightful discussions. This work would not have been possible without collaborations with them. I also thank Josephine Li, Eva Ruff, and Christina Zigulis who have provided a tremendous amount of administrative support.

Working in OCM is a memory of a lifetime. Chris Giebink, Rhonda Salzman, Richard Lunt, Yifan Zhang, and Michael Slootsky are invaluable collaborators. I am thankful for many stimulating discussions with them. Xiaoran Tong, Celia Cunningham, Kyle Renshaw, Greg McGraw, Guodan Wei, Kuen-Ting Shiu, and Brian Lassiter have made OCM a fun environment to work in. Thank you all.

You look at where you are going and where you are and it never makes sense, but then you look back at where you've been and a pattern seems to emerge. –Robert M. Pirsig (Zen and the Art of Motorcycle Maintenance)

TABLE OF CONTENTS

LIST OF FIGURES

Figure

LIST OF TABLES

Table

LIST OF APPENDICES

Appendix

LIST OF ABBREVIATIONS

Alq_3 tris-(8-hydroxyquinoline)-aluminum

BCP 2,9-dimethyl-4,7-diphenyl-1,10-phenanthroline

BPhen 4,7-diphenyl-1,10-phenanthroline

CBP 4,4-N, N-dicarbazole-biphenyl

CIE Commission Internationale de L′Eclairage

CGL charge generation layer

CRI color rendering index

DCM2 2-methyl-6-[2,3,6,7-tetrahydro-1H,5H-benzo[ij](quinolizin-9-yl)ethenyl]-4H-pyran-4-ylidene] propane-dinitrile

DFT density function theory

EA electron affinity

EBL electron blocking layer

FEA finite element analysis

EL electroluminescent

EML emission layer

ETL electron transport layer

EQE External quantum efficiency

FIr6 bis-(4,6-difluorophenylpyridinato) tetrakis(1-pyrazolyl)borate

FPt2 [(2-(4′,6′-difluoro-phenyl)pyridinato-N,$C^{2'}$)Pt(2-thiopyridyl)]$_2$

FWHM full width at half maximum

HTL hole transport layer

HOMO highest occupied molecular orbital

IC internal conversion

IE ionization energy

IQE internal quantum efficiency

Ir(ppy)$_3$ tris (phenylpyridine) iridium

ISC intersystem crossing

^{3}LC ligand-centered triplet

LCD liquid crystal display

LEDs light-emitting diodes

LIG low-index grid

IPA isopropyl alcohol

IPES Inverse photoelectron spectroscopy

ITO indium tin oxide

LUMO lowest unoccupied molecular orbital

mCP N, N-dicarbazoly1-3,5-benzene

^{3}MLCT metal-ligand charge transfer triplet

^{3}MMLCT metal-metal-to-ligand charge transfer triplet

MoO_3 molybdenum trioxide

NPD 4,4-bis[N-(1-naphthyl)-N-phenyl-amino]-biphenyl

OLEDs organic light-emitting diodes

OVJP Organic vapor-jet printing

OVPD organic vapor phase deposition

PE power efficiency

PES Photoelectron spectroscopy

PHOLED electrophosphorescent OLEDs

PL Photoluminescence

PQIr Ir(III) bis-(2-phenylquinolyl-N,C2) acetylacetonate

PtOEP platinum(II) octaethylporphine

SOLED stacked organic light-emitting diode

SSL solid-state lighting

TCE 1,1,1-trichloroethane

TMO transition metal oxide

T-T triplet-triplet

UGH2 *p*-bis(triphenylsilyly)benzene

UPS ultraviolet photoelectron spectroscopy

V_2O_5 vanadium oxide

VTE vacuum thermal evaporation

WO_3 tungsten trioxide

WOLEDs White organic light-emitting devices

XPS X-ray photoelectron spectroscopy

ZFS Zero-field splitting

ABSTRACT

High Intensity Organic Light-emitting Diodes

by

Xiangfei Qi

Chair: Stephen Forrest

This thesis is dedicated to the fabrication, modeling, and characterization to achieve high efficiency organic light-emitting diodes (OLEDs) for illumination applications. Compared to conventional lighting sources, OLEDs enabled the direct conversion of electrical energy into light emission and have intrigued the world's lighting designers with the long-lasting, highly efficient illumination.

We begin with a brief overview of organic technology, from basic organic semiconductor physics, to its application in optoelectronics, i.e. light-emitting diodes, photovoltaics, photodetectors and thin-film transistors. Due to the importance of phosphorescent materials, we will focus on the photophysics of metal complexes that is central to high efficiency OLED technology, followed by a transient study to examine the radiative decay dynamics in a series of phosphorescent platinum binuclear complexes.

The major theme of this thesis is the design and optimization of a novel architecture where individual red, green and blue phosphorescent OLEDs are vertically stacked and electrically interconnected by the compound charge generation layers. We modeled carrier generation from the metal-oxide/doped organic interface based

on a thermally assisted tunneling mechanism. The model provides insights to the optimization of a stacked OLED from both electrical and optical point of view.

To realize the high intensity white lighting source, the efficient removal of heat is of a particular concern, especially in large-area devices. A fundamental transfer matrix analysis is introduced to predict the thermal properties in the devices. The analysis employs Laplace transforms to determine the response of the system to the combined effects of conduction, convection, and radiation. This perspective of constructing transmission matrices greatly facilitates the calculation of transient coupled heat transfer in a general multi-layer composite. It converts differential equations to algebraic forms, and can be expanded to study other thermal issues in more sophisticated structures.

CHAPTER I

Introduction to Organic Light-emitting Diodes

This chapter is an overview of lighting technology. Our purpose is to establish a foundation for the work that follows. To understand the operation of lighting systems, we start with a review on lighting metrics, followed by a brief review of solid-state lighting (SSL). Then we introduce the concept of conjugated small molecules and electron delocalization, which is one of the principal reasons for their exciting possibilities in electrical engineering research and applications. A selective introduction of active organic devices follows, and we conclude with a summary of a variety of commonly used processing techniques in this field.

1.1 Lighting: Metrics and Beyond

1.1.1 Lighting Metrics

Luminance is a photometric measure of the luminous intensity per unit area of light traveling in a given direction. It indicates how much luminous power will be perceived by an eye looking at the surface from a particular angle of view.[1] The SI unit for luminance is candela per square meter (cd/m^2), also called nits. A computer display typically emits 100 to 300 cd/m^2, and the sun has a luminance of about 1.6×10^9 cd/m^2 at noon. The perception of colors by cones in the retina requires at least several cd/m^2.[2]

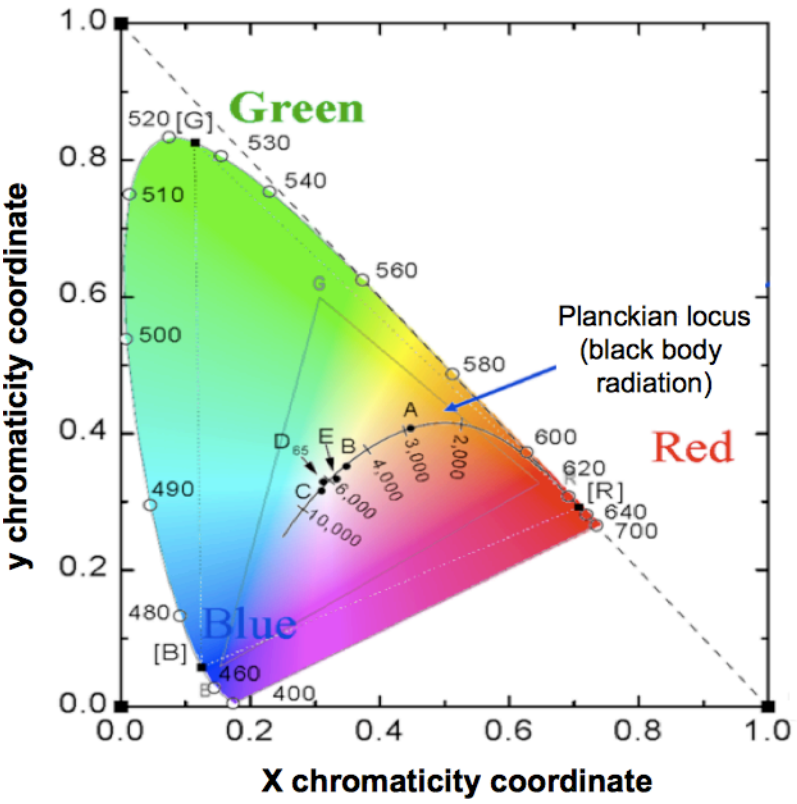

Figure 1.1: The CIE 1931 color space chromaticity diagram. Point A is tungsten at 2856K, B is direct sunlight at 4870K, C is overcast sunlight at 6770K, D65 is daylight at 6504K, and E marks equal energy. Adapted from A. Zukauskas, Introduction to Solid State Lighting, Wiley (2002).

Luminous efficacy is a measure of the efficiency with which the source provides visible light from electricity, i.e. the ratio of luminous flux to power. It is usually measured in lumens per watt (lm/W). An illumination source often uses light fixtures that come in a wide variety of styles for various functions. Luminous efficacy is an important property of light fixtures. Typical values are 10 to 18 lm/W for incandescent bulbs, and 35 to 60 lm/W for compact fluorescent lamps.[3]

Other than being bright and efficient, an illumination source is meant to approximate the blackbody solar spectrum, and needs to have a broad lineshape with roughly equal intensity across the entire visible spectrum.[4] Two matrics for color quality are the Commission Internationale de L′Eclairage (CIE) coordinates, and the color rendering index (CRI).[5]

The CIE 1931 XYZ color space was created by the International Commission on Illumination in 1931. This 3D color space is the basis for all color management systems. Shown in Figure 1.1, this color space represents the chromaticities visible to the average person, i.e. the human color gamut. The curved edge of the gamut is called the spectral locus, and corresponds to monochromatic light. If one chooses any two points of color on the chromaticity diagram, then all the colors that lie in a straight line between the two points can be formed by approximate mixing of these two colors. Figure 1.1 shows the color temperature for the Planck radiator from 2000K to 10000K. White is located at (0.33, 0.33), with typical color temperature of 5500K.[6]

The CRI is a quantitative measure of the ability of a light source to reproduce the appearance of different colors under illumination in comparison with a reference light source, such as an ideal black-body source with a defined CRI=100. Light sources with high CRI are desirable. Incandescent lamps have CRI approaching 100, indicating a perfect match to a black body, while fluorescent lamps typically have lower CRI in the range of 60 to 90. The CRI is evaluated by comparing the appearance of eight color samples which have relatively low color saturation, and are evenly distributed over the complete range of hues. The CRI rating of 100 means that the eight samples look exactly the same as they would under a black body radiator. However, an ideal light source for color rendering will have both a high CRI and a color temperature similar to that of the sun. For example, with a color temperature of only 2700K, it is impossible to distiguish between various hues of blue. The same can be said for lamps that exceed 6000K in color temperature as they are too weak at the red end of the spectrum, making reds and oranges appear too similar. The northern sky with a color temperature of about 7500K and a CRI=100 is not necessarily the ideal color rendering light source either. Table 1.1 summarizes the color temperature and CRI for some light sources.[7, 8]

Table 1.1: Examples of color temperature and CRI.

Light Source	Color Temperature	CRI
Candle	1700K	100
High Pressure Sodium	2100K	25
Incandescent	2700K	100
Tungsten Halogen	3200K	95
Natural Sunlight	5000-6000K	100

Figure 1.2: (Upper) Comparison of light sources with different CRI. A CRI of 70 and above is required for most lighting applications. Image Courtesy of Javier Ten. (Lower) Comparisons of varied color temperature.

1.1.2 Solid-state Lighting

Solid-state lighting (SSL) refers to the type of lighting that utilizes semiconductors to convert electricity into light, e.g. light-emitting diodes (LEDs), and OLEDs. Compared to traditional lighting technologies such as incandescent bulbs or fluorescent lamps, SSL differs fundamentally in terms of materials, drivers, system architecture, controls, and photometric properties. [9]

The LEDs are increasingly used in a variety of lighting applications due to their long life, energy savings, durability, compactness, and cool operation. They are gradually replacing incandescent bulbs in many applications, such as traffic lights and exit signs. Although SSL still costs more than incandescence at the point of purchase, the energy savings over the long term can be significant, along with reduction in carbon dioxide emissions. Ann Arbor, Michigan has been piloting LED street lights for the last several years. The initial installation will save the city over $100,000 per year in energy costs, and reduce annual greenhouse gas emissions by 267 tons.[10]

OLEDs are LEDs based on organic compounds. Compared to their inorganic counterpart, OLEDs are substantially cheaper, and have better color range and viewing angle. Shown in Figure 1.3, the flexibility of OLEDs introduces a variety of artistic lighting possibilities that emphasize their immense potential.

1.1.3 Organic Light-emitting Diodes

The first bilayer OLED was reported by Tang and Van Slyke in the late 1980s[11, 12], and an industry has formed around the continued development and commercialization of OLED technology since then. OLEDs have the promise to make an impact in lighting and full color display applications due to their high efficiency, long lifetime, as well as low-cost fabrication.[13]

For display applications, OLEDs have some markedly better properties compared to their liquid crystal display (LCD) counterparts.[14] OLED displays are thinner and

Figure 1.3: (Upper) Prototype bus stop featuring flexible OLED lighting. (Lower) Novaled and Philips OLED lighting designs.

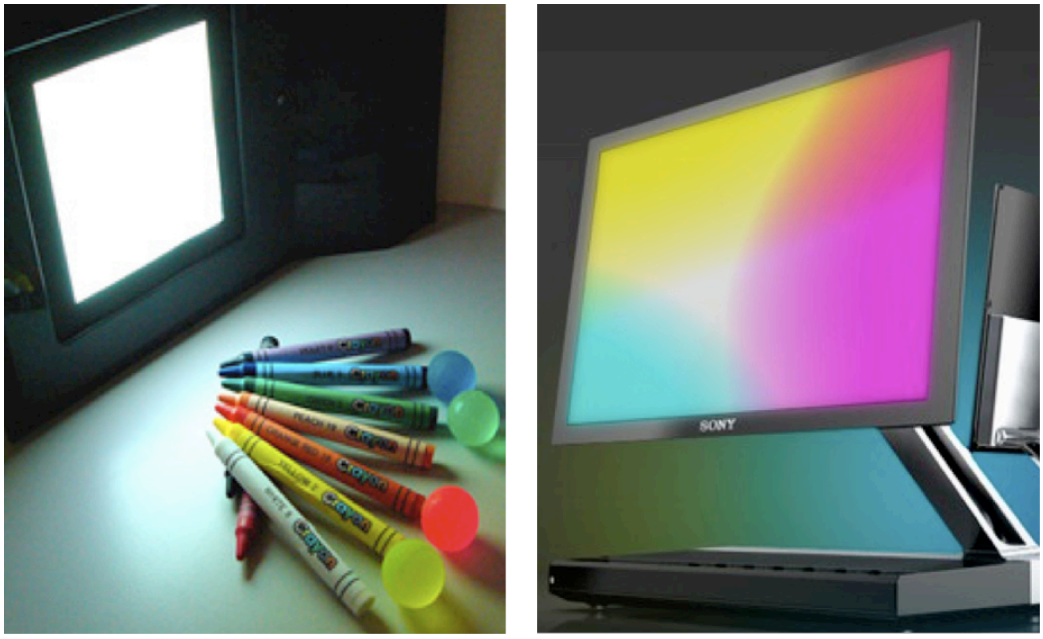

Figure 1.4: (Left) White OLED panel with decent CRI index. (right) A SONY OLED display showing saturated RGB pixels.

lighter, with wider viewing angles, and more saturated colors. Functioning without a backlight, they display deep black levels and can be more energy efficient than LCDs. In 2008, SONY introduced its 27-inch high-difinition display with 3-mm thickness, and a one-million-to-one contrast ratio.

The requirements for devices that serve as illumination sources are different than that for the monochromatic OLEDs targeted for RGB displays which give electroluminescent spectra with a relatively narrow lineshape centered around a peak wavelength. For lighting applications, OLEDs have high light quality, close to that of sunlight. OLED panels have the advantage of being a flat light source over a large area without the necessity of light distribution elements. OLEDs also have the potential to be more efficient than current energy-saving light bulbs. Figure 1.4 shows OLEDs that are used both as efficient white panels with high CRI and the SONY display with highly saturated RGB pixels.

There are two main families of OLEDs: one based on polymers and one that employs small molecules. While small molecules are often thermally evaporated (de-

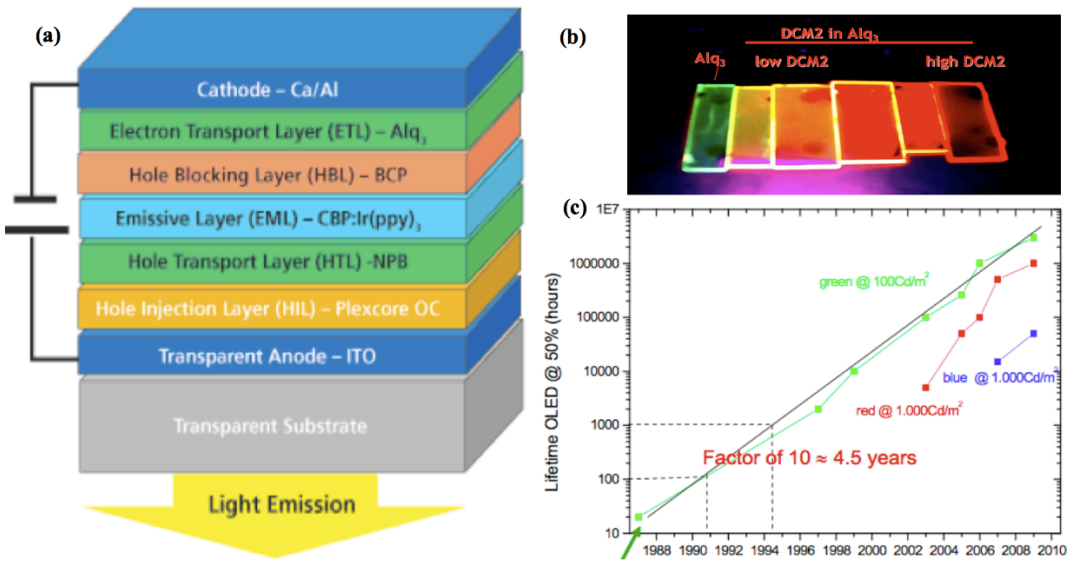

Figure 1.5: (a) Basic structure of OLEDs. (b) Solid State Solvation (Image courtesy of V. Bulovic). (c) The OLEDs lifetime progress since 1987.

tailed in Section 1.2.3), polymer molecules are too massive for this technique to be practical. Instead, the majority of conjugated polymer thin films are cast from a dilute solution, such as toluene or chloroform.[15] Since the film thickness depends on the solution concentration and spin speed, thickness control can be imprecise. We will focus on the fabrication and characterization of small molecule OLEDs in this thesis.

The basic OLED structure is shown in Figure 1.5(a). The device is frabricated on a glass substrate with a transparent bottom electrode of indium tin oxide (ITO) and a metal top electrode, with organic thin films sandwiched in between, i.e. a hole transport layer (HTL), a emission layer (EML), and a electron transport layer (ETL). When an appropriate voltage (typically a few volts) is applied to the device, the injected holes and electrons recombine in the EML, and emit light.[13] The structure of the organic layers and the choice of electrodes are designed to maximize the recombination process in the EML. Film thicknesses of 500$\mathring{A}$ or less lowers the voltage to between 5V and 10V for efficient charge carrier injection, which leads to exciton formation and ultimately emission as the exciton decays to the ground

state. Shortly after the introduction of thin film heterostructure based OLEDs, it was demonstrated that the host-dopant system with emitter molecules doped into a host matrix increases the device efficiency due to the improved level of charge recombination. The structure also helps exciton confinement and eliminates self-quenching of the emitting dopants. Figure 1.5(b) shows the spectral shift with increasing concentration of the 2-methyl-6-[2,3,6,7-tetrahydro-1H,5H-benzo[ij](quinolizin-9-yl)ethenyl]-4H-pyran-4-ylidene] propane-dinitrile (DCM2) suspended in a solid matrix of tris-(8-hydroxyquinoline)-aluminum (Alq_3). This is the energy shift due to self-polarization.[16] Figure 1.5(c) shows the OLEDs lifetime progress since 1987.

Phosphorescent OLEDs have higher internal efficiencies than their fluorescent counterparts.[17] Only about 25% of the excitonic energy generates light in fluorescent emission, with the remaining lost in the form of heat. For phosphorescent materials, up to 100% of the excitonic energy can be converted into light. This is up to four times more efficient than previously thought possible, enabling OLEDs to compete with LCDs as well as incandescent and fluorescent lighting. Figure 1.6 shows the chemical structure and electronic charge density of tris (phenylpyridine) iridium ($Ir(ppy)_3$), which is one of the complexes that possess chemically stable octahedral symmetry.[18]

1.2 Organic Optoelectronic Devices

Inorganic semiconductors, such as silicon and gallium arsenide, play a fundamental role in modern integrated circuits and microchips. Since the discovery of the first highly conducting polymer by Shirakawa, MacDiarmid and Heeger in 1977, organic semiconductors have generated entirely new physics for their application in molecular electronics.[19] Drastic improvements in synthesis and processing of organic semiconductors have been observed in the past two decades. Today, organic semiconductors are extensively used in the fabrication of solid-state devices, i.e. light-emitting

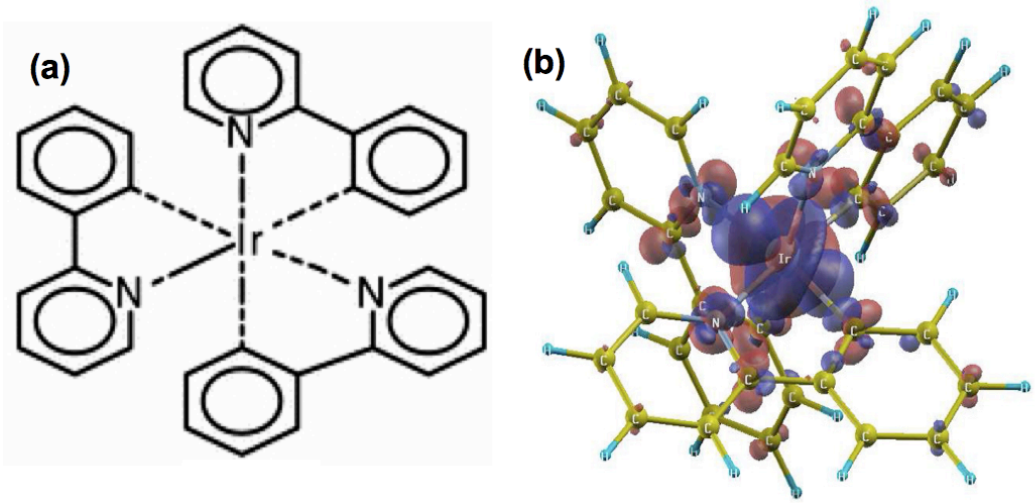

Figure 1.6: (a) Chemical structure and (b) Electronic charge density difference between the singlet excited state and the ground state of $Ir(ppy)_3$.

diodes, photovoltaic cells, photodetectors and transistors, etc. Distinctively different from their inorganic counterparts in the optical and electronic properties, they are also light in weight, mechanically flexible, allow for a wide variety of chemical modifications, and low-cost processing.[20, 21, 22] This section reviews the characteristics of two groups of organic semiconductors: small molecular weight materials mainly prepared by thermal evaporation, and polymers by solution processing. It is followed by a brief review of material purification and patterning techniques.

1.2.1 Conjugated Small Molecules

Organic molecules are defined to contain both carbon and hydrogen atoms. Their structural and functional diversity emerge from the versatility of the carbon atom, with its four valence electrons participating in covalent bonding, i.e. the overlapping of atomic orbitals for electrons to be shared by neighboring atoms. Different types of carbon-carbon bonds can be identified in three classes of hydrocarbons, namely alkanes, alkenes, and alkynes. Alkanes constitute the class of simple hydrocarbons with only carbon-carbon single bonds (C-C), which are also called σ-bonds. In σ-

bonding[23], the overlapping atomic orbitals lie directly between two nuclei. The other classes are alkenes with at least one double bond (C=C), and alkynes with one triple bond (C≡C).

Atomic bonding properties can be qualitatively described by orbital hybridization, which is created by the Valence Bond Theory.[24] For an isolated carbon, the $2s$, $2p_x$, $2p_y$, and $2p_z$ wave functions are used to describe the atomic orbitals, whose basic shapes are shown in Figure 1.7. For carbons joined in bonding, hybrid orbitals are employed to describe the electron movement in the valence shell. There are three important types of hybridizations: sp^3, sp^2, and sp, also shown in Figure 1.7. The primary aspect of sp^2 and sp hybridization is that they allow carbon atoms to form C=C and C≡C bonds. The C=C bond is formed with an sp^2 hybridized orbital and a p-orbital, while the C≡C bond is formed by an sp hybridized orbital and two p-orbitals from each atom.[25]

The π-bond involves the electrons in the leftover p-orbitals with the overlap occuring above and below the σ-bond. The combination of a σ-bond and a π-bond between the same two carbon atoms is a double bond. This double bond is stronger than the single covalent bond (611kJ/mol for C=C vs. 347kJ/mol for C-C) with shorter bond length ($1.33\mathring{A}$ for C=C vs. $1.53\mathring{A}$ for C-C), while C≡C is made up of one σ-bond and two π-bonds with bond strength of 839kJ/mol and a bond distance of $1.21\mathring{A}$. One important characteristic of both C=C and C≡C is restricted rotation between atoms since it requires a large amount of energy to break the π-bond. Figure 1.8 shows the electron arrangements in carbon-carbon single, double, and triple bonds. Here, ethane, ethylene, and acetylene represent the simplest forms of alkanes, alkenes, and alkynes, respectively. For C=C in the 3D model of ethylene, both the σ-bond and carbon atoms lie in a flat plane with the π-bond extending above and below.

Linear combination of atomic orbitals (LCAO) theory is commonly used to estimate the molecular orbitals that are formed upon bonding. The theory states that

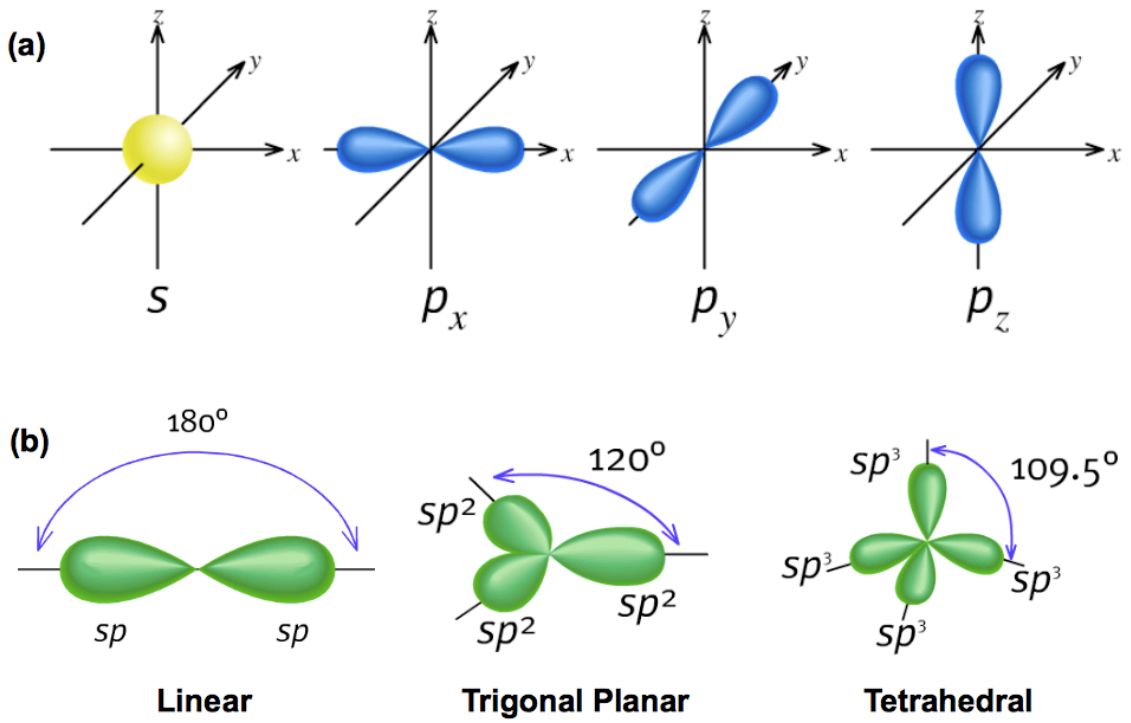

Figure 1.7: (a) Atomic s and p orbitals. (b) Shapes of the hybrid orbitals. Here two sp hybrid orbitals form a linear shape, three sp^2 orbitals in a trigonal planar structure, and four sp^3 orbitals in a tetrahedral structure.

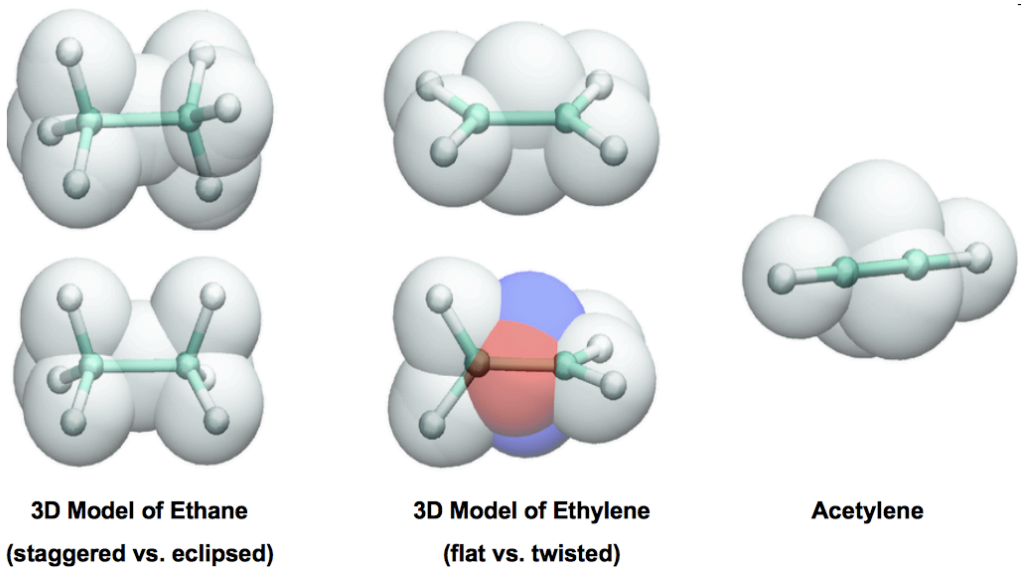

Figure 1.8: Scheme of electron arrangements C-C(left), C=C(middle), and C≡C (right). Rotation of C-C bond allows for two arrangements for ethane, while the twisted C=C bond requires the breaking of the π-bond in ethylene.

the *Schrödinger* equation for a molecular orbital can be constructed from the linear combinations of constituent atomic orbitals.[26] For simple diatomic molecules, the wavefunctions are represented mathematically by the equations:

$$\psi = c_1\psi_1 + c_2\psi_2 \tag{1.1a}$$

$$\psi^* = c_1\psi_1 - c_2\psi_2 \tag{1.1b}$$

where ψ and ψ^* are the molecular wavefunctions for the bonding and antibonding molecular orbitals, respectively, ψ_1 and ψ_2 are the atomic wavefunctions from atoms 1 and 2, respectively, and c_1 and c_2 are adjustable coefficients.

Depending on the energies and symmetries of the individual atomic orbitals, c_1 and c_2 can be positive or negative. Take hydrogen molecular formation for example: as the two atoms approach each other, their $1s$ atomic orbital overlap results in two molecular orbitals. One is a bonding orbital (σ) that concentrates in regions between the nuclei, and the other is an antibonding orbital (σ^*) that locates outside the region of the two nuclei. Antibonding orbitals (often labeled with an asterisk, *) are normally higher in energy than bonding orbitals. Similar rules are applied for π- and π^*-orbital.[25, 26] Note that only orbitals of matching symmetry can mix or interact.

A schematic molecular orbital diagram of ethylene is shown in Figure 1.9. Distinct σ and σ^* bonds are formed from sp^2 hybridization while π and π^* bonds from p_z hybridization.[27, 28] Here, the highest occupied molecular orbital (HOMO) and lowest unoccupied molecular orbital (LUMO), the so-called the frontier orbitals, are identified. The HOMO is the orbital that acts as the electron donor, while the LUMO is the electron acceptor, and the energy difference between the two is termed the energy gap.[23, 29]

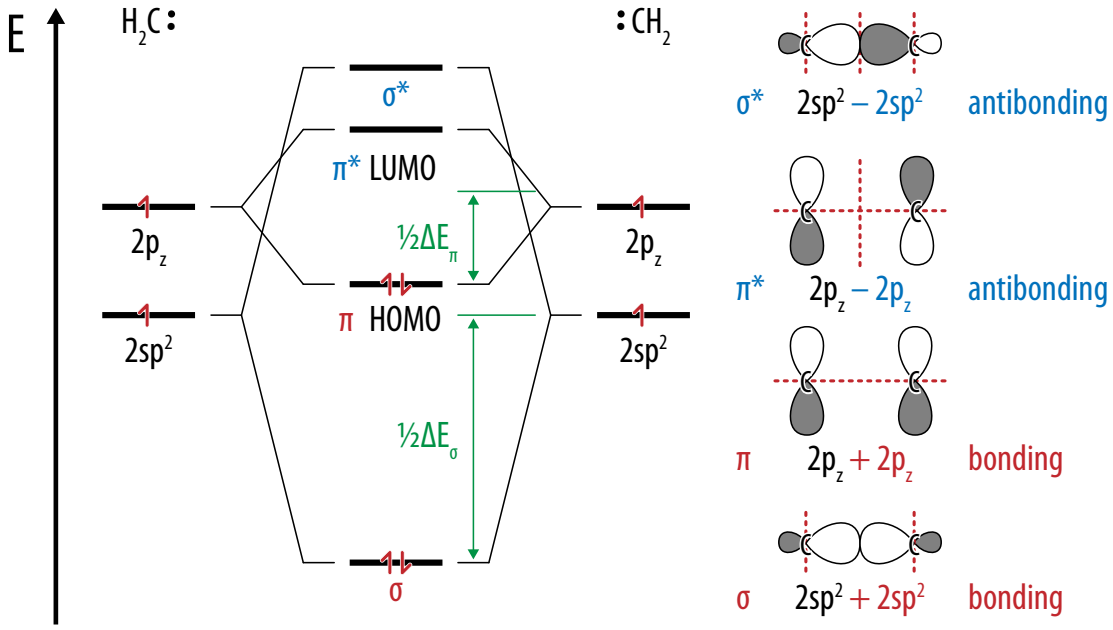

Figure 1.9: A schematic molecular orbital diagram of the ethylene molecule with distinct σ-bond(from sp^2) and π-bond(from p_z) with different bond energies.

The organic conjugated materials are reported to show remarkable optoelectronic properties. The presence of alternating π- and σ-bonds in a molecule is known as a conjugated system.[30, 31] Conjugation is also possible in other ways as long as each contiguous atom in a chain has an available p-orbital. Conjugated systems can extend across the entire molecule, or they can comprise only part of a molecule.

Shown in Figure 1.10, is the classic example of benzene with its system of six electrons above and below the planar ring. Electron delocalization in conjugated small molecules is responsible for electron conduction, with the electronic conductivity ($10^{-9} \sim 10^{3}\ \Omega^{-1}\mathrm{cm}^{-1}$) lying between that of metal and insulators. The gap between the HOMO and LUMO is typically 1.5 to 3.0eV, leading to strong absorption at or near the visible spectral range. The gap becomes smaller with increasing delocalization.

Besides electronic conductivity, high mobility is also required for most high performance organic semiconductors.[21, 22] Small molecules can be easily evaporated

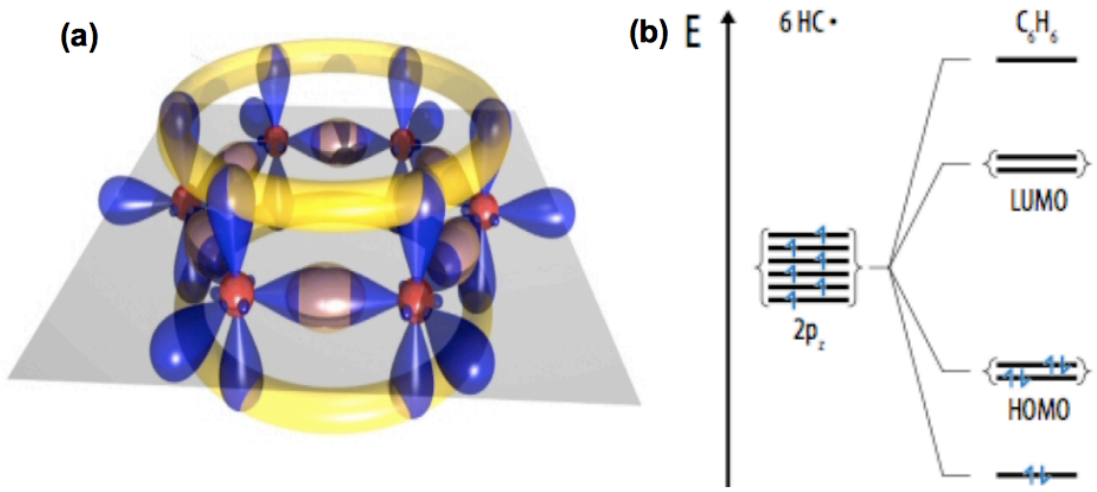

Figure 1.10: (a)Electronic and (b) energy structure of a benzene ring.

to form a polycrystalline film with mobility as high as $\sim 10^{-2}$cm^2/Vs, or amorphous film with mobilities $\sim 10^{-5}$cm^2/Vs at room temperature. Small molecules prepared as molecular single crystals have shown remarkable transport properties, with a mobility of 1 to 10 cm^2/Vs.[32] Conjugated polymers, commonly dissolved in solvents for low-cost fabrication, have generally lower mobility compared to small molecules. However, by varying the processing parameters, e.g. solution concentration, spin speed, and annealing methods, the packing of polymer chains can be altered and the electronic properties optimized. Most high performance polymers tend to have the long axes of the molecules oriented normal to the substrate surface with the typical grain size on the order of micrometers.

A material can be characterized by the long-range periodic configuration of atoms (crystalline structure), or by short-range ordering (amorphous structure), shown in Figure 1.11. The latter can form uniform thin films either by vapor deposition for small molecules and spin-coating methods for polymers.[33] Thermal evaporation is capable of growing continuous films with smooth interfaces and no pinholes, allowing vertical device feature sizes approaching molecular scales. Amorphous small molecules

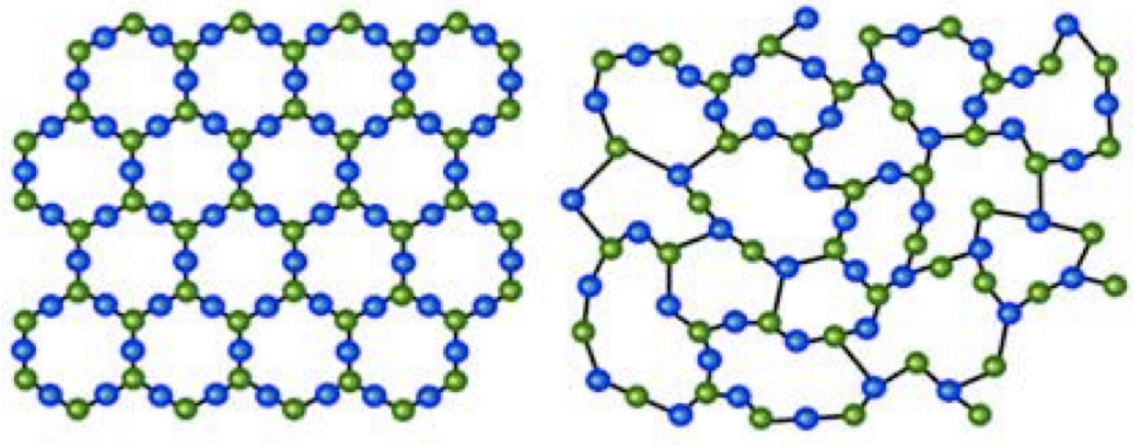

Figure 1.11: The structural difference between crystalline (left) and amorphous (right) structures. A crystalline structure has a periodic, long-range atomic ordering and an amorphous structure has no long-range atomic ordering.

have found their successful application in organic electroluminescent (EL) devices, e.g. photochromics, photovoltaics, and transistors, etc.[34]

In contrast to single crystals and liquid crystals which show anisotropic properties, amorphous small molecule films exhibit isotropic properties due to the absence of grain boundaries. In contrast to polymers, they are materials with well-defined molecular structures and definite molecular weights. Although disordered films possess inferior electron transport characteristics, they often satisfy the requirement for extremely thin, low voltage, organic devices. Moreover, their compatibility with flexible substrates promises low-cost processing. Flexible electronic devices (circuits, displays, and sensors) based on organic active materials will enable future generation of electronics products that will enter the mainstream electronics market.

1.2.2 Purifying Organic Materials

When organic semiconductors are tested in optoelectronic devices, their electronic properties are sensitive to small densities of impurities.[35] Experience has shown that the lifetime and yield of devices fabricated from low purity materials are poor.[35, 36]

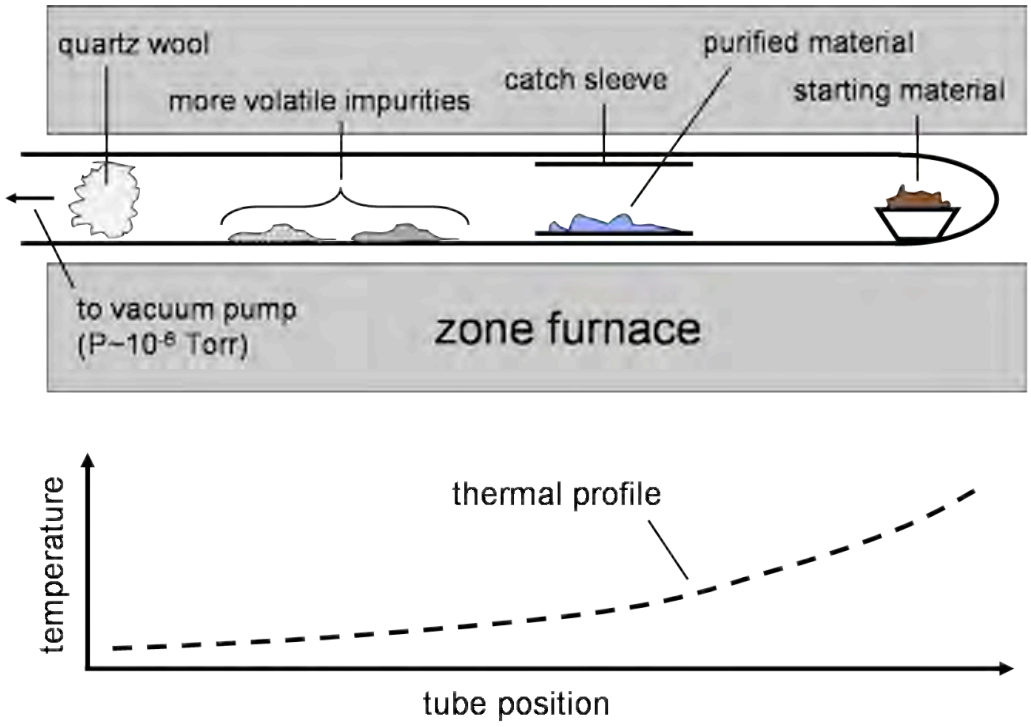

Figure 1.12: Schematic of gradient sublimation.[37]

Therefore, extensive purification is required to separate intrinsic from extrinsic effects. In our laboratory, we purify organic semiconductors that can be processed from the vapor phase using thermal gradient zone sublimation.[37]

This method is based on the fact that each material has its own particular sublimation point.[37] The idea is to heat the source material in a multiple zone furnace in vacuum for a given time, and retrieve the purified materials from a sliding tube in the middle zone. Shown in Figure 1.12, a cylindrical tube is maintained at a thermal gradient along its length. Being continuously evacuated, it contains the material which slowly sublimes and diffuses away from the hot zone. After recrystalization in a cooler zone, the high quality purified material is produced. A sub-ppm impurity level can be obtained by this technique, although this process is usually time-consuming with a cycle of weeks. Materials processed from solution are purified by multiple recrystallization processes.[38, 39]

1.2.3 Growth Techniques

Figure 1.13 illustrates the working mechanism of a thermal evaporator. High current flows through the boat containing small molecules, heating them to their sublimation temperature. High vacuum allows the vapor to reach the substrate without reacting with other atoms in the chamber, and reduces the incorporation of impurities from the residual gas in the chamber. A crystal monitor is mounted close to the substrate to estimate the quantity of material being deposited. The distance between the source and the substrate is far enough to prevent solid particles reaching the substrate.

With relative simplicity and high precision of layer thickness, typically within $\pm 5\mathring{A}$, vacuum thermal evaporation (VTE) is currently the most commonly used technique for the deposition of organic molecular solids.[37, 40] It allows for high degree of material purity and deposition control (film thickness, dopant concentration, etc.). However, control over large areas can be difficult using vacuum evaporation. In addition, a considerable fraction of the evaporant coats the cold walls of the deposition chamber, leading to low materials use efficiency and contamination of the system and substrate. The potential throughput for vacuum evaporated organic thin film devices is low, resulting in high production costs.

Sputtering is another high vacuum physical deposition process that relies on a plasma (high energy noble gas atoms, such as Argon) to release the source material. Shown in Figure 1.13, sputtering is performed in a vacuum chamber where the substrate is mounted on a negatively charged plate. The high energy ions induce atoms at the surface of the substrate to be ablated. These ablated atoms form a thin film coating after condensing on the substrate. This technique is especially useful for compounds or mixtures, such as ITO, where different components would otherwise tend to evaporate at different rates.

To avoid many of the drawbacks of VTE, an alternative method called organic

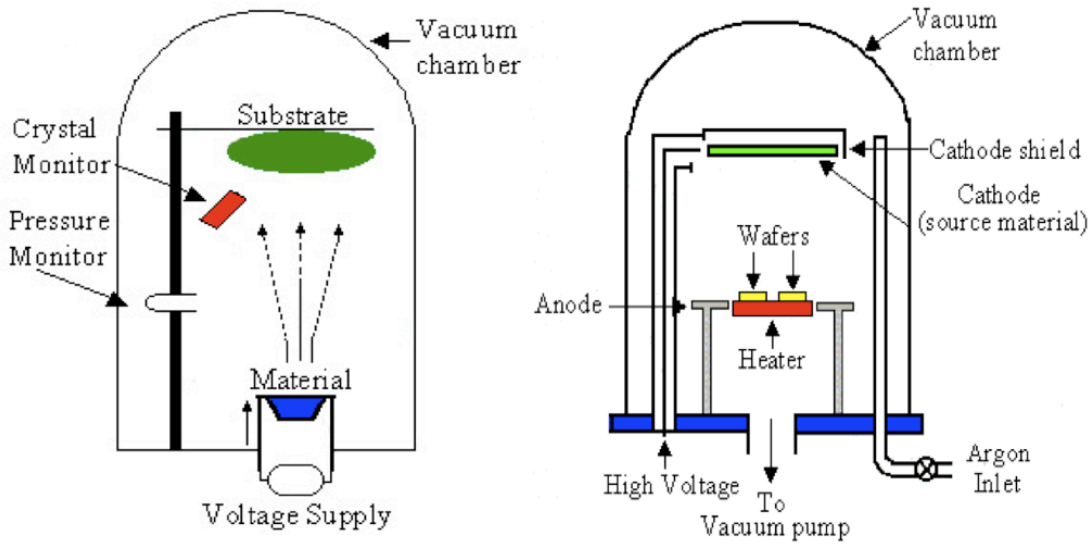

Figure 1.13: The process of VTE (left) and sputter (right) deposition.

vapor phase deposition (OVPD) has been introduced (Figure 1.14). This method significantly improves control over doping, and is adaptable to rapid and uniform deposition on large-area substrates.[41, 42] Organic compounds are thermally evaporated (at temperatures below 400^{o}C) into an inert carrier gas stream such as nitrogen, and then transported in a hot-walled reactor toward the substrate where condensation occurs. Flow patterns may be engineered to achieve a uniform distribution of organic vapors, resulting in a uniform coating thickness and minimized materials waste. This allows for positioning of evaporation sources outside of the reactor tube. By separating the functions of evaporation and transport, this technique leads to precise control over the deposition process.[43, 44] To grow doped films with uniform composition across the entire substrate area, the component streams are mixed prior to deposition.

Organic vapor-jet printing (OVJP) is a natural extension of OVPD. As an analog to ink-jet printing, the deposition of individual pixels on extended substrates and in close proximity can be achieved.[45, 46] Shown in Figure 1.14, the solvent is a hot inert carrier gas that vaporizes the organic source, creating a flow of volatilized molecules. These molecules are deposited through nozzle apertures to form organic patterns onto a cold substrate surface placed in close proximity (10$\sim$100μm) to the nozzle tip. The

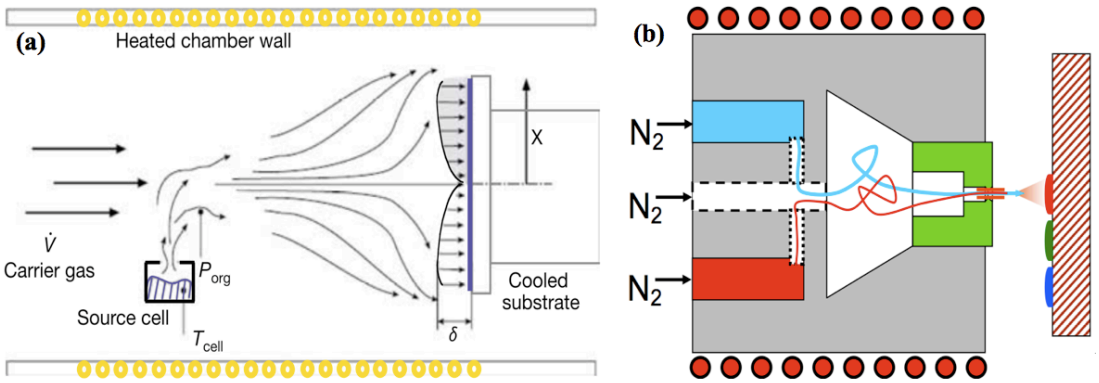

Figure 1.14: (a) Schematic of the OVPD process. (b) Schematic of the OVJP process.[44]

deposit resolution achievable by this method is determined by the distance from the nozzle to the substrate, the gas flow velocity, the background pressure, temperature, and the diameter of the orifice. This process has the possibility of revolutionizing the growth of small molecule organic thin films by rapidly and simply depositing nanometer scale organic thin film patterns.

1.2.4 Patterning Techniques

Patterning is fundamental to obtaining small features for the applications mentioned above. It is crucial in terms of device speed, power consumption, and low-cost manufacture. We will introduce the concepts of several lithography techniques, i.e. photolithography, electron beam lithography, and X-ray lithography, followed by cold welding as an example of non-lithography-based patterning.

Photolithography is a fundamental process in integrated microelectronic manufacture in which parts of a thin film are selectively removed from a substrate.[47] Fine lithographic patterns can be transferred to the substrate when light interacts with the light-sensitive chemical photoresist serving as a substrate mask, which is used to define the patterns on the exposed materials. Depending on the chemical composition, the photoresist can react in two ways: a positive resist becomes polymerized when exposed to the light while a negative resist has the reverse property. The devel-

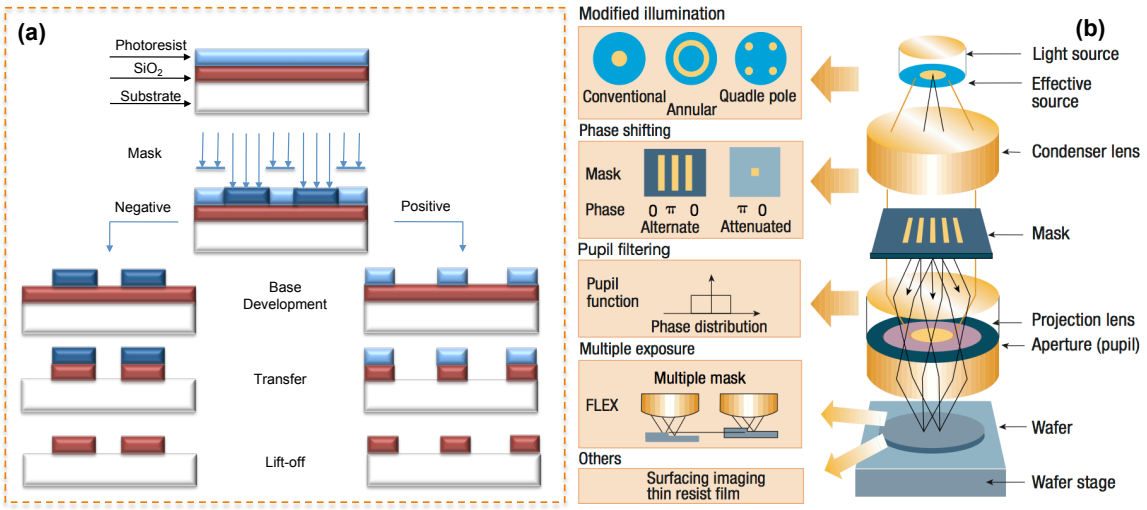

Figure 1.15: (a) Photolithography Process. (b) Schematic view of a typical exposure optical system. Resolution enhancement techniques may be applied at various points in the optical path.[49]

oping process decomposes the resist, followed by a post-bake process to harden the pattern and remove any residue of the developer. Figure 1.15 demonstrates the steps for positive and negative lithography.[48]

The resolution limit in this conventional projection optical lithography is determined largely by the well-known Rayleigh equation. The resolution, R, and the corresponding depth of focus are given by: [49]

$$R = k_1 \times \lambda / NA \tag{1.2a}$$

$$DOF = k_2 \times \lambda / NA^2 \tag{1.2b}$$

where λ is the exposure wavelength, NA is the numerical aperture of the optical system, and k_1 and k_2 are constants that depend on the specific resist material, process technology and image formation technique used. To obtain high resolutions, shorter wavelength light and lens systems with larger numerical apertures can be used. In general, the minimal feature size that can be obtained is almost the same as

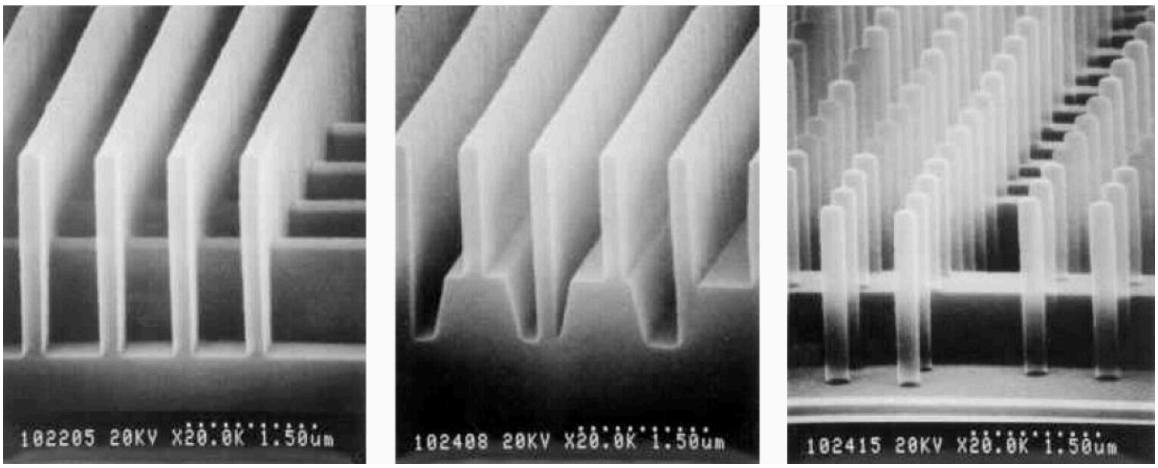

Figure 1.16: Resist patterns on different substrates with proximity X-ray lithography.[49]

the wavelength of light used for the exposure, for which one needs a relatively large numerical aperture (typically ≥ 0.5). Figure 1.15(b) shows a typical optical exposure system. Resolution enhancement techniques may be applied at various points in the optical path, as illustrated to the left of the figure.

Electron beam (e-beam) lithography uses a beam of electrons rather than photons as the exposure source.[50] The purpose is to create small structures in the resist that can be subsequently transferred to the substrate materials by etching. The primary advantage of e-beam lithography is the extremely high resolution combined with a large depth of focus. The key limitation of electron beam lithography is its low throughput, so this technique is used mainly in the production of masks, low-volume production of semiconductor components, and research and development. Several techniques have been developed to expand the throughput, such as making use of parallel exposure and ion beams. The microelectronics industry drive for ever smaller, faster and cheaper components, has rapidly pushed this technology to its limit.

X-ray lithography has a large range of wavelengths, from about 0.4nm to 100nm, with a resolution $\sim$1nm.[50] In the exposure system, X-rays are first collimated using a silicon carbide mirror, then passed through a transparent window of beryllium into

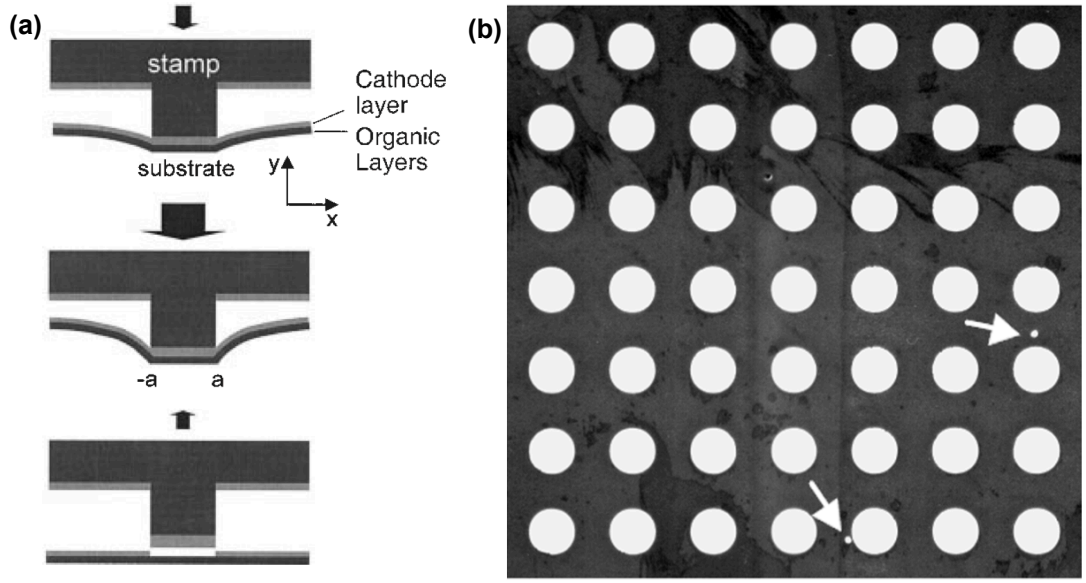

Figure 1.17: (a)Schematic illustration of the direct micro-patterning process by cold-welding followed by lift-off. (b) Optical micrograph of an array of 230-μm-diameter Mg:Ag contacts patterned by cold-welding followed by cathode life-off.[54]

a chamber containing the mask and wafer. The mask is prepared on a membrane of silicon carbide, and a layer of tantalum (patterned by direct-write electron-beam lithography) serves to absorb the X-rays and so generate the shadow on the semiconductor wafer. Figure 1.16 shows the resist patterns produced on different substrates using proximity X-ray lithography.

Other than the three lithographies introduced above, several other approaches have been proposed for delineating patterns at resolutions below 100nm, e.g. ultraviolet lithography[51], nano-imprint lithography[52], and near-field optical lithography[53], etc. Although such approaches are useful for producing individual nanostructures for the investigation of nanometre-scale devices, the throughput is too low for commercial application.

The cold-welding technique, demonstrated by Kim, is especially suitable for patterning flexible thin films for organic electronic devices.[54] Shown in Figure 1.17(a), selective lift-off of the metal cathode layer is achieved by pressing a pre-patterned,

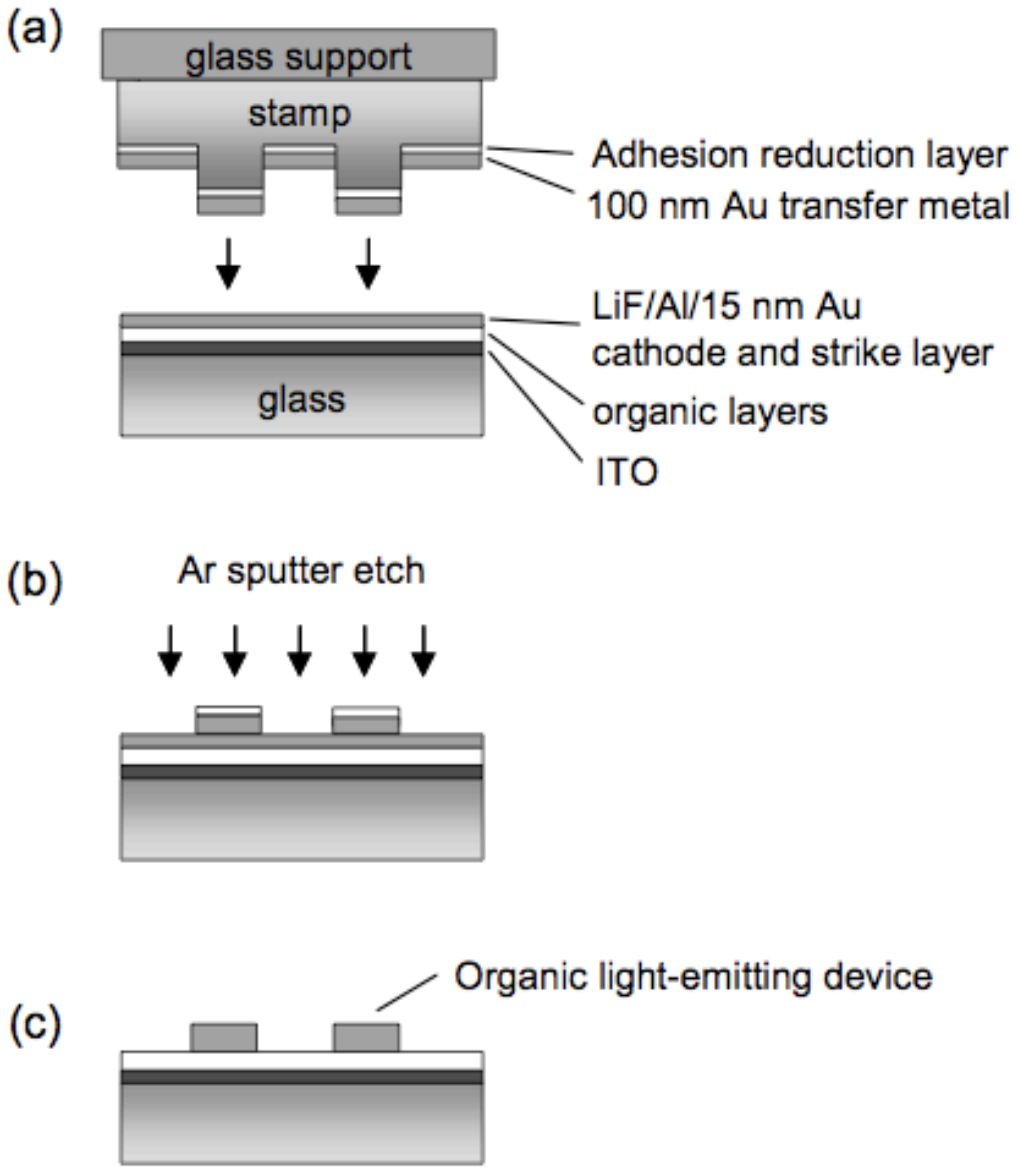

Figure 1.18: Schematic of additive cathode patterning process.[55]

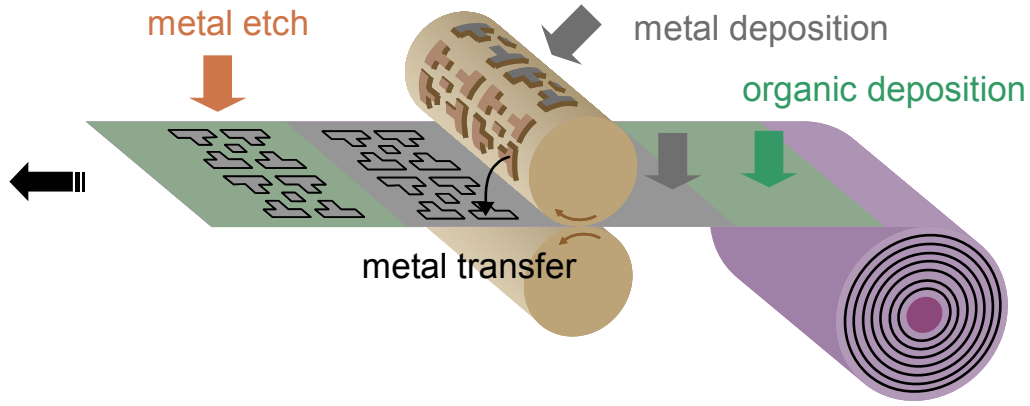

Figure 1.19: Schematic of a roll-to-roll process employing the additive cold-welding technique for the electrode patterning.[57]

metal-coated silicon stamp onto unpatterned device layers. Under pressure, the metal coating on the stamp cold-welds to the metal cathode coating. Subsequent separation of the stamp from the substrate removes the cathode metal in the regions contacted by the stamp, resulting in submicrometer feature definition. Figure 1.17(a) shows a patterned array of 230-μm-diameter dots and the edge of a 12-μm- wide stripe pattern, demonstrating a high yield. Cold-welding followed by lift-off of the cathode metal allows simple, cost-effective, and high-throughput large-area fabrication of organic electronic devices.

Similar formation of metallic bonds can be used in an analogous additive process.[56] A thin (about 10nm) metal "strike layer" is deposited on the substrate, and the stamp coated with a metal layer is pressed onto the substrate to transfer a metal pattern. When pressure is larger than the potential barrier at the surface, cold welding between the two contacting metal layers occurs and patterns are transferred. The following steps involve etching to remove the residual strike layer, etc. To ensure the success of the pattern transfer, adhesion between the metal layer and the stamp should be weaker than the interface adhesion at the substrate.

The cold-welding technique has several advantages over previously reported pat-

terning methods. First, it is cost-effective, since the stamps are reusable after the metal layers are removed by chemical dissolution. Second, this technique offers high throughput, since the entire electrode area of the circuit is patterned in a single step. Due to its capability for very high pattern resolution, this method is especially suitable for the fabrication of micro-displays. And finally, roll-to-roll fabrication processes that use flexible plastic substrates can employ this technique (Figure 1.19).[57]

CHAPTER II

Excitation in Organic Semiconductors: A Case Study

2.1 Molecular Electronic Structures

This chapter introduces the theoretical concepts needed for the work that follows. Starting with the Born-Oppenheimer (B-O) approximation, we give a review on the quantitative analysis of dynamic processes at the molecular level. Computation of molecular energy and wavefunctions for an archetype molecule will be discussed, followed with the energy transfer fundamentals. As an example, we provide a complete transient lifetime study on a set of binuclear compounds.

2.1.1 Born-Oppenheimer Approximation

Proposed by Max Born and J. Robert Oppenheimer in the 1920s, the B-O approximation simplifies the Schrödinger equation for a molecule, and introduces a mathematical description for the molecular orbitals.[26] First we write the Hamiltonian for the nuclei-electron systems as a sum of five terms:[58]

$$H = -\frac{1}{2}\sum_{A}\frac{\nabla_A^2}{M_A} - \frac{1}{2}\sum_{i}\frac{\nabla_i^2}{m_i} - \sum_{i,A}\frac{Z_A}{r_{iA}} + \frac{1}{2}\sum_{A\neq B}\frac{Z_A Z_B}{R_{AB}} + \frac{1}{2}\sum_{i\neq j}\frac{1}{r_{ij}} \tag{2.1}$$

where M_A and m_i are the nuclear and electron masses, respectively, Z_A and Z_B are the nuclei charge numbers, R_{AB}, r_{ij}, and r_{iA} refer to the relative nuclei-nuclei, electron-electron, and nuclei-electron distances, respectively. The first two Hamiltonian terms are for kinetic energy for each nucleus and electron in the system, followed by the Hamiltonian for the potential energy between the electron and nuclei, with the last two terms describing the potential energy arising from the Coulombic nuclei-nuclei and electron-electron repulsions, respectively.[58]

This approximation is based on the fact that the nucleus and electrons are attracted to each other with the same magnitude of momentum. Therefore, the nucleus has a velocity that is almost negligible due to its much larger mass in comparison to the electron. Since the nucleus is assumed to be stationary with electrons moving around it, the motion of the nuclei and the electrons can be solved with independent wavefunctions. Furthermore, the electron spin may be treated separately from the motion of both electrons and nuclei since spin is due to magnetic interactions, which are weak for most organic molecules. The B-O approximated molecular wavefunction, ψ, is therefore summarized as the product of the individual vibrational wavefunction, ψ_v, (depending on spatial coordinates of the nuclei), electronic wavefunction, ψ_e, and spin wavefunction, ψ_s:[31, 29]

$$\psi = \psi_v \psi_e \psi_s \tag{2.2}$$

This separation of the electronic and vibrational wavefunctions is the fundamental assumption of the Franck-Condon principle.

The Franck-Condon principle states that since electronic motions are much faster than nuclear motion, electronic transitions occur most favorably when the nuclear structure of the initial and final states are similar. Suppose an electron in a diatomic molecule makes a jump from one orbital to another as a result of some external perturbation such as absorption of light or an energetic collision. The transition

probability (P) between two electronic states of different nuclear configuration is:[29, 21]

$$\begin{aligned} P = \langle \psi' | \mu | \psi \rangle = \int \psi'^{\star} \mu \psi d\tau = \int \psi_v'^{\star} \psi_e'^{\star} \psi_s'^{\star} (\mu_e + \mu_N) \psi_v \psi_e \psi_s d\tau \\ = \int \psi_v'^{\star} \psi_v d\tau_n \int \psi_e'^{\star} \mu_e \psi_e d\tau_e \int \psi_s'^{\star} \psi_s d\tau_s \end{aligned} \tag{2.3}$$

where ψ and ψ' are the total wavefunctions of the initial and final state, respectively, μ is the molecular dipole operator determined by the charge and locations of the electrons and nuclei. Here $\int \psi_v'^{\star} \psi_v d\tau_n$ is the Franck-Condon factor–the selection rule for vibrational transitions. It states that a change from one vibrational energy level to another will be more likely to happen if the two vibrational wave functions overlap more significantly. The second integral $\int \psi_e'^{\star} \mu_e \psi_e d\tau_e$ contributes to the probability amplitude that determines the electronic spatial rule. If the equilibrium separation of the nuclei is the same in the initial (r_i) and final state (r_f), the transition may occur with no restriction with respect to nuclear motion. However, under the condition that $r_i \neq r_f$, the transition rate depends on the ability of the system to change its nuclear motion. The last integral $\int \psi_s'^{\star} \psi_s d\tau_s$ accounts for the probability amplitude for spin subject to spin selection rules.

Using the Franck-Condon principle, we are able to calculate the intensities of transitions between vibrational states of the electronic energy levels. This concludes that the conversion of electronic energy into vibrational energy may be the rate determining step in an electronic transition between states of different nuclear geometry.[29, 30]

2.1.2 Energy Structure Measurement

Photoelectron spectroscopy (PES) utilizes the kinetic energy distribution of the emitted photoelectrons to study the composition and electronic state of the surface region of a sample. There are two subdivisions according to the source of exciting radiation: X-ray photoelectron spectroscopy (XPS) and ultraviolet photoelectron

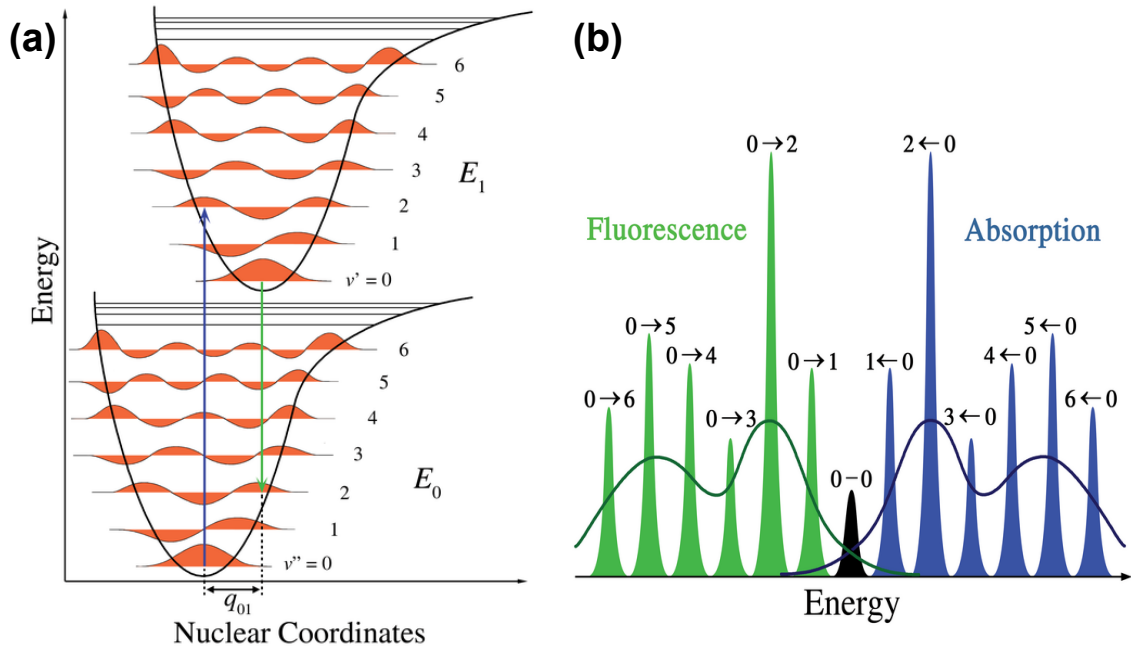

Figure 2.1: (a) Nuclear coordinates. (b) Electronic absorption and emission band. Mirror-image relationship arises between electronic absorption and emission bands.

spectroscopy (UPS).[59]

XPS uses soft X-rays with photon energy of 200∼2000eV. During the process, a photon is absorbed by an atom in a molecule or solid, leading to ionization and the emission of a core (inner shell) electron. By contrast, UPS uses vacuum UV radiation with a photon energy of 10 to 45eV. In UPS, the photon interacts with valence levels of the molecule or solid, leading to ionization by removal of one of these valence electrons. The kinetic energy distribution of the emitted photoelectrons (i.e. the number of emitted photoelectrons as a function of their kinetic energy) can be measured using any appropriate electron energy analyser and a photoelectron spectrum can thus be recorded.[60]

Inverse photoelectron spectroscopy (IPES) is used to study the unoccupied electronic structure of the thin film surfaces. A well-collimated beam of electrons directed at the sample, and these electrons couple to high-lying unoccupied electronic states

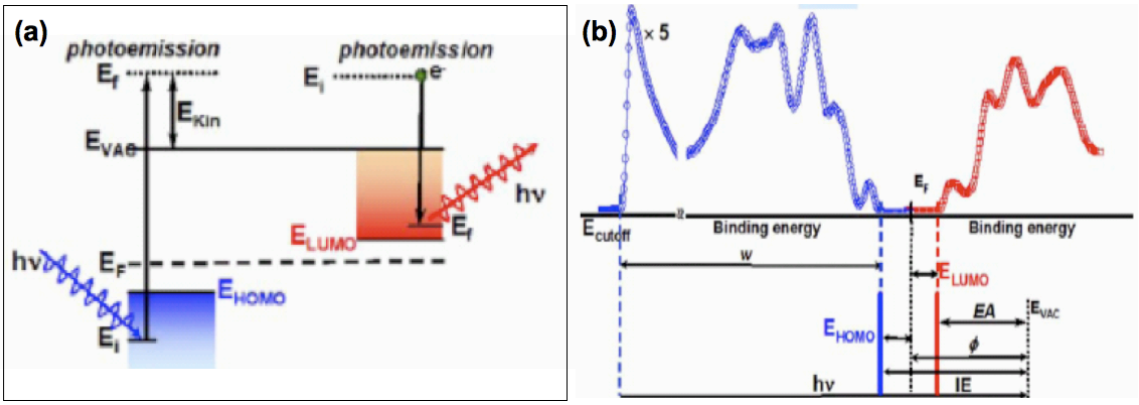

Figure 2.2: Principles of photoemission (blue) and inverse photoemission (red) with the corresponding electronic structure of an organic film.

and decay to low-lying unoccupied states with a subset of these transitions being radiative. The photons emitted in the decay process are detected and an energy spectrum (photon counts vs. incident electron energy) is generated.[60, 61] Due to the low energy of the incident electrons (typically $\leq$20eV), their penetration depth is only a few atomic layers, making inverse photoemission a particularly surface-sensitive technique. As inverse photoemission probes the electronic states above the Fermi energy of the system, it is a complementary technique to PES.

Figure 2.2 presents the fundamental parameters of organic films directly probed by photoemission characterization such as the HOMO, LUMO, electron affinity (EA), ionization energy (IE), and work function (ϕ), related to the Fermi level (E_F), and vacuum level (E_{VAC}). Here $h\nu$ is the energy of an incident photon involved in the photoemission process.[29]

2.2 Excited States of Organic Semiconductors

2.2.1 Singlets and Triplets

Consider two electrons in a chemical bond with spin vectors S_1 and S_2, quantized as $\pm\hbar/2$. The electron spins can be paired (antiparallel), or unpaired (parallel). If

two spins are antiparallel, the total spin is $S = S_1 + S_2 = 0$. In this case, the only allowed spin quantum number m_s is 0 ($|s, m_s\rangle = |0, 0\rangle$). This state remains a single state in the presence of an external magnetic field. It is termed a singlet state, S. However, if two spins are parallel, the total spin has a magnitude of $\hbar$ with possible m_s=0, ± 1 ($|s, m_s\rangle = |1, 1\rangle$, $|1, 0\rangle$, and $|1, -1\rangle$).[62] This state possesses a net spin magnetic moment and splits into three quantized states under an external magnetic field. It is termed as triplet state, T, indicating a threefold degeneracy of the state. To sum up, we have:[63, 64]

$$s = 0 \qquad |0, 0\rangle = \frac{1}{\sqrt{2}}(\uparrow\downarrow - \downarrow\uparrow) \tag{2.4}$$

$$\begin{aligned} s = 1 \qquad |1, 1\rangle &= \uparrow\uparrow \\ |1, 0\rangle &= \frac{1}{\sqrt{2}}(\uparrow\downarrow + \downarrow\uparrow) \\ |1, -1\rangle &= \downarrow\downarrow \end{aligned} \tag{2.5}$$

The results are visualized in Figure 2.3.

According to the valence bond theory, the symmetric spatial wavefunction has a slightly lower energy than the antisymmetric state. Therefore, the ground state is a singlet (S_0). From the selection rule, the first excited singlet state (S_1) is realized by exciting one of the $1s$ states to a $2s$ state, while the first excited triplet state (T_1) is formed by promoting the spatial wavefunction from symmetric to antisymmetric in the $1s$ orbital. In general, T_1 is lower in energy than S_1.

Due to conservation of angular momentum, absorption of a photon cannot change the spin state from a singlet to a triplet. Hence, absorption of a singlet ground state will yield a singlet excited state. Direct formation of a triplet is a very improbable process since both the orbit and spin of the electron would have to change simultaneously. Generally, singlet excited states decay quickly back to the ground state

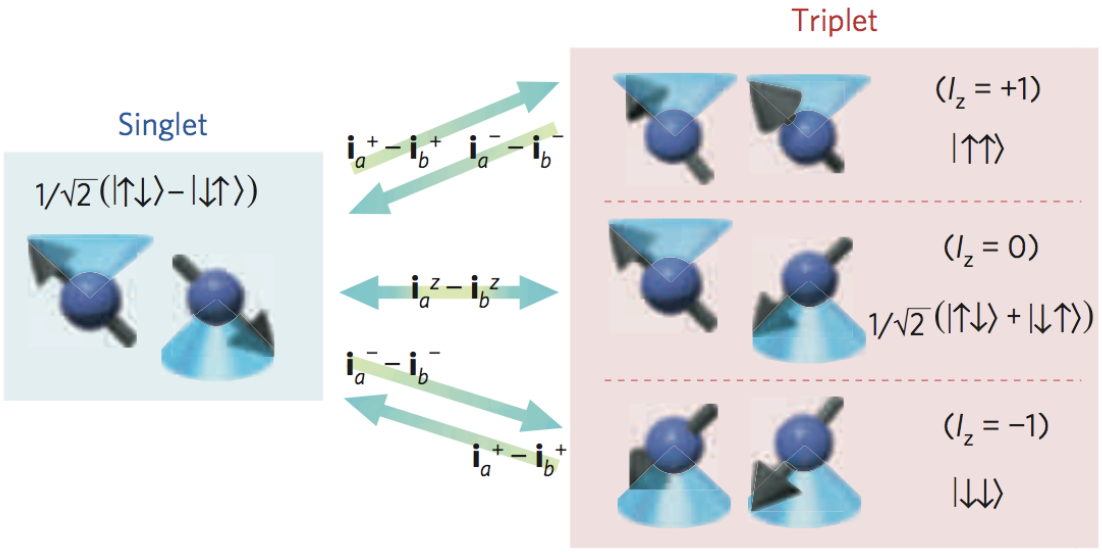

Figure 2.3: Schematics of the singlet and triplet states of two identical spin 1/2.[62]

($10^{-9} \sim 10^{-7}$ seconds), although the resulting vibrational or rotational state might be different. This process is known as fluoresence. On occasion, the singlet excited state can become a triplet state via intersystem crossing. Once in the triplet excited state, decay back to the ground state turns out to be quite slow ($10^{-3} \sim 10^{-2}$ seconds), known as phorphoresence.[65]

Figure 2.4 shows the Jablonski diagram that illustrates the electronic states of a molecule and the transitions between them. There are three significant non-radiative processes: internal conversion (IC), intersystem crossing (ISC) and vibrational relaxation. The process, IC, occurs when a vibrational state of an electronically excited state couples to a vibrational state of a lower electronic state. This is the radiationless transition between energy states of the same spin. On the contrary, ISC is a transition to a state with a different spin multiplicity. ISC is much more important in molecules with larger spin-orbit coupling since this type of nonradiative transition gives rise to phosphorescence. The third type, vibrational relaxation, is the most common of the three. It occurs very quickly ($10^{-14} \sim 10^{-11}$ seconds) and is enhanced

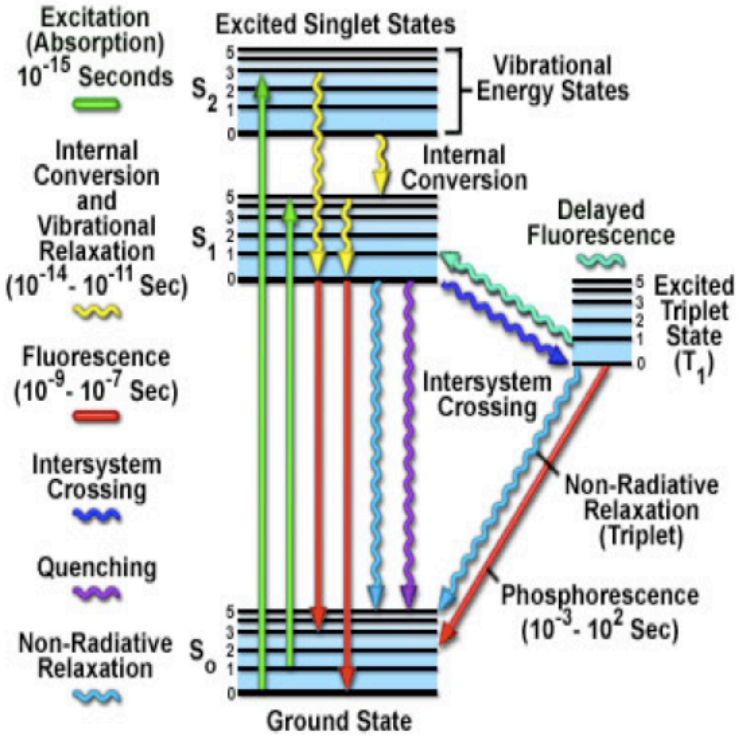

Figure 2.4: Jablonski Energy Diagram. The states are arranged vertically by energy and grouped horizontally by spin multiplicity. Here, straight arrows indicate radiative transitions and squiggly arrows indicate non-radiative transitions. Higher vibrational states are indicated with thiner lines compared to the vibrational ground states.

by physical contact of an excited molecule with other particles with which energy can be transferred through collisions.[29, 66]

2.2.2 Excitons

Excitons are electronically neural quasi-particles consisting of a bound electron and hole pair. An exciton forms when a photon is absorbed by a semiconductor. This excites an electron from the valence band into the conduction band, leaving behind a localized positively charged hole. The electron and hole are stabilized by the Coulomb force. Excitons mediate the absorption and emission of light, particularly in disordered and low-dimensional materials, i.e. it is the migration quantum of electronic energy.[67]

There are three types of excitons: Wannier-Mott excitons, Frenkel excitons, and charge-transfer (CT) excitons. Wannier-Mott excitons typically have radii larger than the lattice spacings. As a result, the binding energy is on the order of 0.01eV. Such a weak binding energy explains the ease of charge separation in a silicon p-n junction where the built-in electric field is large enough to dissociate any light-produced excitons. In contrast, for a material with small dielectric constant, the Coulomb interaction between electron and hole is strong and the excitons tend to be small, of the same order as the size of the unit cell. Frenkel excitons are localized in a single molecule, with typical binding energies in the range of 0.1 to 1.0eV. In comparison, CT excitons have the electron and hole component on adjacent molecules.[68, 69]

Once excitons are created in the organic semiconductor, the excitons will diffuse before their energy is released along radiative or non-radiative pathways. However, the diffusion of the exciton is accompanied by an energy transfer between molecules. Efficient energy transfer is required for the modification of emission properties in phosphorescent OLEDs.

We now look at the exciton energy transfer from the host molecules to the dopants

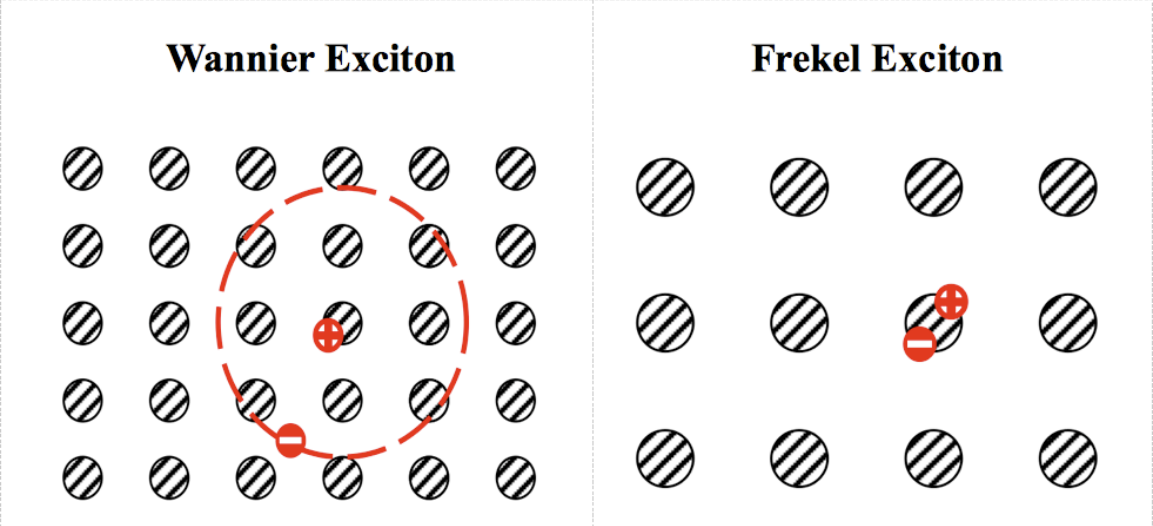

Figure 2.5: Wannier Excitons and Frenkel Excitons.

in the host-guest matrix. Energy transfer occurs in three different ways: (i) Förster type energy transfer, (ii) Dexter type energy transfer, and (iii) trap-assisted carrier recombination. In general, the probability of energy transfer can be described by the Fermi Golden Rule, shown in Equation 2.6.[64]

$$\text{Probability}\,(D^*A \rightarrow DA^*) = (2\pi/h)|H|^2\rho, \tag{2.6}$$

where D^* is an excited state donor and A is a ground state acceptor. Here, the Hamiltonian operator, H, describes the specific type of system perturbation occurring between the initial state (D^*A) and the final state (DA^*), and ρ is the density of the final state at the energy of the initial state.[21]

Förster transfer arises from dipole-dipole interaction between the electronic states of the donor and the acceptor. Transfer occurs when the oscillations of an optically induced electronic coherence on the donor are resonant with the electronic energy gap of the acceptor.[70] The strength of the interaction depends on the magnitude of transition dipole interaction, which depends on the magnitude of the donor and acceptor transition matrix elements, and the alignment and separation of the dipoles.

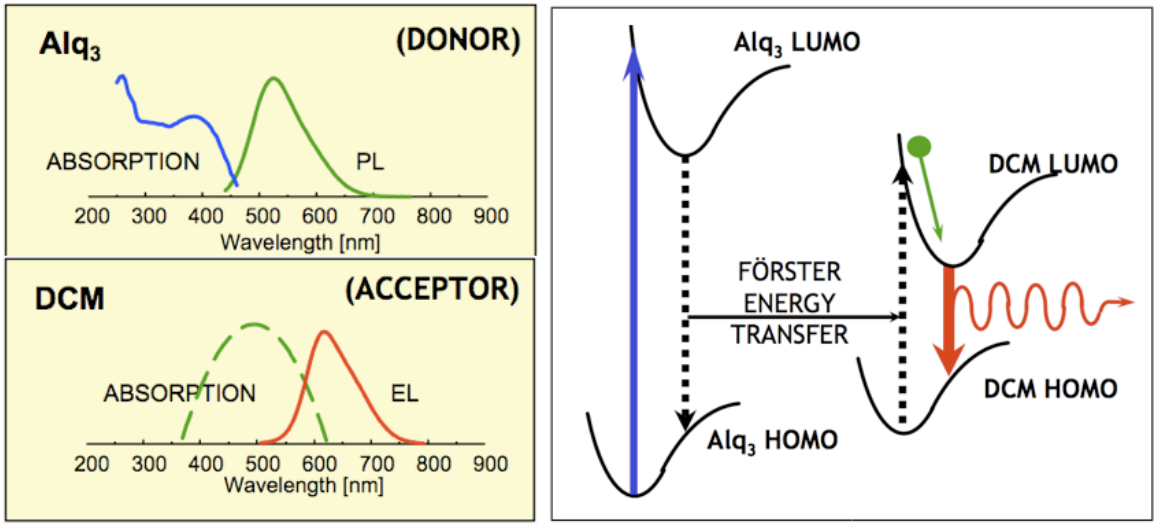

Figure 2.6: (a) Absorption and photoluminescence of Alq_3 and DCM. (b)Diagram for Forster transfer between Alq_3 and DCM (Image courtesy of V. Bulovic).

Förster showed the following dependence of the rate of transfer:

$$k_{ET} = (2\pi/\hbar)| < D, A^*|H_{DA}|D^*, A > |^2 \int g_D(E)g_A(E)dE = k_D(R_0/R)^6 \qquad (2.7)$$

where, k_{ET} is the rate of the energy transfer, k_D is the decay rate of the donor, R is the distance between the donor and acceptor, and R_0 is what is known as the critical transfer distance, and is related to the spectral overlap of the donor emission with the ground state absorption of the acceptor. For efficient transfer, donor emission and acceptor absorption must overlap. The R^{-6} dependence on distance is often used in spectroscopic characterization of the proximity of donor and acceptor.

Energy transfer via the dipole-induced mechanism primarily depends on the magnitude of the spectral overlap integral as shown in Figure 2.6. Hence, the singlet-singlet transition is the only process that is viable by this mechanism. Since the oscillator strength and therefore the molar absorbability of S→T transition is normally not significant, the magnitude of the overlap integral is usually vanishingly small, making triplet-triplet transitions by this mechanism inefficient.

Dexter transfer is a non-radiative energy transfer by the exchange interaction which occurs as a result of the overlap of the wave functions of the donor and the acceptor.[71] The transfer process has been described as electron tunneling, where one electron moves from the excited donor LUMO to the acceptor LUMO while simultaneously an electron moves from the acceptor HOMO to the donor HOMO. This is a very short range process since it requires the overlap of the wavefunctions of the energy of the two species. In Dexter's model, the interaction strength decreases exponentially as a function of distance:

$$k_{ET} = \frac{2\pi}{\hbar} K J e^{-2R_{DA}/L} \tag{2.8}$$

where K is related to specific orbital interactions, J is the normalized spectral overlap integral, R_{DA} is the donor-acceptor separation relative to their van der Waals radii, and L depends on the system under consideration. Dexter energy transfer is insignificant beyond a separation distance of $10\mathring{A}$ between the donor and the acceptor due to the exponential (tunneling) term.

2.2.3 Excimers and Exciplexes

In certain cases, two or more molecules may participate in cooperative absorption or emission. An absorption complex exists when two molecules act cooperatively to absorb a photon. And an *exciplex* exists if two molecules act cooperatively to emit a photon.[72, 73] In the special case that components of the complex are of the same type, the excited molecular complex is termed an *excimer*.[74]

An electronically excited state may be a polarizable species and may participate in charge-transfer interactions with other polar or polarizable species because of the occurrence of an electrophilic half-filled highest occupied orbital and a nucleophilic half-filled lowest unoccupied orbital. As a result, a collision complex between an electronically excited species, M^*, with any polar or polarizable ground state molecule,

N, will generally be stabilized by some charge-transfer interaction.

$$M^* + N \rightarrow M \leftrightsquigarrow N(\text{exciplex}) \tag{2.9a}$$

$$M^* + M \rightarrow M \leftrightsquigarrow M(\text{excimer}) \tag{2.9b}$$

2.3 Binuclear Compounds: A Case Study

Transient studies can be used to examine the radiative decay dynamics in a series of phosphorescent platinum binuclear complexes. The complexes studied in our work consist of square planar (2-(4′ ,6′-difiuoro-phenyl) pyridinato-N, $C^{2'}$)Pt units bridged by either pyrazole or thiopyridine ligands. We observe an increase in radiative lifetime as temperature is reduced from 300 K to 4 K when the binuclear complexes, named **1**, **2**, and **3**, (see Figure 2.7), with Pt-Pt spacings 3.19$\mathring{A}$, 3.05$\mathring{A}$, and 2.83$\mathring{A}$, respectively, are doped into a *p*-bis(triphenylsilyly)benzene (UGH2) wide energy gap host. The lifetimes for 1, 2, and 3 are $\tau = (6.3 \pm 0.1)\mu$s, $\tau = (2.3 \pm 0.1)\mu$s, and $\tau = (2.0 \pm 0.1)\mu$s at T= 295K, respectively. At T=4K, those values increase to $\tau = (8.6 \pm 0.1)\mu$s, $\tau = (14.4 \pm 0.1)\mu$s, and $\tau = (17.0 \pm 0.1)\mu$s, suggesting that the neighboring heavy metal centers in compounds **2**, and **3** have significant orbital overlap. A three-level zero-field splitting model yields the lowest triplet energy splittings of (28±3)cm^{-1}, (142±9)cm^{-1}, and (113±10)cm^{-1} for compounds **1**, **2**, and **3**, respectively.

2.3.1 Structures

Spin-orbit coupling between singlet and triplet states in organic molecules is known to be an effective means to promote rapid, radiative triplet emission. When this process is electrically excited, it results in electrophosphorescent emission in OLEDs, leading to unity internal quantum efficiency[17]. The typically slow ($\ll 10^{-6}$s) and inefficient, room-temperature phosphorescence in organic molecules is enhanced by

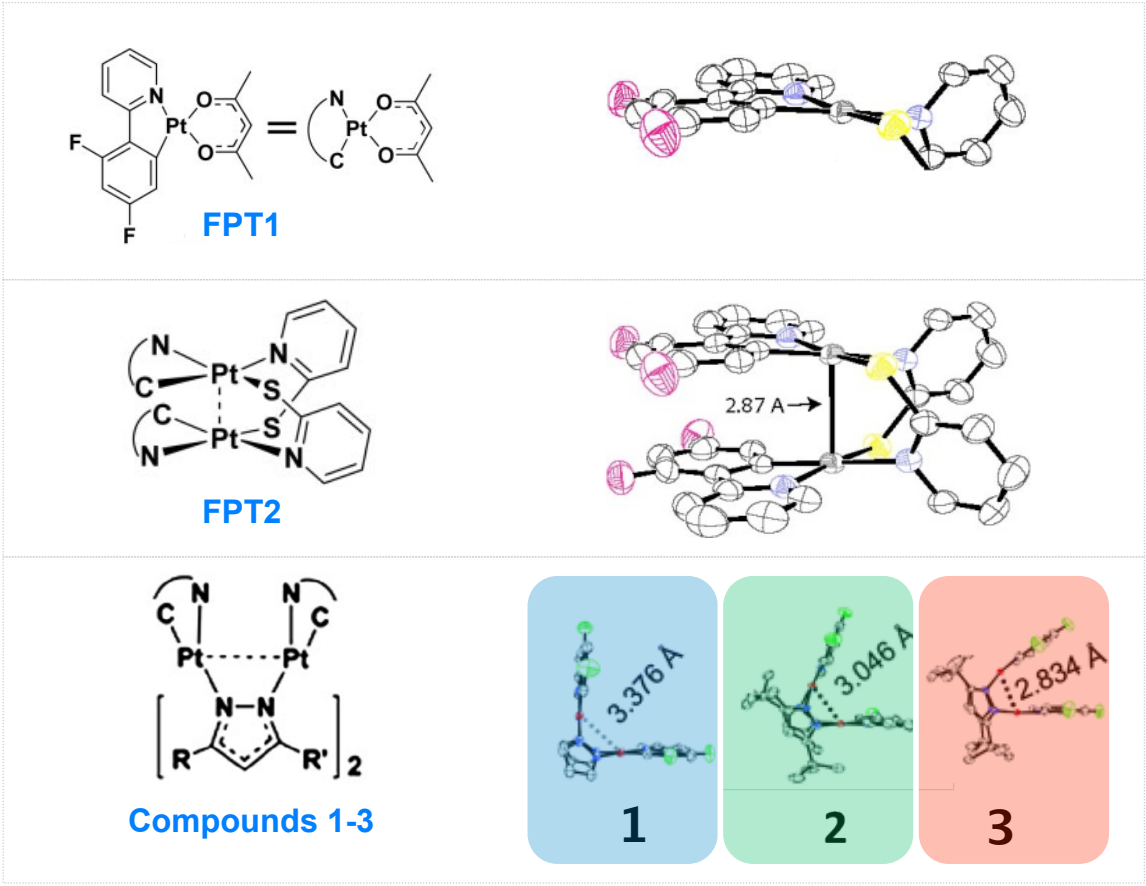

Figure 2.7: The structures of FPt1, FPt2, and binuclear complexes **1**, **2**, **3**.

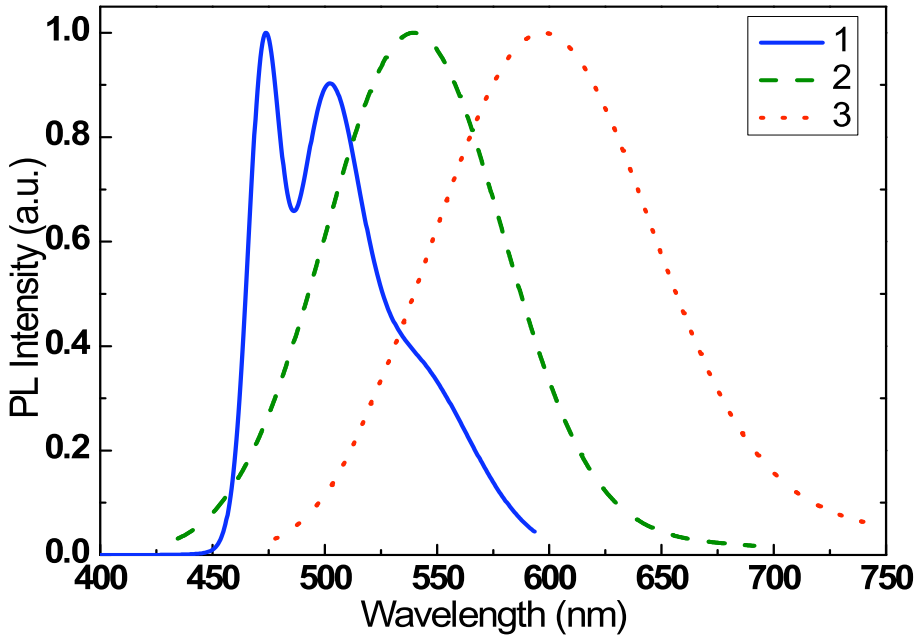

Figure 2.8: Phosphorescent spectra of compounds **1** (solid line), **2** (dotted line), and **3** (dashed line) at room temperature (T = 295 K). Compounds emit blue, green, and red light, respectively.

introducing a heavy metal atom in the molecular complex [67]. The magnitude of the spin-orbit interaction by the presence of the heavy metal atom with atomic number Z, scales as Z^4. The first efficient electrophosphorescent OLED was based on platinum(II) octaethylporphine (PtOEP) [65], whose emissive state is a mixture of ligand-centered triplet (^{3}LC) and metal-ligand charge transfer triplet (^{3}MLCT) states. A number of other square planar platinum complexes have also been utilized in OLEDs, emitting from a similar mixture of ^{3}MLCT and ^{3}LC states [75, 76, 77]. A related class of phosphors is comprised of the binuclear Pt complexes, where the emissive state arises from charge transfer involving the metal-metal-to-ligand charge transfer triplet (^{3}MMLCT) interaction. The photophysical properties of this latter class of materials are explored in this work as a function of the Pt-Pt spacing.

Recently, Ma *et al.* reported a series of phosphorescent pyrazolate-bridged cyclometalated platinum(II) complexes [78] with the formula: C^NPt $(\mu - pz)_2$PtC^N. Similar structures for binuclear Pt(II) and Ir(III) have also been previously reported [79]. The pyrazolate ligand can be used to control the degree of metal-metal interaction by adjusting the angle between opposing ligands, and thus the emission spectra. For example, compounds **1**, **2**, and **3** in Figure 2.7 (a) with Pt-Pt spacings (**1**) 3.19Å, (**2**) 3.05Å, and (**3**) 2.83Å, lead to efficient phosphorescence in the blue, green and red, respectively, as shown in Figure 2.8[80]. The bridging ligands rigidly link the two metal centers of the three binuclear compounds [81]. For compound **1**, the emission spectrum indicates a mixed ^{3}LC/^{3}MLCT excited state [78], providing evidence for a weak interaction between the two metal centers. In addition, broad and featureless emission spectra of compounds **2** and **3** are observed, and assigned to ^{3}MMLCT [82]. This occurs when the metal centers are in close proximity, and their interactions are enhanced. An analogous Pt complex, [(2-(4′,6′-difluoro-phenyl)pyridinato-N,$C^{2'}$)Pt(2-thiopyridyl)]$_2$ (FPt2) with a peak emission at a wavelength of λ=610 nm has also been studied, and has a Pt-Pt distance of 2.87Å. [83].

Table 2.1: Ligands of Pt compounds and their parameters.

Compound	R,R'	Pt-Pt Distance ($\mathring{A}$)	λ_{max}(nm)
FPt1	-	-	462
1	H,H	3.38	466
2	Me,*t*-Bu	3.06	546
3	*t*-Bu,*t*-Bu	2.83	630
FPt2	-	2.87	610

Here time-resolved photoluminescence of four, Pt-based binuclear complexes are investigated, and large triplet energy splittings of compounds **2**, and **3** and FPt2 are observed. Theoretical analysis of the phosphorescent properties of the complexes is provided, followed by experimental techniques and details. Results from the transient measurements are given, as well as analysis and simulations based on density function

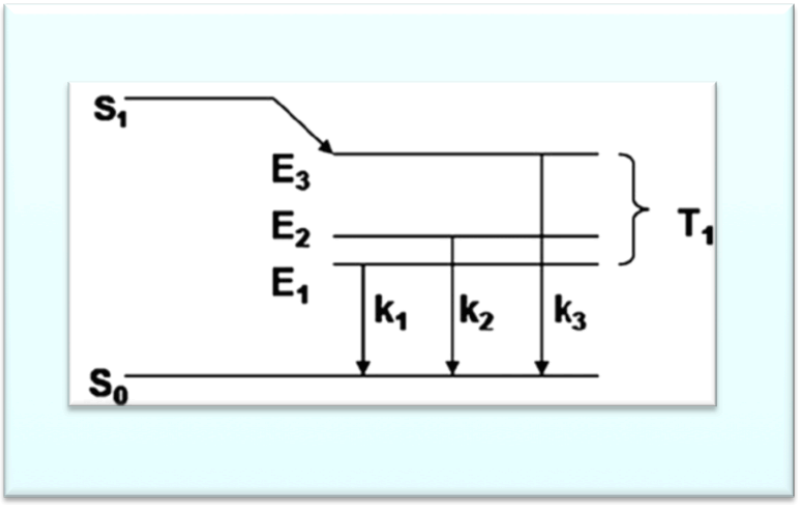

Figure 2.9: Schematic energy level diagram for the splitting of the lowest triplet state (T_1) into three sublevels E_1, E_2, and E_3, which has a radiative decay rate of k_1, k_2 and k_3, respectively. S_0 is the ground state and S_1 the lowest singlet state.

theory (DFT) to interpret the spectral properties.

2.3.2 Theory

Zero-field splitting (ZFS) refers to the difference between otherwise degenerate triplet states in the absence of an external magnetic field [29]. In the case of a triplet organic molecule, the interaction between spins is anisotropic, i.e., the interaction energy will be different in different directions. In effect, the spins are coupled to the molecular framework and this is equivalent to quantization of spin along some arbitrarily defined x, y, and z axes due to a local magnetic field within the molecule due to spin-spin interactions. In practice this molecular magnetic field amounts to $\sim 0.2^{-1}$, namely the effective molecular magnetic field. The separation of the triplet sublevels (T_x, T_y, and T_z) is termed the ZFS.

For transition metal complexes, ZFS is the leading term in the spin Hamiltonian resulting from dipolar magnetic interactions of the unpaired electrons. For most materials, the dipolar interactions between spins average to zero since the spins are

in a rapid isotropic motion in the molecular frame. However, splitting arises where there is large overlap of the orbitals containing the unpaired spins, which results in electron exchange and spin quantization. Using perturbation theory, ZFS has two contributions: a first-order term resulting from dipolar spin-spin ($\mathbf{S} \cdot \mathbf{S}$) coupling, and second-order $\mathbf{L} \cdot \mathbf{S}$ coupling which is dominant in high Z transition metal molecular complexes [84]. The ZFS values for most of the transition metal compounds are determined using high resolution optical spectra. For example, $[Rh(bpy)_3]^{3+}$, $[Pt(bpy)_2]^{2+}$ have small ZFS of only $\sim 0.1 cm^{-1}$, while the splitting of $[Os(bpy)_3]^{2+}$ reaches 211 cm^{-1} due to its increased metal character. Alternatively, details of the energetics of ZFS can be obtained by studying temperature-dependent photoluminescence decay dynamics. Assuming a Boltzmann distribution among the field-split sublevels, the transition rate follows [85]:

$$k_{therm} = \frac{k_1 + k_2 e^{-\Delta E_{21}/k_B T} + k_3 e^{-\Delta E_{31}/k_B T}}{1 + e^{-\Delta E_{21}/k_B T} + e^{-\Delta E_{31}/k_B T}} \tag{2.10}$$

where ΔE_{31} and ΔE_{21} are the energy differences between triplet sublevels 3 and 1, and 2 and 1, respectively, as shown in the proposed energy level scheme of Figure 2.8 (c). Also, T is the temperature, k_B is Boltzmann's constant, and k_1, k_2 and k_3 are decay rates from the three sublevels. This equation is simplified at low temperature, where:

$$k_{therm}^{LT} = k_1 \tag{2.11}$$

since the population is frozen into the lowest sublevel 1. Furthermore, at high temperature, where Equation (2.10) simplifies to:

$$k_{therm}^{RT} = (k_1 + k_2 + k_3)/3 \tag{2.12}$$

2.3.3 Experimental

Each metallorganic phosphor was codeposited at $8wt\%$ with the large energy gap host, UGH2 [86] onto a clean Si substrate by thermal evaporation in a vacuum chamber with a base pressure of 10^{-7} Torr. The large energy gap of UGH2 ensures that exciton formation by optical pumping occurs directly on the guest phosphor molecules. The thickness of the organic layer was fixed at 180nm.

Samples were mounted in a cryostat where the temperature was varied from 4K to 295K. Photoluminescence (PL) was excited using a N_2 laser with a wavelength of λ=337nm at a 10Hz repetition pulse rate. The 18μJ pulse with a duration of 0.7ns was focused on the sample to a 1.5mm diameter spot. The resulting PL was focused into a streak camera (Hamamatsu C4334) that monitored the time-resolved spectral decay.

2.3.4 Results

The PL spectra for three compounds as solid solutions in UGH2, are shown in Figure 2.8 (b). For compound **1**, the emission spectrum shows vibronic features that are typical for ^{3}LC/^{3}MLCT mixed excited states. A fit of the spectrum of compound **1** to its three vibronic components is shown in Figure 2.10. In contrast, compounds **2** and **3** show broad and featureless emission spectra, similar to those of excimers. Emission from **2** and **3** results from a $^3[d\sigma^\star, \pi^\star]$ state, where the $\sigma^\star$ orbital is formed by the two occupied dz^2 orbitals of the co-facial Pt centers[78]. The locations of the emission peaks are temperature independent for both complexes, although they broaden with increasing temperature, as shown in Figure 2.11 (a) and (b). For compound **2**, the full width at half maximum (FWHM) increases from 62nm at 12K, to 92 nm at 295K, while for compound **3**, the FWHM increases from 77nm at 12K to 114nm at 295K. Integrating the area under the PL spectra can yield the total luminescence efficiency. Normalized integrated PL intensities and efficiencies

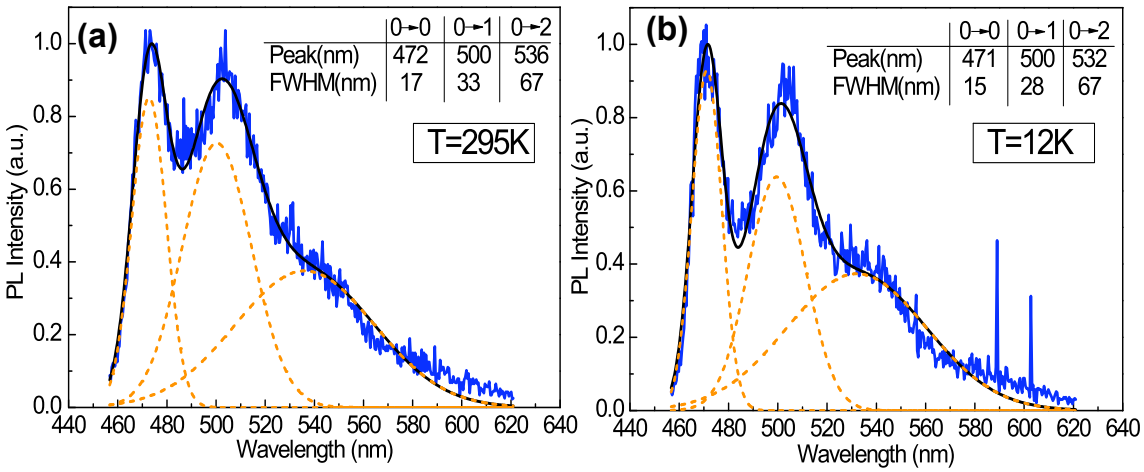

Figure 2.10: Phosphorescent spectra of compound **1** at (a) room temperature (T = 295 K) and (b) T = 12 K. Complexes are doped into the wide energy gap host UGH2 at 8wt%. Vibronic spectra corresponding to 0→0, 0→1, and 0→2 transitions are fit by Gaussian distributions (dashed lines). Their sum is shown by the solid line. Insets show the peak locations and full width at FWHM for each vibronic peak. Emission peaks narrow at low temperature, although their intensities are temperature insensitive.

for compounds **2** and **3** doped in UGH2 are provided in Figure 2.11 (c) and 3(d), respectively.

The dimer properties of the complexes can be understood in terms of their phosphorescent decay transients. In Figure 2.12, we show the phosphorescent decay at T= 4K and 295K after pulsed photoexcitation for compounds $\mathbf{1}, \mathbf{2}, \mathbf{3}$ and FPt2. For FPt2, we observed significant non-linearities in the transients, suggesting the presence of non-radiative loss channels due to triplet-triplet (T-T) annihilation [87]. In this case, the phosphorescent emission intensity follows:

$$L(t) = \frac{L(0)}{(1 + K\tau)\, e^{t/\tau} - K\tau} \tag{2.13}$$

where

$$K = \frac{1}{2} k_{TT} \left[{}^3M^{\star}(0) \right]. \tag{2.14}$$

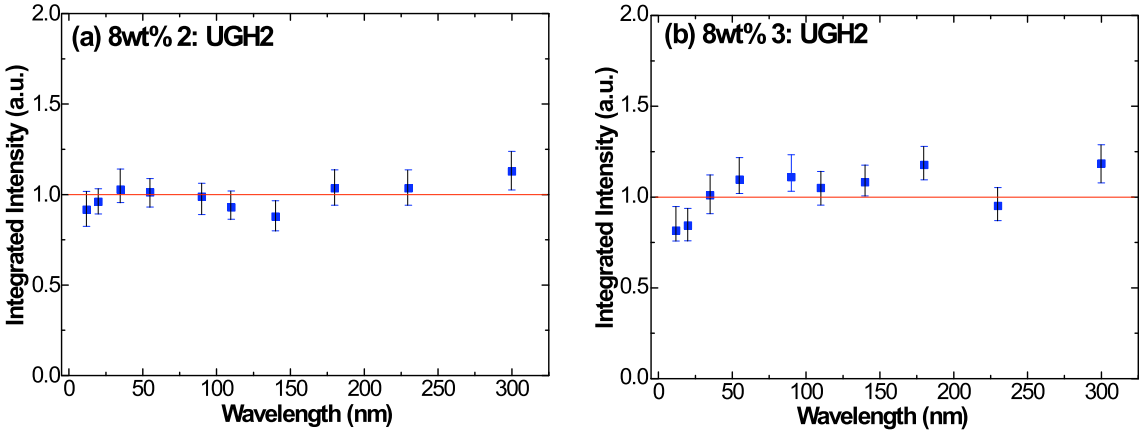

Figure 2.11: Temperature dependence of the peak PL intensity of compounds (a) **2** and (b) **3** doped into UGH2 at 8wt%. The corresponding integrated PL intensity of **2** and **3** are shown in (c) and (d), respectively. Data were taken between T=295K and 12K.

Here, $[^3M^\star(0)]$ is the initial triplet excited state concentration, τ is the natural phosphorescent recombination lifetime, k_{TT} is the rate of triplet annihilation, and $L(t)$ is the luminescence intensity at time t. The radiative lifetime is measured between room temperature to T=30K, yielding τ=(2.0±0.1)μs and τ=(12.0±0.1)μs at these extremes, respectively. We note that the low triplet mobility prevents rapid diffusion of excitons to the dopant from nearby host sites, contributing along with ZFS, to the longer lifetime for FPt2 at T<30K, and hence those data are not included in the analysis.

For compound 1, the lifetime shows only a slight temperature dependence, ranging from τ=(6.3±0.1)μs at T=295K, to τ=(8.6±0.1)μs at T=4K. However, the lifetimes of compounds **2**, **3** and FPt2 all exhibit a pronounced dependence on temperature, as listed in Table 2.2.

Table 2.2: Radiative lifetimes of binuclear complexes in this study.

Temperature	**1** (μs)	**2** (μs)	**3** (μs)	FPt2 (μs)
T=295K	6.3 ± 0.1	2.3 ± 0.1	2.0 ± 0.1	2.0 ± 0.1
T=4K	8.6 ± 0.1	14.4 ± 0.1	17.0 ± 0.1	12.0 ± 0.1

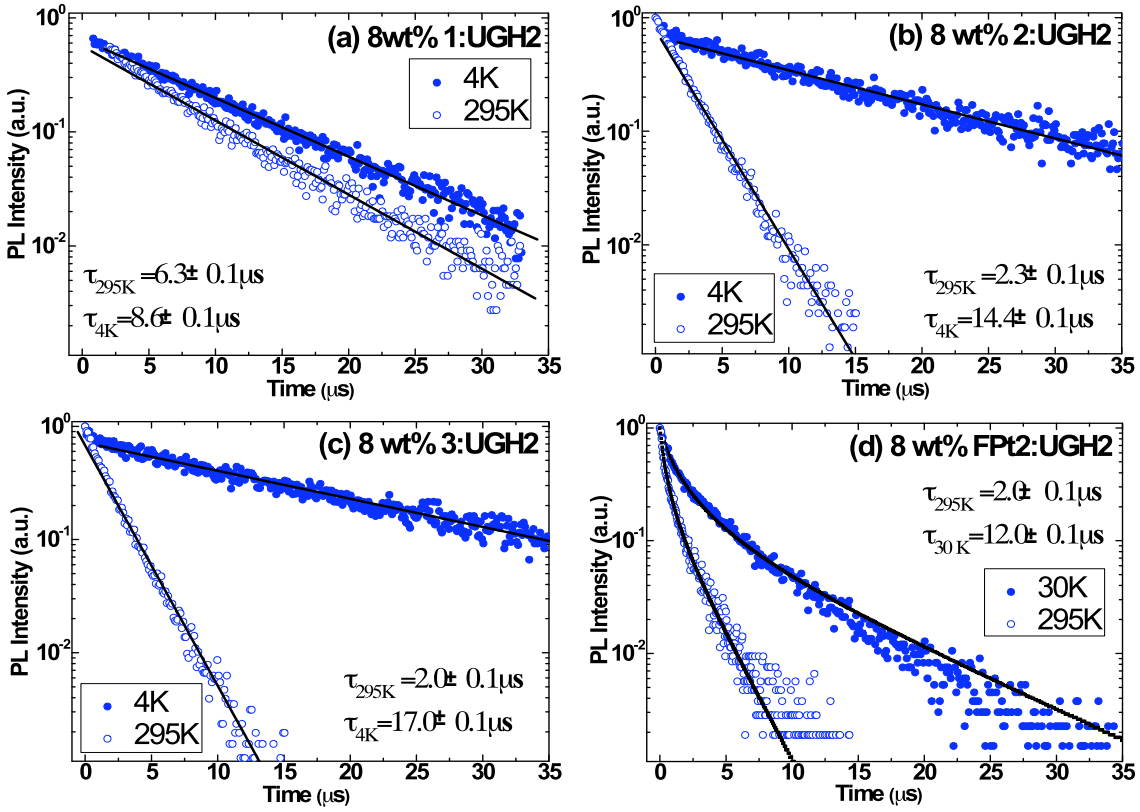

Figure 2.12: Radiative lifetime of compounds (a) **1**, (b) **2** (c) **3** and (d) FPt2 at room temperature (T=295K) and 4K (30K for FPt2) after pulsed photo excitation using a N_2 laser at a 10Hz repetition pulse rate, and at a wavelength of λ=337nm. Dots are experimental data and solid lines are fittings. Compounds **2**, **3** and FPt2 exhibit strong temperature dependent decay. The curves are normalized for comparison. The structure of FPt2 is shown in the inset of (d).

2.3.5 Discussion

As shown in Figure 2.12, the emissive decay rate increases with temperature, while the PL intensity for compounds **2** and **3** remains constant. This is evidence for the thermal population [88] of the higher emitting sublevels E_2 and E_3, as suggested in (2.10). Now, the relationship between the non-radiative and radiative emission rates is determined from the PL efficiency via:

$$\eta_{PL} = \frac{k_R}{k_R + k_{NR}}. \tag{2.15}$$

Since the integrated PL intensity in Figure 2.11 shows no temperature dependence, we therefore conclude that either $k_R \gg k_{NR}$ and the observed temperature dependence in lifetime is only due to changes in k_R (i.e. $\eta_{PL}\sim 1$) or that the ratio, k_{NR}/k_R is temperature independent. The latter possibility only occurs in the unlikely event that the Arrhenius parameters are identical for k_R and k_{NR} in both **2** and **3**, and thus we favor the former explanation.

Figure 2.13 shows the Arrhenius plots of the temperature dependent decay rate measurements (filled triangles) for compounds $\mathbf{1} - \mathbf{3}$. Equations (2.10)-(2.12) are used to fit the data (open circles) and obtain the corresponding ZFS values. Thus, ΔE_{31}=(142±9)cm^{-1} and ΔE_{31}=(113±10)cm^{-1} for compounds **2** and **3**, respectively, which are considerably larger than that of **1**, with ΔE_{31} =(28±3)cm^{-1}. The complete fitting parameters are listed in Table 2.3. Note that for compound **1**, the energy splitting is small. In this case, the condition of $\Delta E_{21} \gg kT$ required for the approximation in (2.12) is not valid at T=4K. Hence, to check the result, the fits yielding ΔE_{31}, ΔE_{31}, and k_2, were used directly in (2.10) to obtain a non-radiative rate to within the error range of the data.

To further understand the experimental results, we estimated the metal participation in the triplet state, which is expected to influence the magnitude of the ZFS.

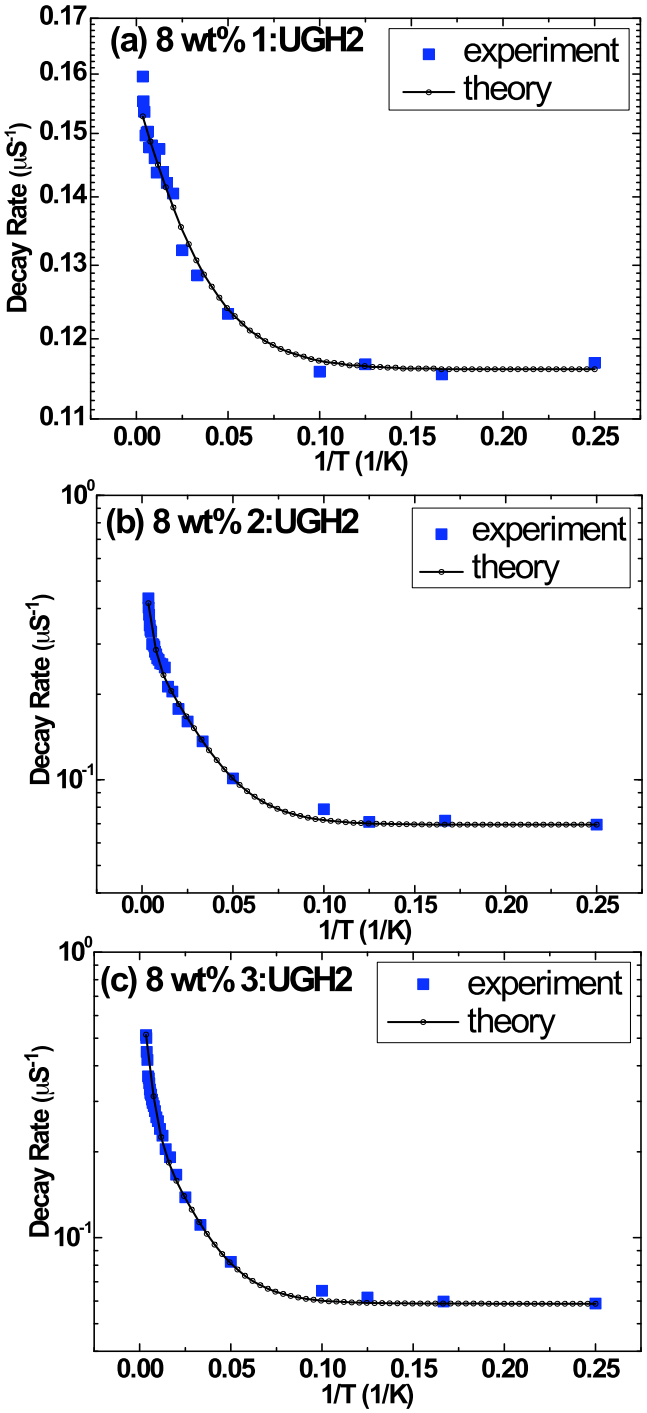

Figure 2.13: Arrhenius plots and zero-field splitting fitting of temperature dependent decay rates of compounds (a) **1**, (b) **2**, and (c) **3**. Fitting parameters are provided in Table 2.2.

Table 2.3: ZFS energies and transition rates for binuclear Pt complexes.

Compound	ΔE_{31} (cm^{-1})	ΔE_{21} (cm^{-1})	k_1 (μs^{-1})	k_2 (μs^{-1})	k_3 (μs^{-1})
1	28 ± 3	<4	0.12 ± 0.001	0.11 ± 0.02	0.25 ± 0.02
2	142 ± 9	31 ± 5	0.07 ± 0.001	0.42 ± 0.08	0.81 ± 0.08
3	113 ± 10	33 ± 6	0.06 ± 0.001	0.32 ± 0.06	1.12 ± 0.06

The calculated orbital distribution is shown in Figure 2.14. No pronounced change in spin density takes place at the pyridyl ring, whereas the triplet spin density surfaces at the Pt-Pt center for compounds **2** and **3** are double that of **1**. The spin densities normalized to that on the ligand are listed in Table 2.4 . Indeed, twice the electron density resides on the Pt centers in compounds **2** and **3** compared to **1**.

Table 2.4: The spin density at the metal center normalized to that on the ligand.

Compound	Pt 1	Pt2
1	0.103	0.002
2	0.198	0.196
3	0.200	0.206

Based on the point dipole model [84], $\mathbf{L} \cdot \mathbf{S}$ coupling is enhanced as dipoles are brought into close proximity, as in compounds **2**, **3**, and FPt2. According to Figure 2.14, compounds therefore show a significant overlap of the d-orbitals of the individual metal atoms that allows for strong interactions, thus lifting the triplet energy degeneracy and leading to a pronounced ZFS.

We consider a simple two-spin model based on the DFT simulation to roughly estimate the relative magnitudes of the ZFS in compounds **2** and **3** compared to their mononuclear counterpart, compound **1**. For simplicity, we assume that the LUMO is localized at the center of the pyridyl ring, while the HOMO is centered on the platinum atoms. A uniform spin density distribution over a sphere of radius r_0 is assumed for compound **1**, and $2r_0$ for compounds **2** and **3**, as listed in Table 2.4. Compounds **2** and **3** are treated together since they have a similar spin density as

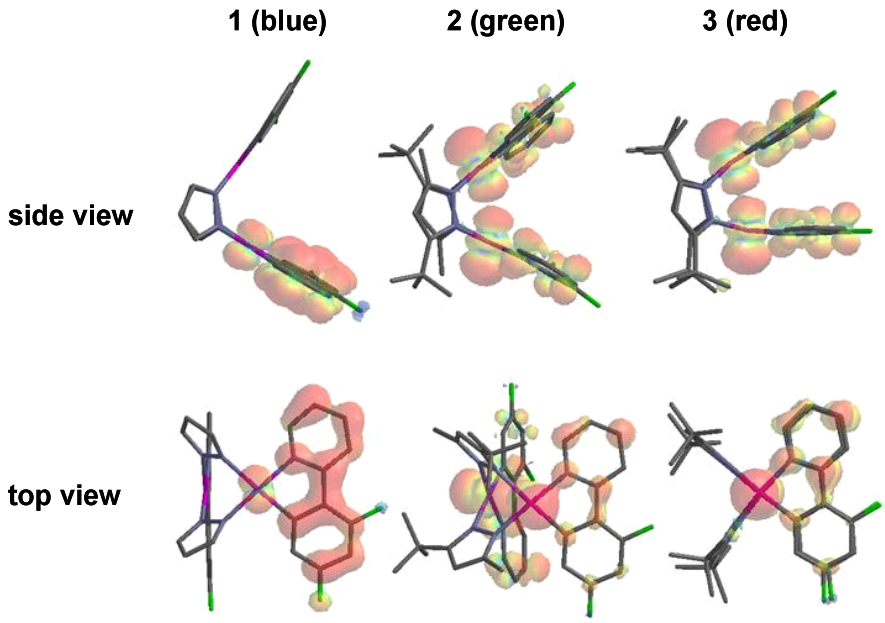

Figure 2.14: Triplet spin density surfaces for compounds **1**, **2**, and **3**. The spin density surface in the triplet state at the Pt-Pt center for compounds **2** and **3** are double to that of compound **1**. This indicates a large dz^2 orbital character in **2** and **3**.

determined by DFT simulations.

Considering only $\mathbf{L} \cdot \mathbf{S}$ coupling, and assuming that the Coulomb potential, arises from a nucleus of charge Ze, then the spin-orbit Hamiltonian follows:

$$H_{so} = -\frac{e\hbar^s}{2m_e^2c^2r}\frac{d\phi}{dr}\mathbf{L} \cdot \mathbf{S} = \xi(r)\mathbf{L} \cdot \mathbf{S} \tag{2.16}$$

where

$$\xi(r) = \frac{Ze^2\hbar^2}{2m_e^2c^2r^3} \tag{2.17}$$

Here, e is the elementary charge, r is the distance between the metal center and the unpaired electron of the ligand , and m_e is the mass of an electron. Then the spin-orbit interaction energy for compound i=**1**, **2** and **3** follows $E_{so}^i \propto 1/r^3$. This behavior allows us to calculate the integral over an ideal spherical spin density distribution.

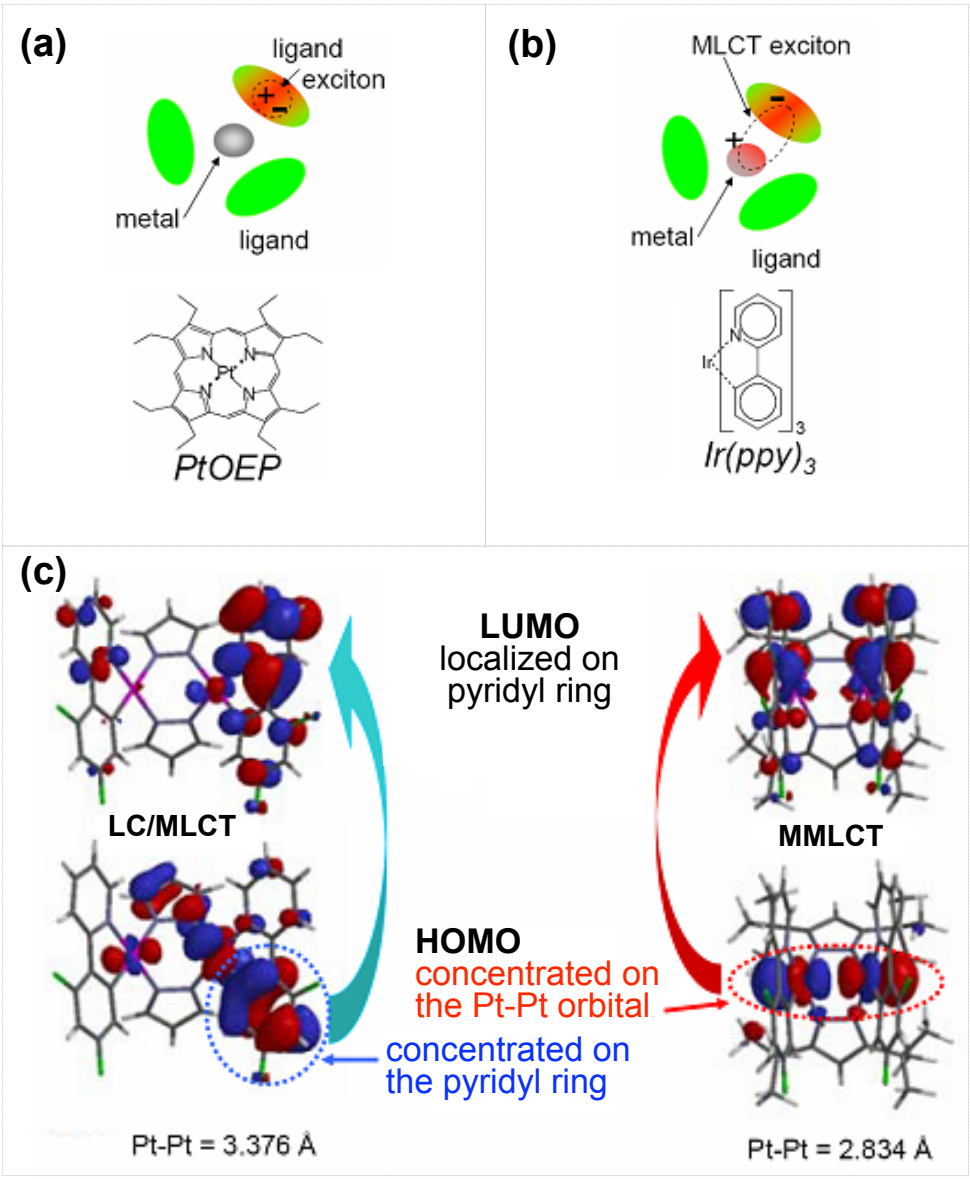

Figure 2.15: (a) Formation of ligand exciton, typically on molecules with negligible metal-ligand interaction, e.g. PtOEP. (2) Formation of ^{3}MLCT exition, typically on molecules with pronounced metal-ligand interaction, e.g. Ir(ppy)$_3$. (c) Triplet spin density surface for molecules with Pt-Pt distance of 3.376 $\mathring{A}$ and 2.834 $\mathring{A}$. Smaller Pt-Pt distance introduce ^{3}MMLCT where HOMO is concentrated on the Pt-Pt orbital instead of on theh pyridyl ring. (Image courtesy of Tompson Research Group at USC)

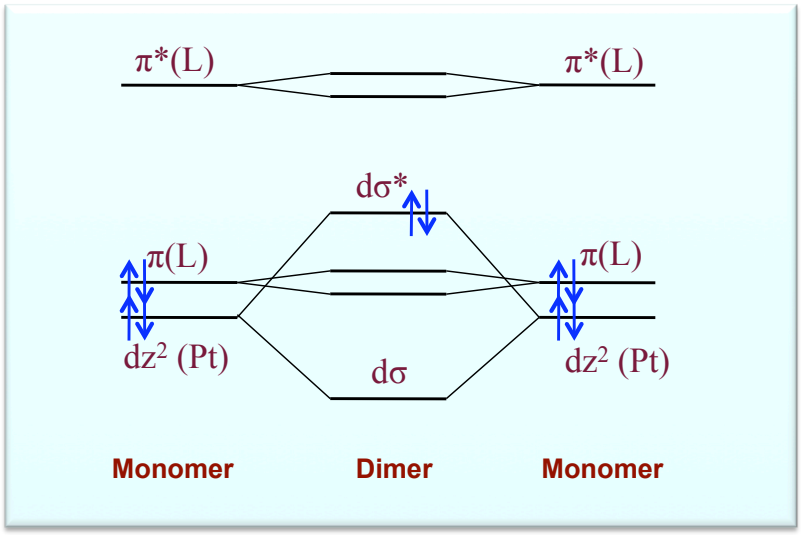

Figure 2.16: Schematic molecular orbitals for Pt complexes. Dimer is formed when there is strong metal-metal interaction.[29]

Therefore, we obtain $\Delta E_{31}^{2,3}/\Delta E_{31}^{1} = E_{so}^{2,3}/\Delta E_{so}^{1} = 6.3$, which is comparable with experimental results of $\Delta E_{31}^{2}/\Delta E_{31}^{1} = 5.1 \pm 0.9$, and $\Delta E_{31}^{3}/\Delta E_{31}^{1} = 4.1 \pm 0.8$ for compounds **2** and **3**, respectively (see Table 2.3). The difference between calculation and experiment arises from our estimation of complete LUMO localization at a point in the center of the ligand, in contrast to the actual situation where the electron density is distributed over the pyridyl group. The assumption of a uniform spin density distribution on the HOMO also introduces error, although the difference is relatively minor compared to the approximations made. Hence, we conclude that ZFS is enhanced due to the small Pt-Pt distance characteristic of this set of binuclear complexes.

We have studied the radiative decay dynamics of a series of Pt binuclear complexes used as phosphorescent dopants in OLEDs. By employing a three-sublevel, non-degenerate triplet spin model, we report large zero field splitting energies for complexes with strong metal-metal bonds, and have developed a detailed understanding of the photophysics underlying those interactions. A distance of $3\mathring{A}$ or less between the platinum centers allows for significant overlap of the d-orbitals of the individual

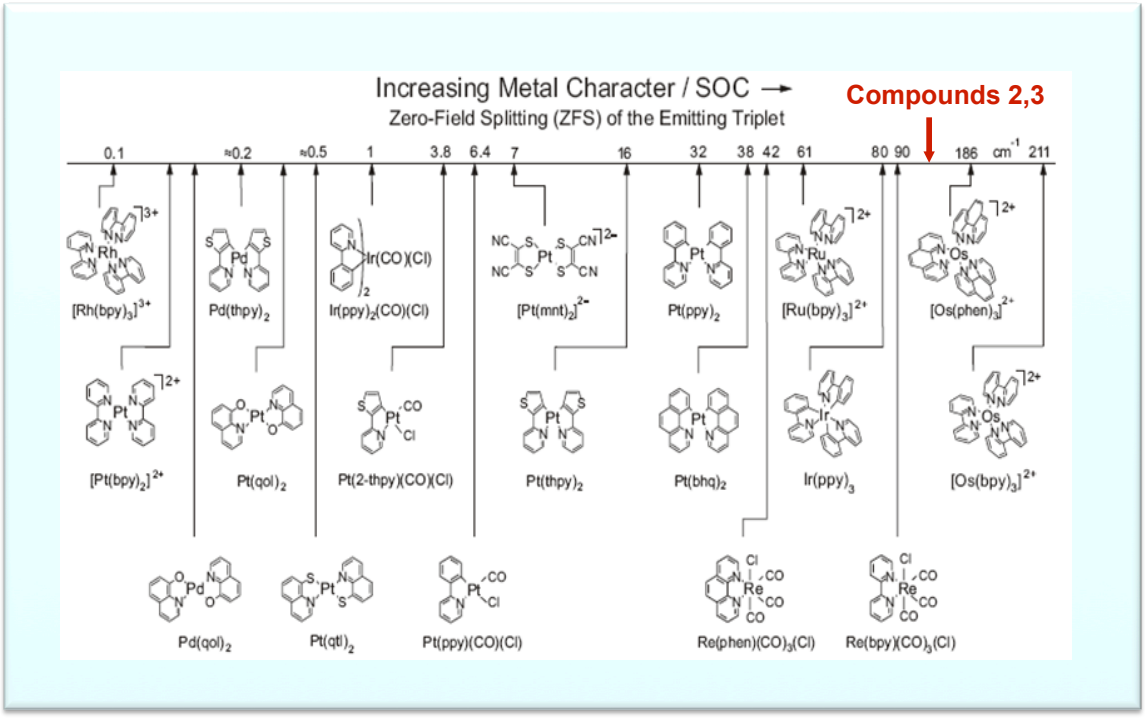

Figure 2.17: Summary of ZFS for phosphors with increasing metal character.[89]

metal atoms, leading to large ZFS energies.

The photophysical properties of organometallic phosphorescent emitters rely on a strong $\mathbf{L} \cdot \mathbf{S}$ coupling dependence on the metal-metal interaction, which controls the magnitude of ZFS of the triplet state. The corresponding ZFS energies reported here are much larger than those in other similar complexes [90]. When applied to OLEDs, the increased metal character of the excited states enhances the intersystem crossing rate [89], and hence increases the internal quantum efficiency of the triplet emission. This understanding may lead to the design of new organic-based transition metal complexes with optimized emission properties for a broad range of practical device applications.

CHAPTER III

High Intensity Organic Light-emitting Diodes

In this chapter, we will start with the carrier injection and transport properties in OLEDs by highlighting some of the materials that have drawn considerable attention. The device efficiency characterization is introduced in detail, followed by experimental techniques including fabrication and testing. To conclude, we will give an example of fabricating a stacked OLED for illumination applications.

3.1 Diode Basics

3.1.1 Carrier Injection

High efficiency OLEDs strongly depend on effective charge injection from the electrodes to the organic medium. An unbalanced injection results in an enhanced non-radiative recombination due to the interactions of excitons with the excess of charge carriers. A characterization and understanding of the injection process as well as the bulk conductivity process is important to further optimize and develop new organic systems for electronics and photonics applications. Charge-carrier injection from a metallic contact into solids, and especially into semiconductors, has been extensively investigated, and it is well known that the energy barrier between the contact and the organic dielectric controls the hole and electron injection. In the absence of surface states and a depletion region due to impurity doping, the energy

barrier is $\Delta_h = I - \Phi_{anode}$ for holes and $\Delta_e = \Phi_{cathode} - A$ for electrons, where Φ is the work function of the contact material and I and A are the ionization energy and electron affinity of the organic, respectively.

Injection of charge from most electrode materials requires overcoming a barrier at the electrode/organic interface. The injection process may govern the performance of organic devices if the supply of carriers can not achieve the maximum that the material can transport. This would be the so-called injection-limited regime, which is commonly described either by the Fowler-Nordheim (FN) model for tunneling injection[91] or by the Richardson-Schottky (RS) model for thermionic emission[92]. The FN model assumes that the electrons tunnel from the contact through a triangular barrier into unbound continuum of states and predict the temperature independent J_{FN} characteristic[91]

$$J_{FN} = BF^2 exp\left[-\frac{b}{F}\right] \tag{3.1}$$

where $B = e^3/8\pi h\Delta$ and $b = [8\pi(2m^\star)^(1/2)\Delta^{3/2}]/3he$. Here e is the elementary charge, h is the Planck constant, and m^* the effective mass of the carrier of the dielectric. The RS model assumes that the electron acquires sufficient thermal energy to cross the potential maximum and the characteristic J_{RS} is given by[93]

$$J_{RS} = AT^2 exp\left[-\frac{\Delta - (e^3/4\pi\epsilon\epsilon_0)^(1/2)F^(1/2)}{kT}\right] \tag{3.2}$$

where A^* is the Richardson constant, T is the temperature, and k the Boltzmann constant.

3.1.2 Carrier Transport

When injection is achieved from both electrodes due to the negligible energy barrier at the contacts, the relatively low mobility of organic materials (typically

$10^{-5} \sim 10^{-3}$ cm^2/(Vs)) leads to charge accumulation and electric field redistribution. In this limit, the only material parameters determining the current are the carrier mobility and the dielectric constant, as described by Mott-Gourney square law, also known as Child's law in solid.[94]

$$J_{MG} = \frac{9}{8}\epsilon\epsilon_0\mu\frac{V^2}{L^3} \tag{3.3}$$

where μ and ϵ are the mobility and dielectric constant of the material, ϵ_0 is the permittivity of vacuum, L is the distance between the contacts, and V is the applied voltage. Equation 3.3 is valid for a mobility μ that is independent of the applied electric field and the current density.

However, the typically low mobility of disordered organic materials means that charge carriers are localized and transport involves discrete hopping. This makes it difficult to rationalize the models described above which were developed for band-type materials. A more detailed study on electron injection in an organic/inorganic interface is provided in Chapter IV.

3.1.3 The Efficiency of OLEDs

The external quantum efficiency (EQE) is used to characterize the performance of an OLED. It is defined as the number of photons emitted from a device out of the number of injected charges per unit time:

$$\eta_{EQE} = \frac{hc/e}{I}\int \lambda\Psi(\lambda)d\lambda = \eta_R\chi\phi_{PL}\eta_{OC} \equiv \eta_{IQE}\eta_{OC} \tag{3.4}$$

where $\Psi(\lambda)$ is the spectral density at the emissive wavelength λ, c is the speed of light, and I is the operation current. Here EQE is shown to be composed of four factors: the probability of exciton formation from the injected charge carriers, η_R, the spin fraction of emissive excitons χ, the photoluminescent efficiency of the emissive molecule ϕ_{PL},

and the outcoupling efficiency η_{OC}.

For $\eta_R \sim 1$, the injected electrons and holes have to recombine and form excitons without leaking all the way through the organic layers to the electrodes. By using the multi-layer structure suggested by Tang and VanSlyke[12], carrier leakage can be effectively prevented in the organic heterostructure. The hole-transporting layer (HTL) and electron-transporting layer(ETL) help block the leakage of electrons to the anode and holes to the cathode. Excitons are therefore formed at the organic interface. Following exciton formation, efficient decay is also required. Since the ratio of singlets to triplets is 1:3, $\chi \sim 0.25$ is achieved for fluorescent devices in which only singlets are harvested, while $\chi \sim 1$ in phosphorescent devices since both singlets and triplets are radiative.

The third factor, ϕ_{PL}, is generally a measure of the radiation efficiency of the absorbed excitons. For a given excited state, ϕ_{PL} is decided by the competition between the rates of various radiative (k_R) and non-radiative (k_{NR}) transitions, i.e. intersystem crossing, internal conversion, etc. The phosphorescence quantum yield is[95]

$$\phi_{PL} = \frac{k_R}{k_R + k_{NR}} = \frac{k_{ph}}{k_{ph} + k_f + k_{IC} + k_{ISC}}, \tag{3.5}$$

where k_{ph}, k_f, k_{IC}, and k_{ISC} are the rates of phosphorescence, fluorescence, internal conversion, and intersystem crossing, respectively. The presence of a metal atom in complexes, such as $Ir(ppy)_3$, increase the singlet-triplet mixing and have demonstrated the principal advantage of phosphors. The emission energy for organometallic phosphors is closely related to the structure of organic ligands, making it possible to design a series of efficient phosphorescent emitters that covers most of the visible spectrum. The metal center of the complex can also be used to fine-tune its emission energy. The emission from a transition metal complex originates from its lowest energy triplet excited state. Spectroscopic analysis shows that this state is predom-

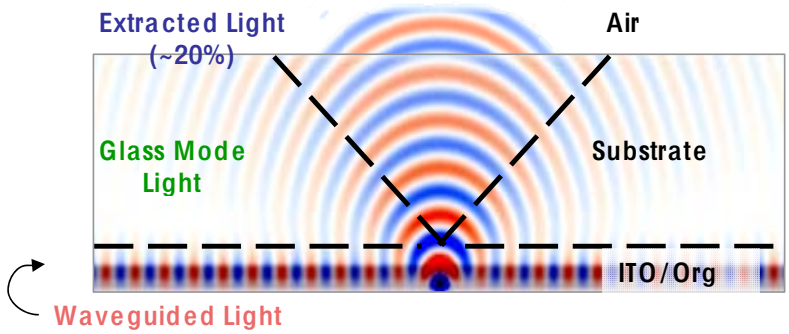

Figure 3.1: Trapped light in high-index organic and ITO layer.

inantly localized on the cyclometalating ligands, mixed with singlet metal-to-ligand charge transfer (^{1}MLCT) character.[96] Modification of ancillary (non-emissive) ligands affects the energy of the metal orbitals and thus the amount of ^{1}MLCT character in the excited state. Varying the ratio of ligand centered to ^{1}MLCT character directly affects the energy of the mixed excited state. With the optimized chemical design of the phosphors in the state-of-the-art OLEDs, ϕ_{PL} =80-90%.

The primary limitations to the quantum efficiency of OLEDs is the outcoupling fraction η_{OC}. The fraction of photons emitted in the forward-viewing direction is reduced by absorption losses and waveguide modes, resulting in an outcoupling efficiency η_{OC}=20%. A variety of techniques have been employed to increase the output coupling fraction up to 50% by substrate surface modifications, such as gratings, microlenses, and low index substrates, etc.[97, 98]

Another characteristic of OLED performance is power efficiency η_{PE}, defined as the ratio of luminous power out as detected by the human eye L, to the electric power input VI.

$$\eta_{PE} = \frac{L}{VI} = \Phi\eta_{EQE}\frac{V_\lambda}{V} \tag{3.6}$$

where V is the voltage corresponding to the drive current I, $V_\lambda = hc/eV$ is the emissive photon energy in eV and the ratio, and $\frac{V_\lambda}{V}$ is defined as the electrical efficiency

which can be increased by improving charge balance. Here the photopic response, Φ, is defined as the responsivity of the eye, $P(\lambda)$, to incident light with an arbitrary spectrum $\phi(\lambda)$:

$$\Phi = \frac{\int \phi(\lambda) P(\lambda) d\lambda}{\int \phi(\lambda) d\lambda} \tag{3.7}$$

Quantified in lumen (lm), $\Phi(\lambda)$ is responsive across the visible spectrum with a maximum 683 lm/W at λ=555nm.

3.2 Stacked Structure

White organic light-emitting devices (WOLEDs) have shown their potential for a new generation of solid-state lighting sources.[99, 100] To attain complete coverage across the visible spectrum, an OLED used for illumination purposes typically employs multiple emitters. A number of the different device architectures have been reported to achieve efficient white electroluminescence. Conventional WOLEDs employ red, green, and blue (R, G, and B) phosphorescent and/or fluorescent dopants in either a single EML, or multiple doped layers that allow for exciton formation in an expanded region.[101, 102, 103] Although the latter structure has shown an EQE approaching 20% in the forward-viewing direction, finding a suitable combination of hosts and phosphorescent dopants can be difficult due to the constraints that are placed on the relative energies of the constituent materials in these architectures.

Increasing attention has been directed toward the stacked organic light-emitting diode (SOLED), where individual OLED emitting elements are electrically connected in series in a vertical configuration.[104, 105, 106] The connecting charge generation layer (CGL) is formed by contact of an *n*-doped (Li, Cs, etc.) ETL with either a p-doped HTL[107, 108], or with transparent inorganic conductors such as vanadium oxide (V_2O_5), molybdenum trioxide (MoO_3), and tungsten trioxide (WO_3).[109]

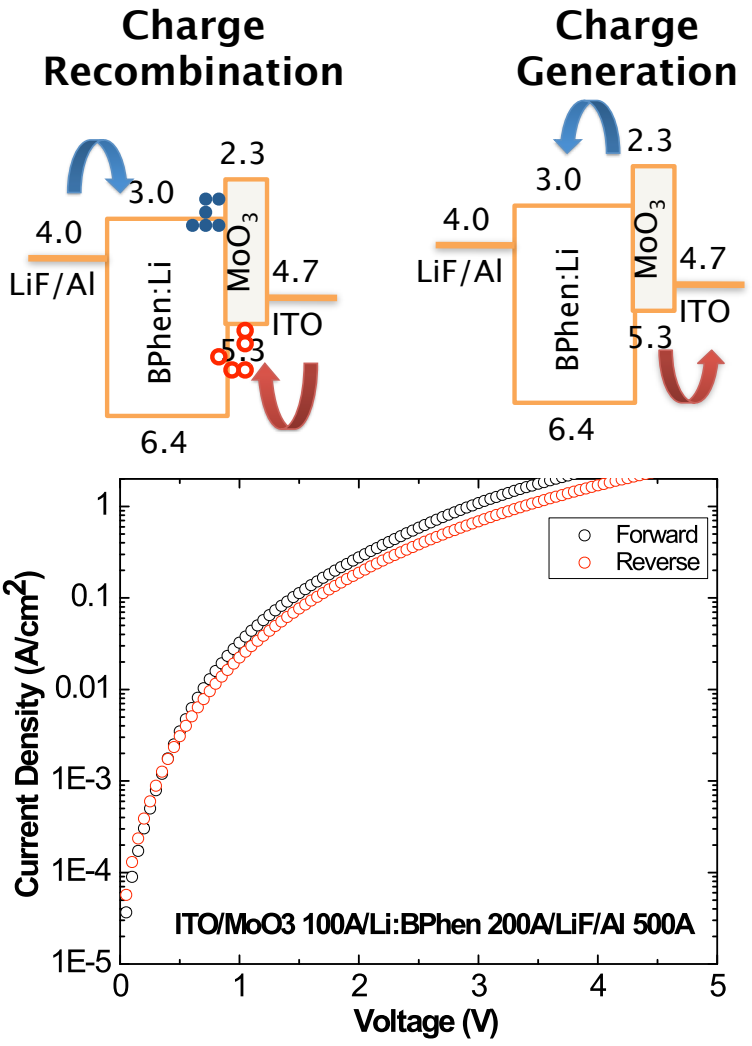

Figure 3.2: (Upper) Energy diagrams of CGL under charge recombination and charge generation. (Lower) Current density and voltage characteristics of CGL under forward and reverse bias.

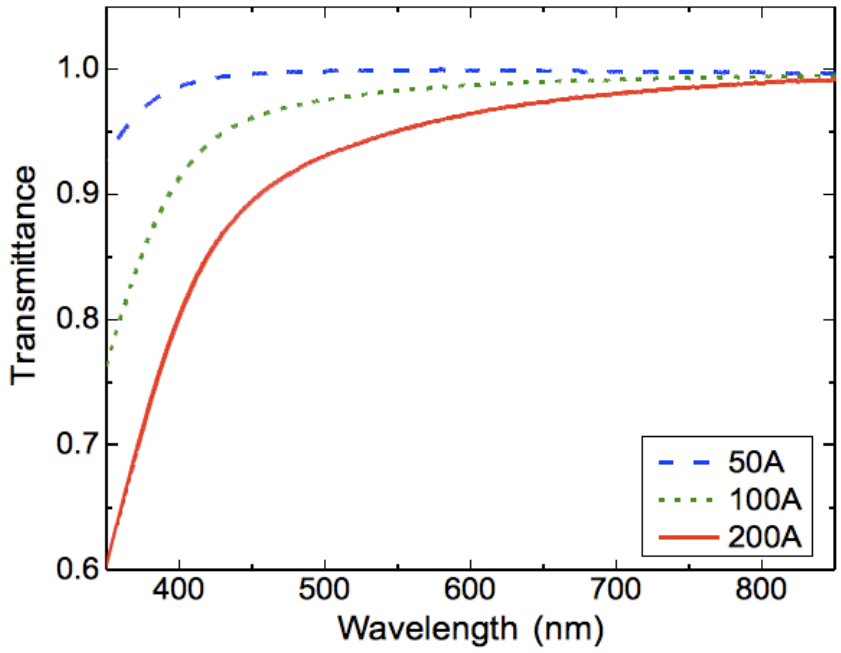

Figure 3.3: Transmittance of MoO_3 thin films with thickness of 50$\mathring{A}$(dashed line), 100$\mathring{A}$(short dashed line), and 200$\mathring{A}$(solid line).

In the stacked structure, individual primary-color-emitting phosphorescent OLEDs are interconnected by Li-doped 4,7-diphenyl-1,10-phenanthroline (BPhen) and MoO_3 to form a compound CGL. Recent reports on analogous structures used fluorescent emitting layers in one or both EMLs to achieve white light [110]. In contrast, our stacked architecture utilizes all electrophosphorescent R, G, and B elements to achieve high luminance and high quality white emission. The luminance at a fixed current density is approximately equal to the sum of that for each independent OLED element.

Figure 3.2 demonstrates the J-V characteristics of the charge generation layer (CGL). The device structure is ITO/MoO_3(100$\mathring{A}$)/Li:BPhen(200Å)/LiF(8Å)/Al(500Å). Under efficient charge generation, the reverse current (corresponding to charge generation) is expected to be comparable to the forward current (charge recombination). The comparison shows the Li:Bphen/MoO_3 as a promising CGL unit in SOLED. Another metric for the CGL quality is transparency. Figure 3.3 shows the transmittance

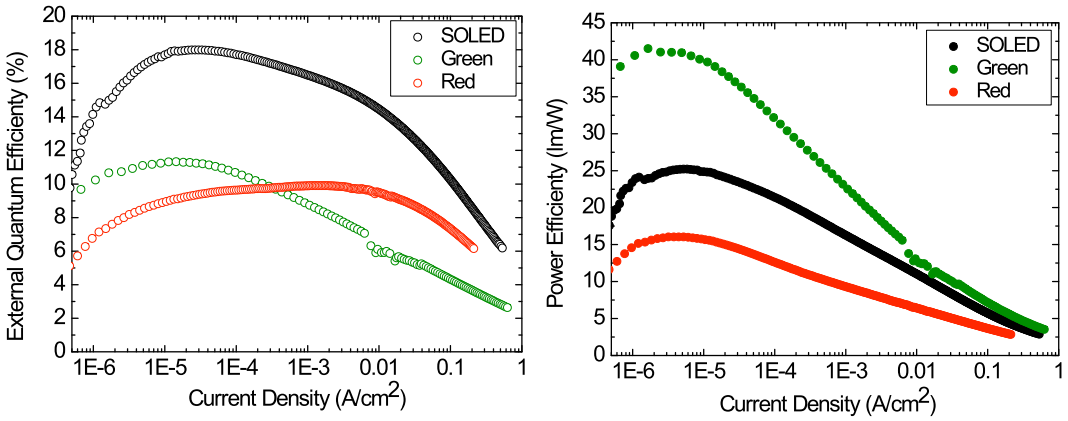

Figure 3.4: (Left) EQE and (Right) PE of SOLED with green and red components.

of MoO_3 thin films with thickness of 50Å, 100Å, and 200Å. The thickness of 100$\mathring{A}$ is chosen to be implemented in the SOLED structure. Up to 90% of transmittance is achieved between the wavelength of 400$\mathring{A}$ to 800Å.

To test CGL performance in a stacked structure, we start from SOLED with only green and red OLED components. In Figure 3.4, the EQE and PE of the two-component SOLED are shown in comparison. The device structure is listed below:

Green: ITO/NPD(400Å)/$Ir(ppy)_3$:CBP(250Å)/BPhen(400Å)/LiF/Al

Red: ITO/NPD(400Å)/PQIr:CBP(250Å)/BPhen(400Å)/LiF/Al

SOLED: ITO/NPD(400Å)/$Ir(ppy)_3$:CBP(250Å)/BPhen(500Å)/Li:BPhen(100Å)/ NPD(400Å)/$Ir(ppy)_3$:CBP(250Å)/BPhen(400Å)/LiF/Al

The forward-viewing PE of the SOLED peaks at 25 lm/W and rolls off to 15 lm/W at 1000 cd/m^2. Figure 3.5 shows the spectra of the SOLED under various current densities in comparison with each of the component. Under J=1, 10, and 100 mA/cm^2, the CIE coordinate is (0.34, 0.57), (0.37, 0.55), and (0.38, 0.54) respectively, and CRI is 35, 43, and 51, respectively.

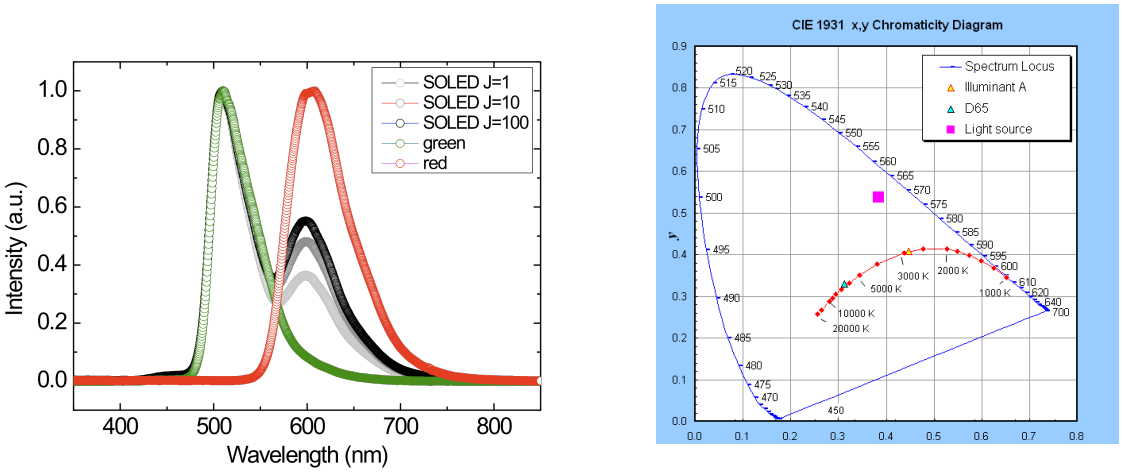

Figure 3.5: (Left) Spectra of SOLED under varied current density J=1mA/cm^2, 10mA/cm^2, and 100mA/cm^2, in comparison with the spectra of green and red OLED components. Spectra is normalized. (Right) CIE coordinate of the two-component SOLED.

Blue component has to be introduced to achieve white illumination. Figure 3.6 shows the performance of a blue OLED based on bis-(4,6-difluorophenylpyridinato) tetrakis(1-pyrazolyl)borate (FIr6) phosphor. Peak forward-viewing EQE of 8% and PE of 5lm/W are achieved, and the spectra is stable under varied current density from 1mA/cm^2 to 100mA/cm^2.

3.2.1 Fabrication

Based on the studies above, we demonstrate a white organic light-emitting device where individual red, green and blue (R, G, and B) phosphorescent OLEDs are vertically stacked and electrically interconnected by a compound MoO_3/Li-doped charge generation layer. Simulations based on weak microcavity effects are used to optimize the device performance. For the order of B, G, and R cells positioned relative to the ITO anode, the device yields a peak total External quantum efficiency (EQE) and power efficiency (PE) of $\eta_{ext} = (36 \pm 2)\%$ at a current density of $J = 82\mu$A/cm^2 and $\eta_p = (21 \pm 1)$lm/W at $J = 17\mu$A/cm^2, respectively. The EQE and PE of the device

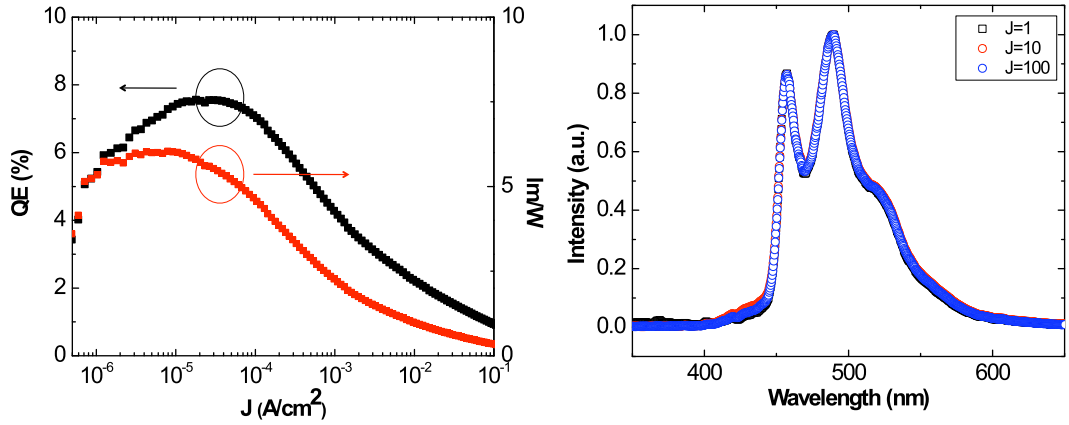

Figure 3.6: (Left) EQE and PE of blue OLED based on FIr6 phosphor. (Right) Spectra of FIr6 OLED under varied current densities, J=1, 10, and 100mA/cm^2.

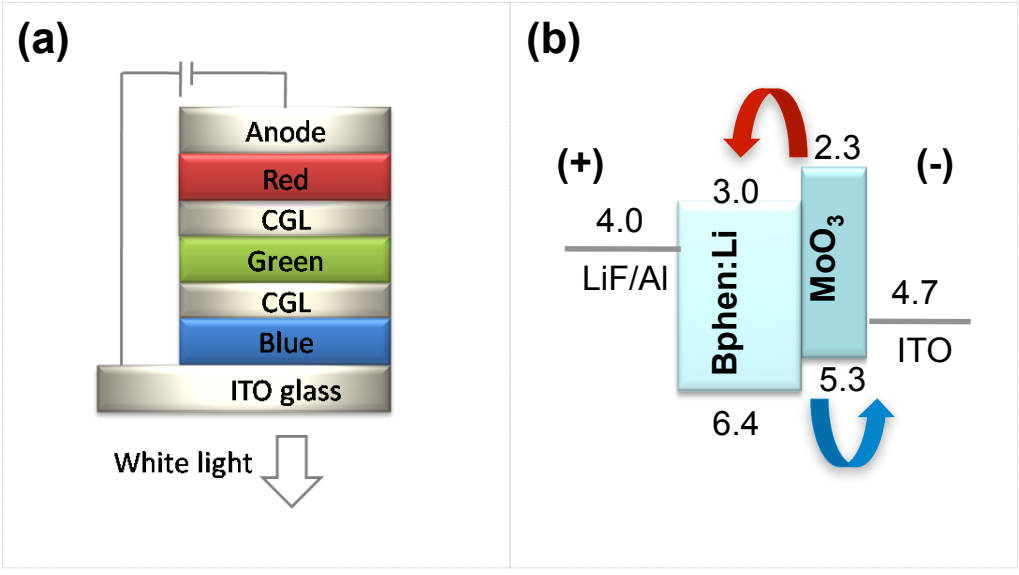

Figure 3.7: (a) Structure of RGB SOLED. (b) Charge generation layer Bphen:Li(100 Å)/MoO_3(100Å).

roll off to $(32 \pm 2)\%$ and (13 ± 1)lm/W at 1000cd/m^2 and J=2mA/cm^2. At this luminance, the device shows CIE chromaticity coordinates of (0.45, 0.36), and a CRI of 63.

Figure 3.8 shows the schematic energy level diagram of the RGB SOLED consisting of three interconnected R, G, and B OLED elements. The highest occupied, and lowest unoccupied molecular orbital energies are taken from the literature.[103, 111] Devices were grown on glass slides precoated with ITO with a sheet resistance of $20\Omega/sq$. Substrates were ultrasonically cleaned in detergent solution for about 1 min, followed by thorough rinsing in deionized water. They were then boiled in 1,1,1-trichloroethane (TCE), and rinsed in acetone followed by isopropyl alcohol (IPA), and dried in pure nitrogen gas between each step. Prior to transfer into a high vacuum ($\sim 10^{-7}$ Torr) deposition chamber, ten minutes exposure to UV/ozone is applied to increase the ITO work function. The B, G, and R OLEDs were sequentially deposited by thermal evaporation without breaking vacuum. A 10-nm thick BPhen layer doped with Li in a 1:1 molar ratio combined with a 10-nm thick layer of MoO_3 served as the CGLs between elements. The transmittance of the MoO_3 is 99.4% at a wavelength of 800nm, decreasing to 96.1% at 450nm. For each OLED element, a 40-nm thick film of 4,4-bis[N-(1-naphthyl)-N-phenyl-amino]-biphenyl (NPD) was used as the HTL, followed by 25nm-thick emission layer, and a 50nm-thick BPhen as the ETL. The undoped BPhen was used to prevent Li diffusion into the EML and to maintain charge balance at high bias.[112, 113]

3.2.2 Device Performance

To analyze the performance of the CGLs, three discrete monochrome R, G, and B control devices were simultaneously deposited with the SOLED. Each control has the same HTL, and ETL, and the same dopings, compositions and thicknesses of the EMLs used in the SOLED. Blue, green and red emission originate from the

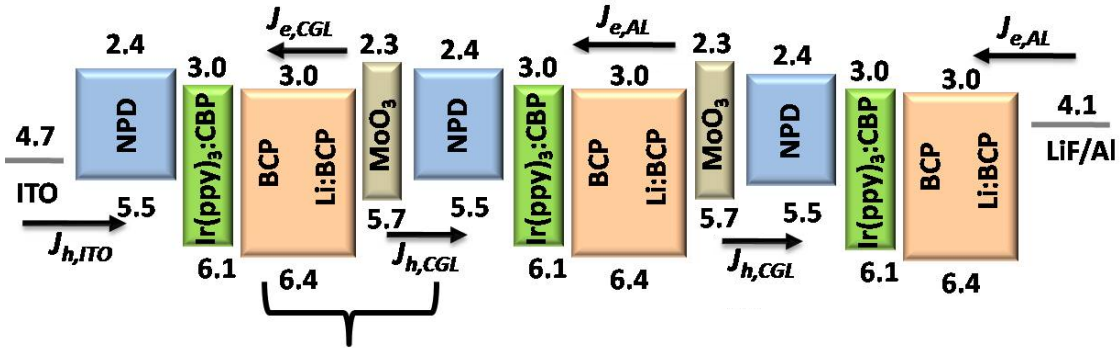

Figure 3.8: Proposed energy-level diagram of RGB SOLED. Numbers indicate the HOMO and the LUMO energies relative to vacuum (in eV). The HOMO and the LUMO energies of FIr6, $Ir(ppy)_3$, and PQIr are (6.1 and 3.1 eV), (5.1 and 2.6 eV), and (5.0 and 2.7 eV), respectively. Arrows indicate carrier injection from electrodes and the MoO_3 CGL.

phosphorescent dopants of FIr6, $Ir(ppy)_3$, and PQIr, respectively. The optimized dopant/host combinations are chosen as FIr6: UGH2 for blue emission, $Ir(ppy)_3$: 4,4-N,N-dicarbazole-biphenyl (CBP) for green, PQIr:CBP for red. Doping concentrations are controlled between 8 wt% to 10 wt% for each cell. Finally, the cathode consisting of LiF (0.8nm) and Al (120nm) was deposited through a shadow mask with an array of 1.0 mm diameter openings. Note that for FIr6 device, a 10nm-thick layer of N,N-dicarbazoly1-3,5-benzene (mCP) is inserted between NPD and EML as an exciton blocking layer.[86]

3.2.3 Discussion

For balanced emission from each OLED element, it is necessary to control the weak microcavity effects in the stacked device. To optimize the structure, therefore, the extraction efficiencies of the R, G, and B cells in the stacked structure are calculated based on transfer matrix simulations. The complex refractive indices of organics, ITO and MoO_3 employed in the simulation are 1.7, 1.9-0.036j and 1.9-0.3j respectively. By moving three EMLs close to their corresponding optical antinodes, the order of

(a)

Structure:		
Aluminum	150nm	1.031-6.861j
LiF	0.1nm	1.45-0.02j
Top Org Layer	120nm	1.7
MoO3	10nm	1.9-0.3j
Middle Org Layer	120nm	1.7
MoO3	10nm	1.9-0.3j
Bottom Org Layer	120nm	1.7
ITO	160nm	1.9-0.036
Glass substrate	1mm	1.48

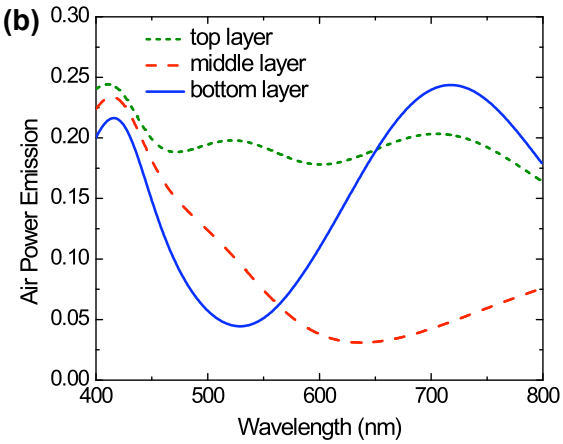

Figure 3.9: (a) Structure of SOLED for optical simulations. (b) Power extracted from SOLED considering microcavity effect for top layer (short dashed line), middle layer(dashed line), and bottom layer(solid line).

B-G-R (with R adjacent to the ITO anode) leads to the optimal color balance, with CIE coordinates (0.39, 0.42) and CRI = 79 (Figure 3.11, solid line) at a current density of J=10mA/cm^2, estimated to result in a luminance >1000cd/m^2. Note that two assumptions are made in this analysis: (i) each of the three dopant/host combinations has an internal quantum efficiency (IQE) equals to 100%, and the numbers of photons generated from each element are equal at a given current density, J; and (ii) the EQE of the stacked device follows the same roll-off behavior at high currents as each element, as shown in Figure 3.12. The first assumption, as shown below, critically depends on the charge transport and injection properties of the CGLs for each element.

The charge injection efficiency from the CGL plays a significant role in determining the output spectrum. Injection from ITO is more efficient than from MoO_3. The experimental spectra of this optically optimized RGB SOLED shows distinct differences from calculation, with the PQIr peak intensity 4-5 times stronger than that of FIr6. This indicates that, besides optical effects, the injection efficiency of charges

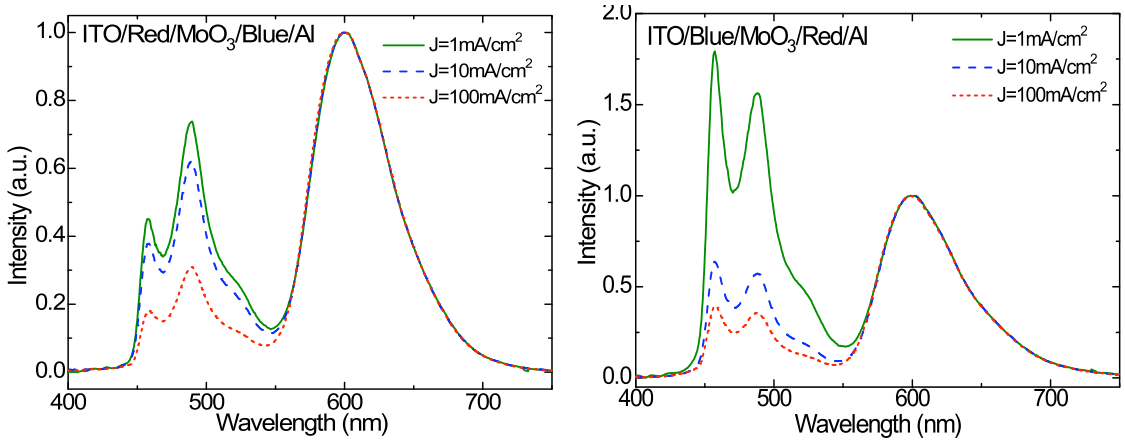

Figure 3.10: Measured spectra of (a) RB and (b) BR SOLED at various current densities: J=1mA/cm^2 (solid line), J=1mA/cm^2 (dashed line), J=100mA/cm^2 (short dashed line).

from the CGL indeed plays a significant role in determining the output spectrum. We find that injection from ITO is more efficient than from MoO_3 used in the stacking configuration in Figure 3.8. The optically optimized spectrum of this structure is shown in Figure 3.11, dashed line.

The EQE and PE of the RGB SOLED in Figure 3.8, and the monochrome OLED control devices, measured in an integrating sphere, are shown in Figure 3.12. Blue, green and red controls exhibit EQEs peak at $(13.9 \pm 1.0)\%$, $(17.5 \pm 1.0)\%$, and $(20.1 \pm 1.0)\%$, respectively, typical for OLEDs based on this set of phosphor dopants and hosts. The total EQE and PEs for the RGB SOLED have maxima at $\eta_{ext} = (36 \pm 2)\%$ at a current density of $J = 82\mu$A/cm^2, and $\eta_p = (21 \pm 1)$lm/W at $J = 17\mu$A/cm^2, respectively. These values roll off to $(32 \pm 2)\%$ and (13 ± 1)lm/W at 1000cd/m^2 corresponding to J=2mA/cm^2. The maximum EQEs of the RGB SOLEDs are approximately the sum of the EQEs of the three individual elements over a wide range of current densities, indicating that the losses at the transparent CGL are minimal. A fit of SOLED EQE is shown in solid line, yielding an emission intensity ratio 0.7:0.5:1 in the B, G, and R elements. This dependence of exciton formation on position in the stack is attributed to the injection efficiencies of the

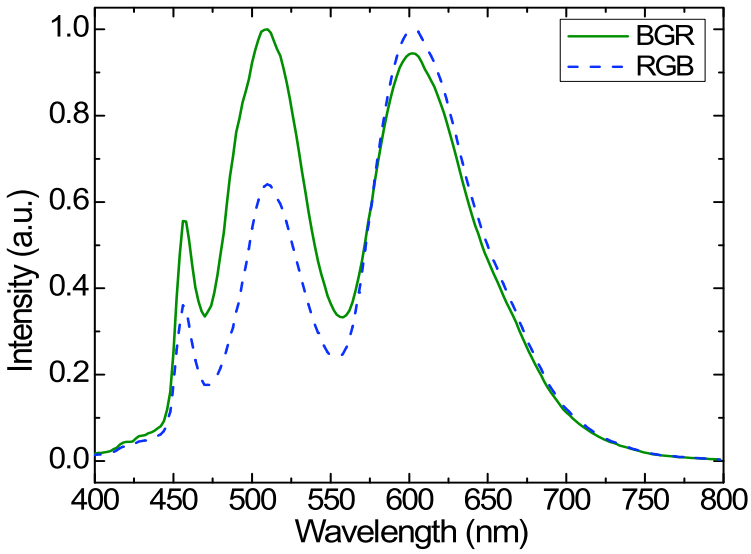

Figure 3.11: Spectra of the optically optimized B-G-R (with R adjacent to the ITO anode) ordered device (solid line) and the spectrum of the R-G-B ordered structure (dashed line).

CGLs and the ITO anode.

Table 3.1: IQEs and η_{Ph} generated from the elements in the RGB SOLED.

	IQE			η_{Ph}		
$J(mA/cm^2)$	1	10	100	1	10	100
$R(top)$	0.69	0.67	0.48	1.00	1.00	1.00
$G(middle)$	0.84	0.65	0.42	0.45	0.64	2.22
$B(bottom)$	0.52	0.33	0.15	0.73	0.82	1.44

Figure 3.13 (a) shows the experimental and simulated electroluminescence spectra for the RGB SOLED at several current densities. The CIE coordinates and the CRI values are (0.45, 0.36) and 63 at J=2mA/cm^2 (corresponding to 1000cd/m^2), and (0.36, 0.37) and 78 at J=100mA/cm^2. Simulated spectra are based on our optical model, and are used to determine the fraction of photons generated from each cell, with values listed in Table 3.1. Note that NPD emission was observed to increase in intensity with J. Due to the relatively inefficient electron injection from MoO_3

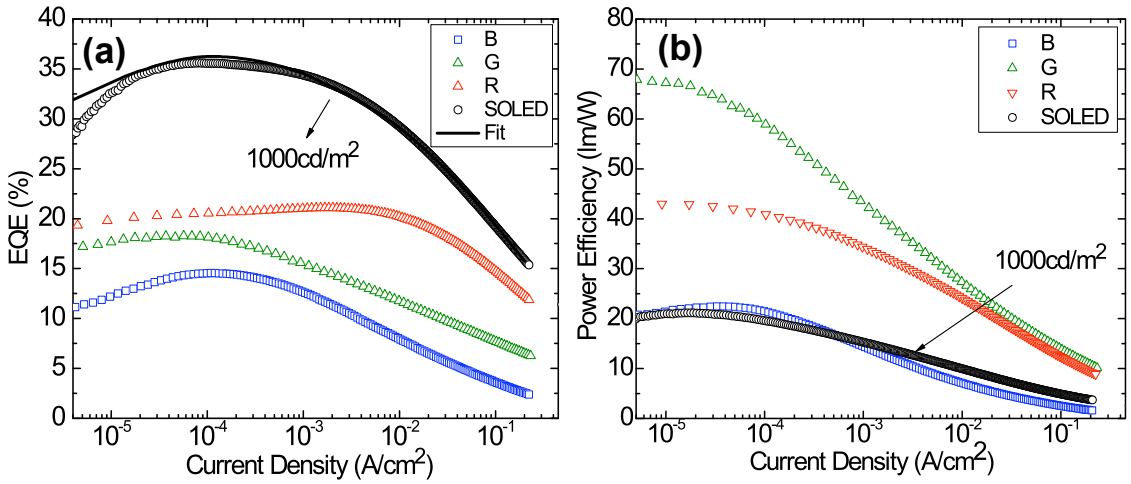

Figure 3.12: (a) Total EQE of the RGB SOLED (open circles) along with taht for the monochrome control devices. The solid line is a fit to the SOLED EQE, which is the weighted sum of the monochromes device efficiencies. (b) Total PE of the RGB SOLED and the control devices. Arrows indicate values at a brightness of 1000 cd/^{2}.

as compared to that of the Al cathode, electrons can concentrate at the MoO_3/NPD interface, leading to some exciton formation on the NPD layer. To test this hypothesis, a two-color RG SOLED was grown, one with a 50nm-thick BPhen layer adjacent to the CGL, and the other with only a 30nm-thick BPhen layer. No NPD emission is observed in the first case, nor for the red and green control devices, while a strong NPD signal is observed for the structure with thinner Bphen.

In Figure 3.13 (b) we show the current density vs. voltage characteristics of the SOLED and the R, G and B control devices. There exists excess drive voltage on the SOLED compared with the sum of that on all three control devices (solid line). This effect, due to energy barriers at the CGL, accounts for a concomitant reduction of $(10.3 \pm 0.7)\%$ in power efficiency.

Table 3.1 provides IQEs and the fraction of photons generated from the three stacked elements. As current density increases, we observe an increase of exciton formation on the blue and green elements with respect to that of the red element.

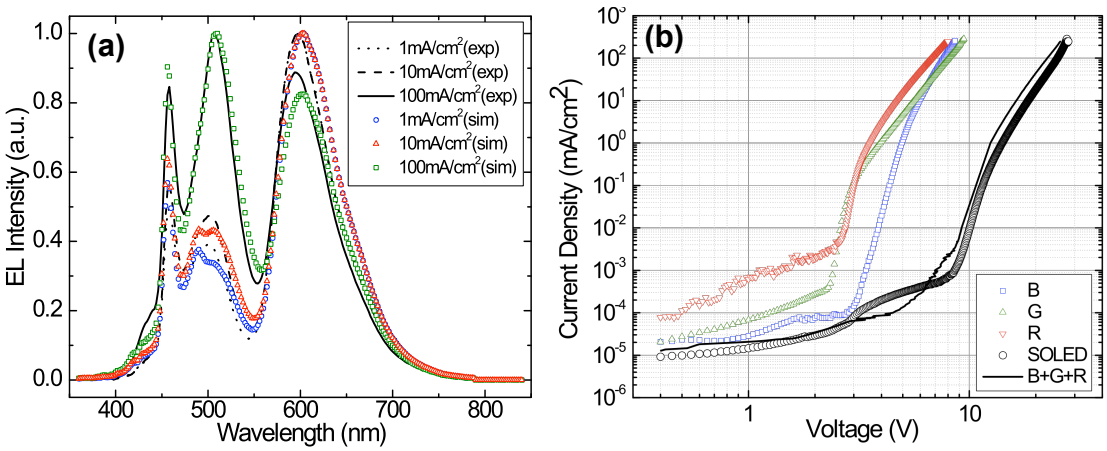

Figure 3.13: (a) Measured and simulated spectra of the RGB SOLED at several current densities. Simulated spectra are based on cavity enhancement and extraction efficiencies by fitting the ratios of photons generated from the constituent R, G, and B elements. (b) The J-V characteristics of the RGB SOLED and the monochrome control devices. The solid line is the sum of the currents of the three control devices, which in the absence of losses, would be equal to the RGB SOLED J-V characteristics.

This indicates current dependence of electron and hole injection efficiency from CGLs.

In summary, we have demonstrated an all phosphorescent RGB SOLED using a compound MoO_3/Li:BPhen transparent CGL. White emission and SOLED efficiency were optimized by making a trade-off between the color emissive element ordering to achieve efficient charge injection and a maximum outcoupling efficiency at a high CRI. The device reaches a maximum total external quantum and power efficiencies of $\eta_{ext} = (36 \pm 2)\%$ and $\eta_p = (21 \pm 1)$lm/W, respectively. These results demonstrate electrophosphorescent RGB SOLEDs represent a promising architecture for achieving high brightness and efficiency for indoor lighting. Besides the novelty of this structure in achieving white light, the stacked structure with CGLs sandwiched between phosphorescent EMLs with distinct emission spectra, can be used as a means for understanding the mechanisms for charge generation and injection processes.

CHAPTER IV

Charge Generation Mechanisms in a Multilayer Stack

4.1 Charge Generation Overview

As reported in Chapter 3, stacked OLEDs provide a way to significantly reduce the stress on each light-emitting unit while still achieving a given luminance level, and therefore ensures a longer operation time. The interconnecting unit CGL is commonly employed in such a multilayer OLED as a means for establishing balanced injection into adjacent sub-elements in the stack.[114] With the application of an electric field, electrons and holes are generated in the CGL, and then injected into the adjacent ETL and HTL, respectively. When N emission units are vertically stacked in series, the driving voltage increases N-fold compared to that of a conventional OLED with one emission unit under the same current density. The CGL has its applications in white illumination where red, green, and blue emission units are combined for high quality white emission. This structure has two main advantages: i) it avoids the trade-off between luminance and lifetime in high-luminance applications, and ii) red, green and blue emission can be separately obtained from independently stacked emission units, allowing flexibility in white emission.

4.1.1 Charge Generation Fundamentals

The first report on CGL by Kido *et. al.* [115] suggested that ITO adjacent to a HTL leads to the generation of holes and electrons upon application of an electric field. Various concepts for CGL structures have been reported since this work. There are different device architectures that provide the charge generation functionality. One is to use junctions between chemically *p*- and *n*-doped charge transport layers, i.e., the organic *p*-*n* junction [116, 117, 108]; the other is to use a doped organic/inorganic layer. For the latter architecture, a transition metal oxide (TMO) such as V_2O_5, MoO_3, and WO_3 allow for the realization of very efficient stacked devices.[106, 104, 118, 119, 120, 121] To optimize such layers, an understanding of the charge generation mechanism must be developed. The charge generation mechanism for a doped organic *p*-*n* heterojunction is interpreted as a temperature-independent field-induced charge separation supported by interface band bending.[122] However the physics of the metal-oxide-based carrier generation process has not yet been fully explored.

In this work, we study both the electron and hole injection in MoO_3 CGLs using temperature-dependent current-voltage and capacitance-voltage characteristics. A compound CGL consisting of 100-Å-thick MoO_3, and Li-doped BPhen in a 1:1 molar ratio, is demonstrated to have a high electron generation efficiency. A model for charge injection via a two-step process consisting of tunneling-assisted thermionic emission over an injection barrier of (1.2±0.2)eV and a trap level due to oxygen vacancies at (0.06±0.01)eV above the MoO_3 valence band edge is shown to accurately predict CGL performance. An optimized, three-element green-emitting electrophosphorescent SOLED is fabricated based on these results. Peak EQEs of $(10.5 \pm 0.2)\%$, $(10.1 \pm 0.2)\%$, $(8.6 \pm 0.2)\%$, and $(8.9 \pm 0.2)\%$ are obtained for SOLED sub-elements with ITO anode/CGL cathode, CGL anode/CGL cathode, CGL anode/Al cathode, and ITO anode/Al cathode contacts, respectively.

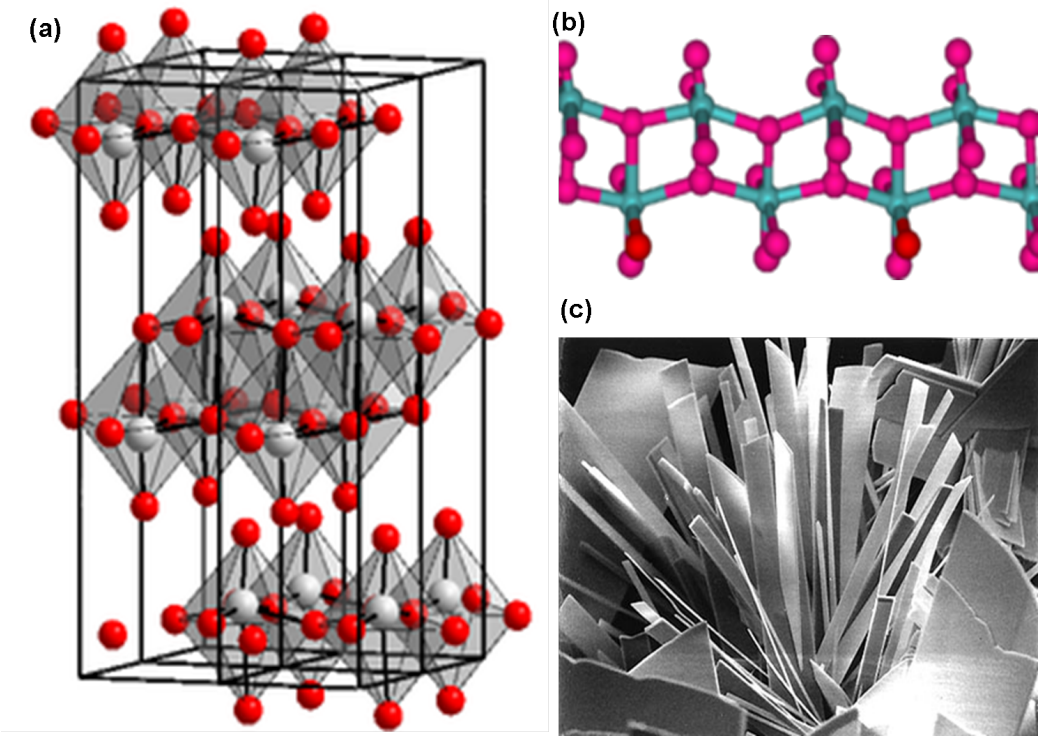

Figure 4.1: (a) Crystal structure of MoO_3; (b) A section of the chain comprising edge-sharing octahedra; (c) SEM image of MoO_3 crystals(Image courtesy of ISU).

4.1.2 Transition Metal Oxide

TMO is a class of materials that contain transition elements and oxygen. They exhibit a rich collection of interesting and intriguing properties, which can be tailored for a wide variety of applications. Many TMOs have been prepared in bulk form or in thin films, which paved the way for intensive research studies in the past several decades.

MoO_3 has the oxidation state of +6. In the gas phase, three oxygen atoms are double-bonded to the central molybdenum atom. In the solid state, anhydrous MoO_3 is composed of layers of distorted MoO_6 octahedra in an orthorhombic crystal. As shown in Figure 4.1 (b), oxygen atoms above and below the chain link to other chains to build the layer.

4.2 Compound Charge Generation Layers

We already discussed efficient R-G-B SOLEDs (see Chapter III) using transparent CGLs consisting of MoO_3 adjacent to Li-doped BPhen.[114] The device yielded a peak total EQE and PE of $\eta_{ext} = (36 \pm 2)\%$ and $\eta_p = (21 \pm 1)$lm/W at current densities of $J = 82\mu$A/cm^2, and $J = 17\mu$ A/cm^2, respectively. Both the high efficiency and white balance achieved in this SOLED indicate that efficient charge generation and injection can be obtained using MoO_3,[105] and the results may be generalized to other compound CGLs such as Mg: Alq_3/WO_3, and Mg: Alq_3/V_2O_5. [123, 124]

To further understand and optimize the CGL architecture, here we systematically study the charge generation in compound CGLs based on transparent metal oxides. We analyze the J-V and C-V characteristics of electron- and hole-only devices consisting of MoO_3 layers with varying thicknesses, and over a wide range of temperature. Optimized performance of Li: 2,9-dimethyl-4,7-diphenyl-1,10-phenanthroline (BCP)/MoO_3 CGL is demonstrated by varying both the thickness of MoO_3, as well as the Li doping ratio in BCP. Thermally assisted tunneling from a trap level at (0.06 ± 0.01)eV above the MoO_3 valence band maximum into the adjacent organic layer is proposed to explain the temperature dependence of the J-V characteristics in both electron- and hole-only devices. The results show the importance of maintaining charge balance in each subelement to achieve high quantum efficiency.[125] Based on our analysis, we demonstrate a three-element green electrophosphorescent SOLED whose energy-level diagram is shown in Figure 3.8, establishing charge balance and comparable efficiency for each element in the stack having a different anode/cathode combination.

4.2.1 Introduction

We base our analysis on the hypothesis that electron injection occurs via thermionically excited electrons into traps due to oxygen vacancies located at energy, ϕ_t, above

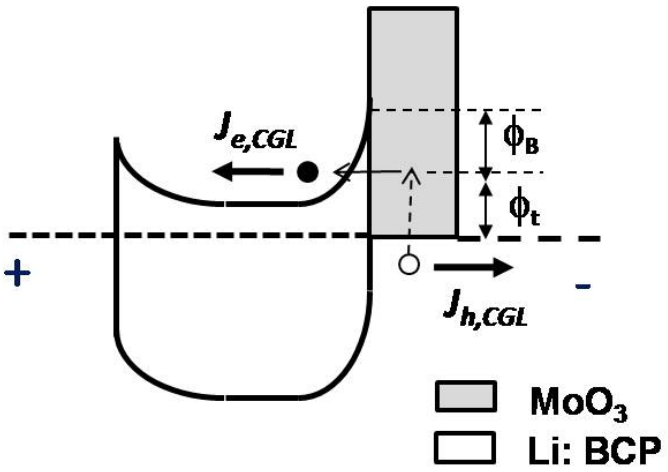

Figure 4.2: Energy level of CGL in the proposed thermally assisted tunneling model, where ϕ_t is the trap level with respect to MoO_3 valence band maximum, and ϕ_B is the tunneling barrier. Holes (open circles) and electrons (solid circles) are dissociated under the electric field, resulting in current density of $J_{h,CGL}$, and $J_{e,CGL}$, respectively.

the MoO_3 valance band maximum, as shown in Figure 4.2. This is followed by field-assisted tunneling through the thin depletion region of the adjacent, doped organic layer. At applied voltage, V, the electron ($J_{e,CGL}$) and hole ($J_{h,CGL}$) current densities in the CGL interface region in Figure 4.2 follow:

$$J_{e,CGL} = J_{h,CGL} = qv_eN_tfP(V) \tag{4.1}$$

where $f = 1\,(1 + exp[q\phi/kT])$ is the Fermi-Dirac function, q is the elementary charge, k is Boltzmann's constant, T is the temperature, ϕ_t is the trap level above the MoO_3 valence band maximum, v_e is the free electron velocity [126], N_t is the trap concentration, and $P(V)$ is the tunneling probability over an interface barrier of height, ϕ_B [127]. Now,

$$P(V) = exp[-\frac{\alpha}{E(V)}\phi_B^{3/2}] \tag{4.2}$$

where $\alpha = 4\sqrt{2m_s^* q}/3\hbar$ for a triangular energy barrier. Here, $E(V)$ is the electric field at voltage, V, m_s^* is the electron effective mass in the organic semiconductor, and $\hbar$ is the Planck's constant divided by 2π.

We note that in earlier work, F-N tunneling has been used to explain the conduction characteristics of metal oxides diodes such as Al-Al_2O_3-Au. While a weak temperature dependence observed in that work was attributed to compensation effects[128] that follow an Arrhenius equation, to our knowledge no *quantitative* fit to that temperature dependence, as (in Equation 4.1) has been shown.

Aside from providing efficient carrier injection, the CGL must establish charge balance in adjacent sub-elements in a stacked device. Charge balance can be realized by the use of blocking layers [129], or by balanced carrier injection. For a discrete OLED, charge balance is maintained by ohmic injection of electrons and holes into the EML. This process is more complicated in a SOLED considering the increased number of energy barriers to hole and electron injection that exist between counterelectrodes.

Now, the exciton generation rate at current density J is: [113]

$$G(J) = \int G(x,J)dx = \frac{1}{q}\int \frac{d[J_e(x)]}{dx}dx = -\frac{1}{q}\int \frac{d[J_h(x)]}{dx}dx \equiv \frac{1}{q}J\gamma \tag{4.3}$$

where $G(x,J)$ is the volume generation rate of excitons between positions x and $x+dx$ in the EML, with $x = 0$ taken at the EML/ETL interface. The integration is across the entire width of the EML. The charge balance factor, γ, is the ratio of holes to electrons injected into the EML [130], given by:

$$\gamma = \frac{J_{h,A} - J_{h,C}}{J} = \frac{J_{e,C} - J_{e,A}}{J} \tag{4.4}$$

where $J_{h,A}$, $J_{h,C}$, $J_{e,A}$, $J_{e,C}$ are the hole (h) and electron (e) current densities at the anode (A) and cathode (C) sides of the EML. For high-efficiency electrophosphorescent

OLEDs, the charge balance factor is near unity,[17] indicating that equal numbers of electrons and holes are simultaneously present in the recombination zone.

4.2.2 Experimental Techniques

Both the electron- and hole-only devices were prepared on detergent and solvent cleaned glass substrates that were immediately transferred into a vacuum chamber with a base pressure of 10^{-7} Torr after a 10-min exposure to a UV/ozone treatment.[131] For the electron-only device shown in Figure 4.3 (a), a 50-nm-thick Al cathode to minimize hole injection was deposited onto the glass substrate through a 1-mm-wide striped shadow mask. This was followed by the deposition of a 40-nm-thick layer of BCP and a 10-nm-thick Li-doped layer of BCP in a 1:1 molar ratio. On this surface, a layer of MoO_3 of different thicknesses (5, 10, and 20 nm) was deposited, followed by a second 50-nm-thick Al cathode deposited through 1-mm-wide striped shadow mask positioned perpendicular to the anode stripes. Similarly, for the hole-only device (see Figure 4.3 (b)), a 50-nm-thick Al electrode was deposited onto the glass substrate, followed by the deposition of a 10-nm-thick Li-doped BCP with 1:1 molar ratio, and MoO_3 of varied thicknesses (0, 5, 10, and 20 nm). Then 40-nm of 4,4'-bis[*N*-(1-naphthyl)-*N*-phenyl-amino]-biphenyl (NPD) was deposited as a HTL, followed by a 50-nm-thick MoO_3 electron blocking layer (EBL), and capped by a 50-nm thick Al cathode.

The ionization potentials and work functions used in the energy-level diagrams have been taken from the literature.[132] Note, however, that there remains disagreement for some of these values, with the range particularly large for MoO_3.[133] For the purposes of this work, we use a work function of 5.7 eV,[132] consistent with the values obtained for material deposited using methods similar to those employed here. For example, recent experiments [134] replacing MoO_3 with an organic thin film as an electron blocking layer provides additional support to our choice of the MoO_3

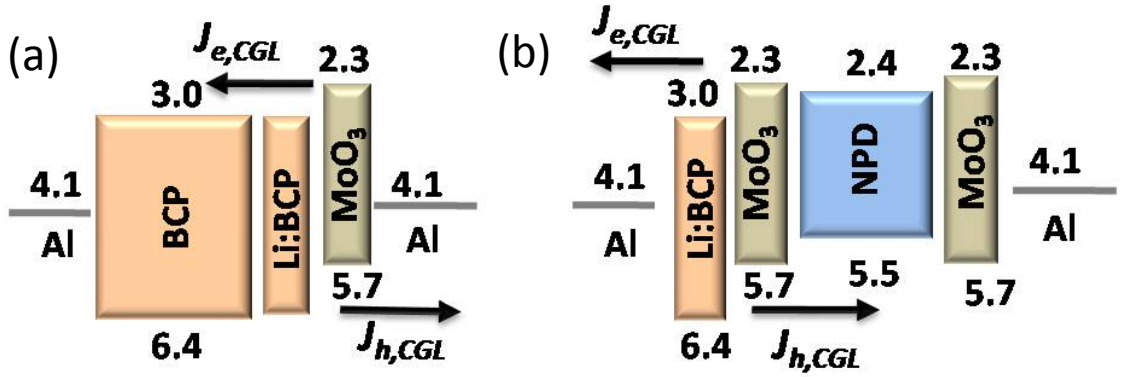

Figure 4.3: Energy diagrams of the (a) electron-only, and (b) hole-only devices.

valence band energy given in Figure 4.2. Finally, photoelectron spectroscopic data in our laboratory (to be reported elsewhere) obtained for the film growth methods and material compositions used here are consistent with the more shallow assignment of the valence maximum.

For characterization, samples were mounted in a cryostat where the temperature was varied from 159 to 296K, and J-V characteristics were measured using a parameter analyzer (HP 4145B). The C-V measurements employed an impedance/gain-phase analyzer (HP 4194A), from which we infer the free carrier concentration and position of the interface barrier. The C-V measurements were obtained at a frequency of 200 Hz, which is sufficiently low to allow for dielectric relaxation.[107] Optical characterization of the devices employed a calibrated detector reference using standard methods described previously.[135]

4.2.3 Results

The room temperature J-V characteristics of the electron-only device with MoO_3 thicknesses of 50, 100, and 200$\mathring{A}$, are shown in Figure 4.4 (a). For electron injection, the Al electrode on the BCP side is positively biased relative to the Al electrode on the MoO_3 side. The lack of rectification of the J-V characteristics indicates nearly

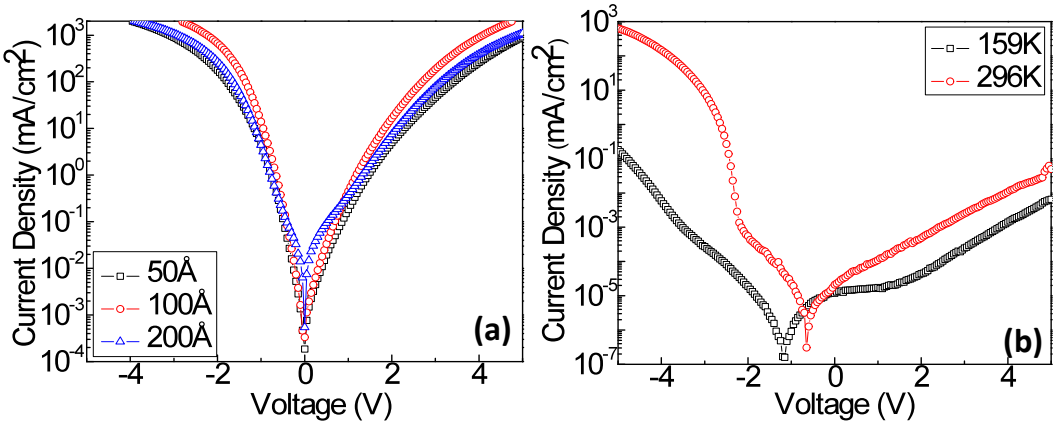

Figure 4.4: (a) Room-temperature J-V characteristics of the electron-only devices with MoO_3 of thickness 50Å(square), 100Å(circle), and 200Å(triangle). (b) The J-V characteristics of the hole-only device (Al 500Å/Li:BCP 100Å/NPD 400Å/MoO_3 50Å/Al 500Å) at 159K (open square) and 296K (open circle).

equally efficient electron injection from the CGL and the cathode [122]. Under forward bias (V>0), a dependence on MoO_3 thickness is observed, with 100$\mathring{A}$ the optimized thickness for the electron-only devices. Figure 4.4 (b) shows the hole-only device with no MoO_3 introduced, the current densities at a given forward bias are reduced with the temperature ranging from 296K to 159K, and a rectification ratio of $\sim 10^4$ at $\pm$5V is observed at room temperature.

The C-V characteristics of the electron-only devices are shown in Figure 4.5 (a). Depletion layer widths calculated from the capacitance [136] are shown in Figure 4.5 (b). In Figure 4.5 (c), the effect of different free carrier concentrations on interface depletion width is demonstrated for CGLs with a 100-$\mathring{A}$-thick layer of MoO_3. The concentration of Li in BCP are varied from 1:1 to 1:10 molar ratio, corresponding to depletion widths of 24$\mathring{A}$ and 85$\mathring{A}$, respectively. The device without Li doping shows a fully depleted region with a thickness of 110$\mathring{A}$.

The current densities as functions of $1/E(V)$ for various temperatures ranging

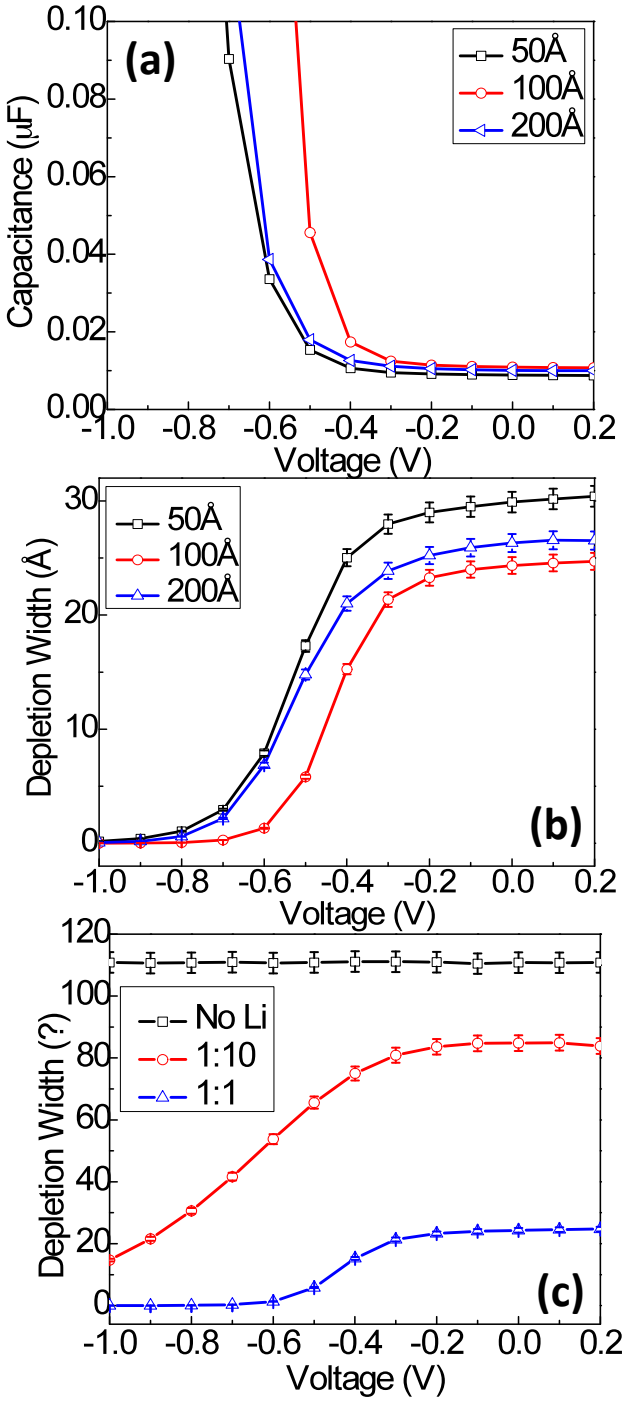

Figure 4.5: (a) The C-V characteristics and (b) the calculated depletion widths of the electron-onl devices with MoO_3 of the thickness 50Å(square), 100Å(circle), and 200Å(triangle) at the frequency of 200Hz. (c) Calculated depletion widths of the electron-only devices with 100-Å-thick MoO_3 with Li:BCP in a 1:10 molar ratio (circle) and Li: BCP in a 1:1 molar ratio (triangle), and without Li doping (square).

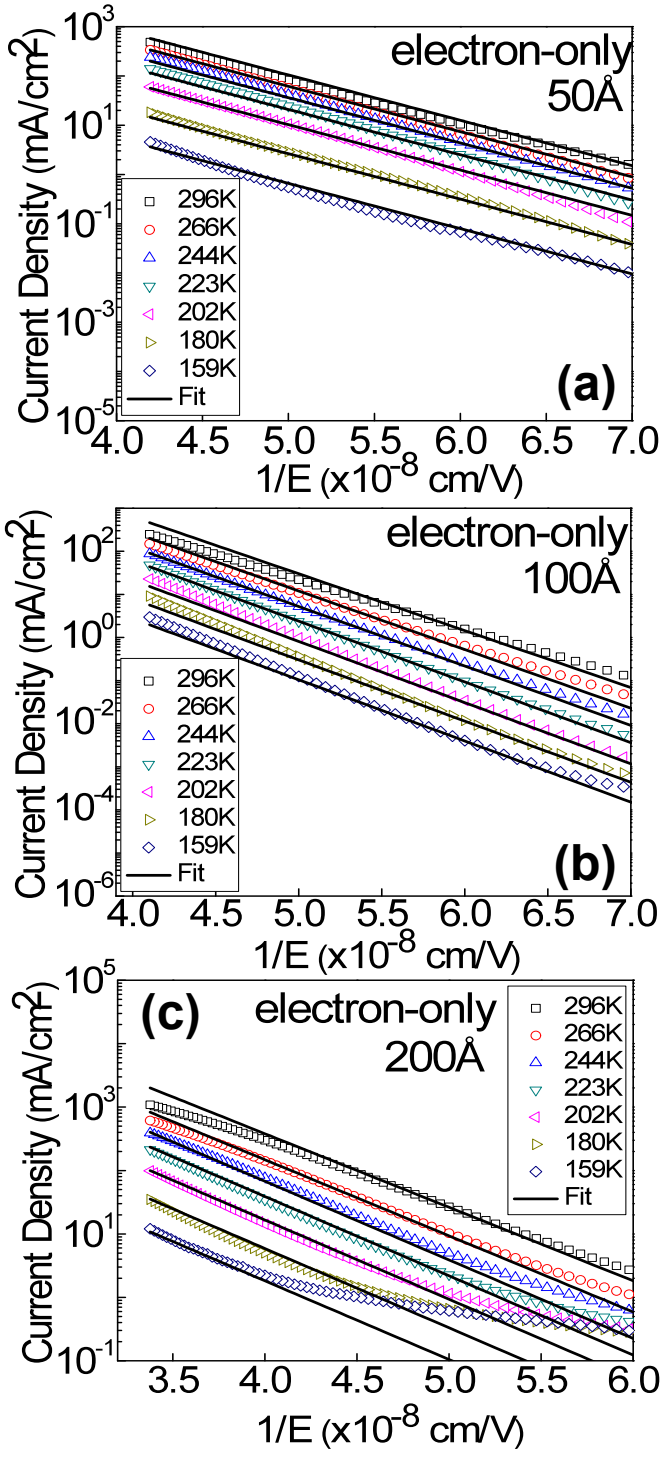

Figure 4.6: Current density as a function of inverse electric field for elctron-only device with MoO_3 thicknesses of (a) 50Å, (b) 100Å, and (c) 200Åunder the temperature varying from 159K to 296K. The solid lines are fits according to the tunneling-assisted thermionic emission model.

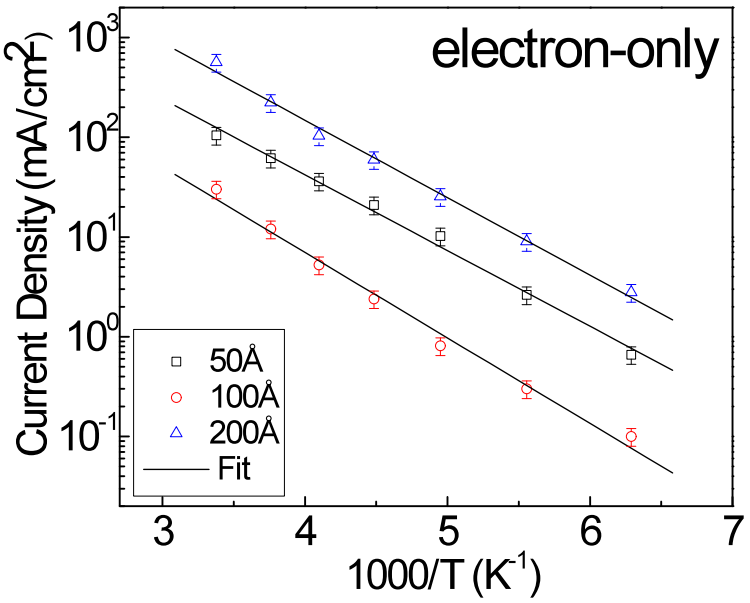

Figure 4.7: The current density as a function of $1000/T$, where T is the temperature for the electron-only device at an applied electric field $E = 2.0 \times 10^7$V/cm, except for the device with 200-Å-thick MoO_3. $E = 2.6 \times 10^7$V/cm is used. The fits (solid lines) yield the trap energy level, ϕ_t, listed in Table 4.1

from 159K to 296K are plotted for electron-only (Figure 4.6) devices shown in Figure 4.3. Here, the electric field is taken as the ratio of the applied voltage, after subtracting the 2.7V built-in potential, to the charge generation layer thickness due to the high conductivity of the Li:BCP layer. Small voltage drops at the contact/organic layer interface are neglected. In Figure 4.7, the current densities J as functions of $1000/T$ are plotted under the electric field $E = 2.0 \pm 10^7$V/cm, from which we obtain trap activation energy ϕ_t. Corresponding plots for hole-only devices are shown in Figure 4.8 and Figure 4.9, respectively.

4.2.4 Thermally Assisted Tunneling

The presence of MoO_3 is required for efficient charge generation, as shown by a comparison of Figure 4.4 (a) and (b). Under reverse bias, both Al contacts are nearly ohmic due to the high Li concentration in BCP, as well as due to the 50-Å-thick

MoO_3 between the NPD and the Al cathode which, in combination, enhance hole injection. Under forward bias, however, both electron and hole injection are reduced at the electrodes, and the current density is a result of the carrier generation from the CGL. With efficient injection and transport facilitated for both electrons and holes under both reverse and forward bias, symmetric J-V characteristics are observed for electron-only devices with various MoO_3 thicknesses, as shown in Figure 4.4 (a). Among the CGLs with varied thicknesses of MoO_3, the device with a 100-$\mathring{A}$-thick CGL shows an optimized generation efficiency, with a current three to four times higher than for 50- and 200-$\mathring{A}$-thick MoO_3 layers at $>2V$ under forward bias. The MoO_3 is too thin to result in complete and uniform coverage at $50\mathring{A}$, hence reducing injection at this interface, while thicknesses $>100\mathring{A}$, tunneling injection is exponentially reduced.

The J-V characteristics of the hole-only devices yield a similar dependence on MoO_3 thickness. Shown in Figure 4.4 (b) are the J-V characteristics of a hole-only device without MoO_3, with the structure Al ($500\mathring{A}$)/ Li:BCP ($100\mathring{A}$)/ NPD ($400\mathring{A}$)/ MoO_3($100\mathring{A}$)/Al ($500\mathring{A}$). Inefficient carrier generation was observed under forward bias due to the absence of MoO_3, resulting in a rectification ratio of $\sim 10^4$ at $\pm 5V$ at room temperature. The hysteresis behavior at 159K, shown in Figure 4.4 (b) where zero current occurs at -1.2V for voltage swept from -5 to 5V, is possibly due to electron capture at defect states in MoO_3 introduced during film deposition. [137]

To understand the thickness dependence of the charge carrier generation efficiency, C-V measurements for the electron-only devices are shown in Figure 4.5 (a). The depletion widths in the doped BCP layer, are $30\mathring{A}$, $24\mathring{A}$ and $26\mathring{A}$ for CGLs with MoO_3 thicknesses of $50\mathring{A}$, $100\mathring{A}$, and $200\mathring{A}$, respectively (Figure 4.5 (b)). The relative static permittivity used to determine the carrier concentration is 3.0 for the organic layers. [138] In the case of 1:1 Li:BCP, the electron concentration in BCP is calculated to be $N_d = 10^{19} \sim 10^{20}\text{cm}^{-3}$ from the depletion width of $24\mathring{A}$.[139] This is in agreement with the 1:1 molar ratio of Li:BCP doping concentration, suggesting one electron

per Li atom. The estimation of N_d here is relatively larger than previously reported ($\sim 10^{18}\text{cm}^{-3}$) from conductivity measurements, where the formation of a BCP-Li complex was suggested to explain the difference of Li doping concentration and the carrier density of the doped film. The doped BCP layer ensures a very thin depletion layer that allows for efficient electron injection.[140] Since the tunneling probability is an exponential function of tunneling distance, the 100-$\mathring{A}$-thick MoO_3 sample, with a depletion width of $24\mathring{A}$, results in the highest tunneling injection efficiency compared to the other thicknesses used.

To extract energy barrier ϕ_B, the J vs. E^{-1} characteristics of the electron-only devices with various MoO_3 thicknesses are plotted in Figure 4.6, where E is calculated by subtracting the built-in potential, 2.7V, from the applied voltage. Since Li:BCP and MoO_3 are highly doped n- and p-type semiconductor materials, respectively, the built-in potential at the Li:BCP/MoO_3 junction is determined by the difference between BCP LUMO (3.0eV) and MoO_3 valence band maximum (5.7eV).[132] Linear relationships in $log(J)$ vs. E^{-1} are observed for devices in the temperature range from 296K to159K. Energy barriers, ϕ_B, obtained from the fit of Equation 4.1 to these data are listed in Table 4.1.

Table 4.1: Tunneling barrier, ϕ_B, trap depth, ϕ_t, and trap density, N_t, of electron- and hole-only devices vs. MoO_3 thickness.

Devices		$50\mathring{A}$	$50\mathring{A}$	$50\mathring{A}$
Electron-only	ϕ_B(eV)	1.1±0.1	1.3±0.1	1.2±0.1
	ϕ_t(eV)	0.07±0.01	0.06±0.01	0.06±0.01
	$N_t(\times 10^{18} cm^{-3})$	1.2±0.8	12.5±7.3	2.5±1.4
Hole-only	ϕ_B(eV)	1.1±0.1	1.0±0.1	1.0±0.1
	ϕ_t(eV)	0.08±0.02	0.09±0.02	0.09±0.02
	$N_t(\times 10^{18} cm^{-3})$	15.7±9.2	9.9±5.8	3.1±1.9

To extract the trap activation energy, ϕ_t, the current densities J vs. $1000/T$ for these same data are plotted in semi-logarithmic representations as shown in Fig-

ure 4.7. The slopes from linear fits yield $\phi_t = (0.06 \pm 0.01)$eV independent of MoO_3 thickness. The pre-factors $\sim 10^6$A/cm^2 are obtained from the intercepts for devices with MoO_3 thickness of from 50$\mathring{A}$ to 200$\mathring{A}$. Taking the electron thermal velocity of $v_e \sim 10^7$cm/s, we obtain a trap concentrations $N_t \sim 10^{18}$/cm^3, as shown in Table I. The comparatively small temperature dependence of $v_e (\sim T^{1/2})$ relative to the Fermi-Dirac term allows for its omission from the model without incurring significant error.

Similar plots for hole-only devices are shown in Figure 4.8 and Figure 4.9. The electric field within the CGL is more complicated to estimate than for electron-only devices due to the voltage drop across the undoped NPD. Hence, we fabricated the following device: ITO(1500$\mathring{A}$)/NPD(400$\mathring{A}$)/MoO_3(100$\mathring{A}$)/Al(500$\mathring{A}$) to determine the E. From these data, we obtain ϕ_B and ϕ_t, with the results also presented in Table 4.1. Agreement between the energies and trap densities obtained for both the electron- and hole-only devices provides significant support for our model.

4.2.5 Charge Generation Layers in Stacked Structure

To determine the effects of the charge generation efficiency on the performance of a green emitting SOLED with more than two sub-elements, OLEDs using the CGL as either a cathode (Cell-L), an anode (Cell-R), or both (Cell-M) were fabricated (see Figure 4.10 (a)), as well as the control device with an indium tin oxide (ITO) anode/Al cathode combination. Detailed structures are provided in Table 4.2. Note that for Cell-R and Cell-M, 20-$\mathring{A}$-thick Al was directly deposited onto ITO to ensure band alignment at the metal/organic interface [141], and thus to decrease the significant energy barrier that prevents electron transport from the CGL to the ITO.

The EQE and PE of each device are shown in Figure 4.12. The control device, with an ITO anode and LiF/Al cathode, shows a peak forward viewing EQE = (8.9$\pm$ 0.2)% at current density J=0.13mA/cm^2, similar to previously reported Ir(ppy)$_3$-

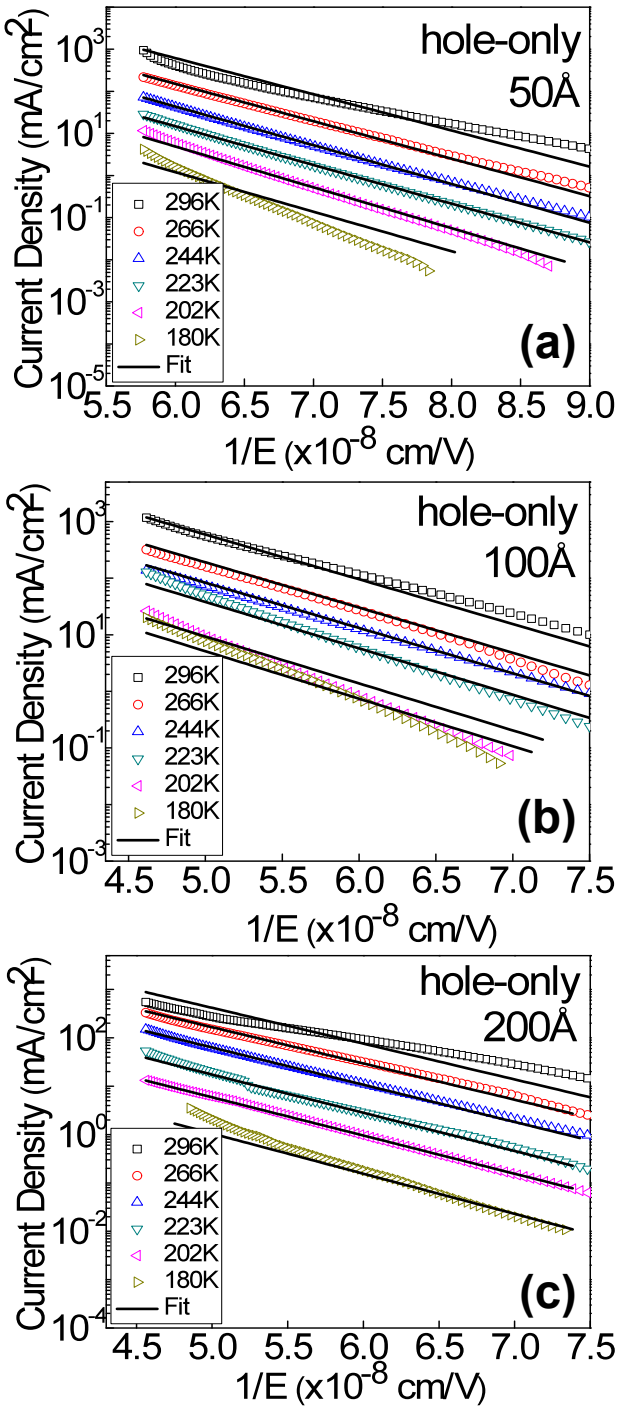

Figure 4.8: The current density as a function of the inverse electric field ($1/E$) for the hole-only device with MoO_3 thicknesses of (a) 50Å, (b) 100Å, and (c) 200 Åunder the temperatures varying from 180K to 296 K. The solid lines are fits according to the tunneling-assisted thermionic emission model.

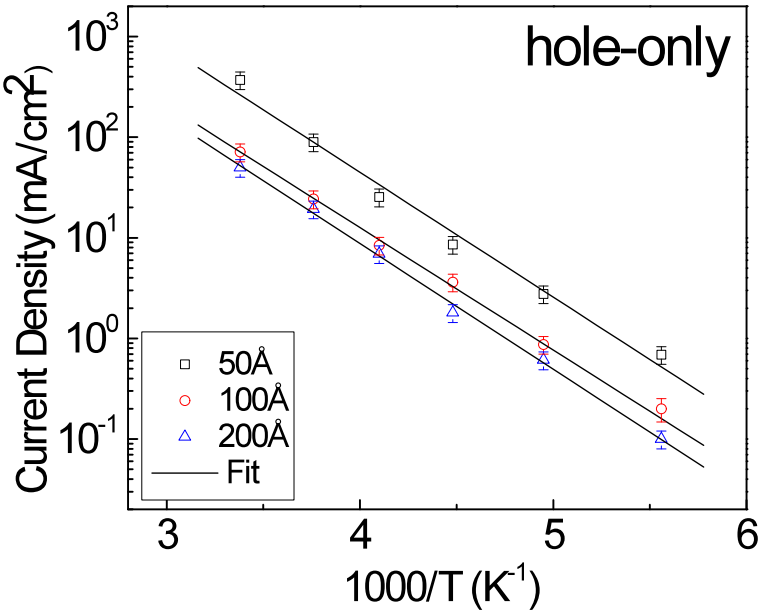

Figure 4.9: The current density as a function of $1000/T$, where T is the temperature for hole-only device at an applied electric field $E = 1.6 \times 10^7$V/cm. The fits (solid lines) yield the trap energy level, ϕ_t, listed in Table 4.1

based electrophosphorescent OLEDs. [142] A peak forward viewing EQE = $(10.5 \pm 0.2)\%$ is observed for Cell-L at J=0.37mA/cm^2, and EQE =$(10.6 \pm 0.2)\%$ at J = 39μA/cm^2 for Cell-M. In contrast, Cell-R shows a significantly reduced peak EQE = $(5.3 \pm 0.2)\%$ at a current density of J=0.92mA/cm^2. The PE for Cells-L, -M, and -R have maxima of (26 ± 1), (29 ± 1), and (15 ± 1)lm/W, respectively, compared to PE = (23 ± 1)lm/W for the control device (Figure 4.11).

Since no NPD emission is observed as a function of current density for cell-L, cell-M, or cell-R, we infer that there exists no electron leakage in the three devices. The improved electron transport to the EML achieved by the CGL in cell-L and cell-M leads to enhanced EQEs. In contrast, due to enhanced hole injection from a CGL anode, cell-R shows an EQE considerably less than that of the control OLED. As suggested by Eqs. 3 and 4, to achieve high efficiency and brightness, CGLs, used in varied contact combinations must provide for charge balance in each emitting element of which the structures have to be modified according to the contact combinations

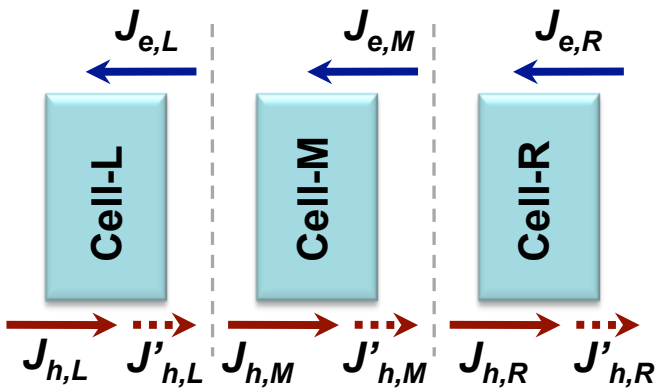

Figure 4.10: Schematic of the currents that establish charge balance in SOLED with three subelements. The directions of current densities are indicated by arrows. Parasitic leakage currents are indicated by the dashed lines.

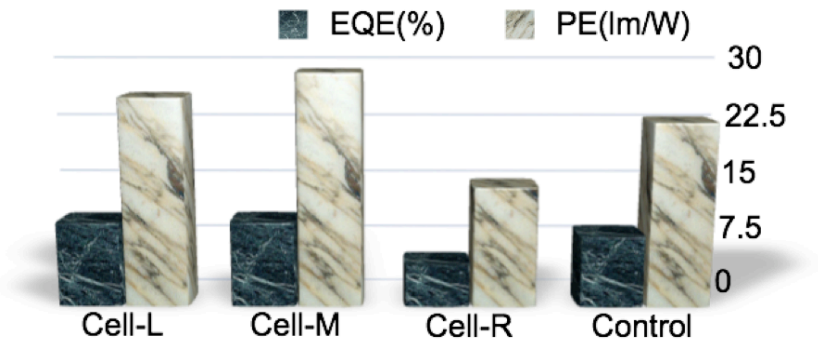

Figure 4.11: Comparison of cell-L, cell-M, cell-R, and the control cell.

for perfect charge balance. Note that optical interference effects introduced by CGLs and the thin Al layers in all three cells have been calculated based on transfer matrix simulations,[143] leading to only a small (3%) effect on the PEs, and hence cannot be the cause of the reduced EQE of Cell-R.

Table 4.2: Structure of the subcells in a three-layer SOLED and the control cell.

Devices	Layer functions	Materials	Thicknesses ($\AA$)
Cell-L	Anode	ITO	1500
	HTL	NPD	400
	EML	$Ir(ppy)_3$:CBP	250
	ETL	BCP	500
	CGL	Li:BCP/MoO_3	100/100
	Cathode	Al	500
Cell-M	Anode	ITO/Al	1500 /20
	CGL	Li:BCP/MoO_3	100/100
	HTL	NPD	400
	EML	$Ir(ppy)_3$:CBP	250
	ETL	BCP	500
	CGL	Li:BCP/MoO_3	100/100
	Cathode	Al	500
Cell-R	Anode	ITO/Al	1500/20
	CGL	Li:BCP/MoO_3	100/100
	HTL	NPD	400
	EML	$Ir(ppy)_3$:CBP	250
	ETL	BCP	500
	Cathode	LiF/Al	8/500
Control	Anode	ITO	1500
	HTL	NPD	400
	EML	$Ir(ppy)_3$:CBP	250
	ETL	BCP	500
	Cathode	LiF/Al	8/500

Comparing the efficiency of the control device with those of each sub-element in the stack, we obtain the following charge balance fractions for Cell-L, Cell-M, and Cell-R (see Figure 4.10):

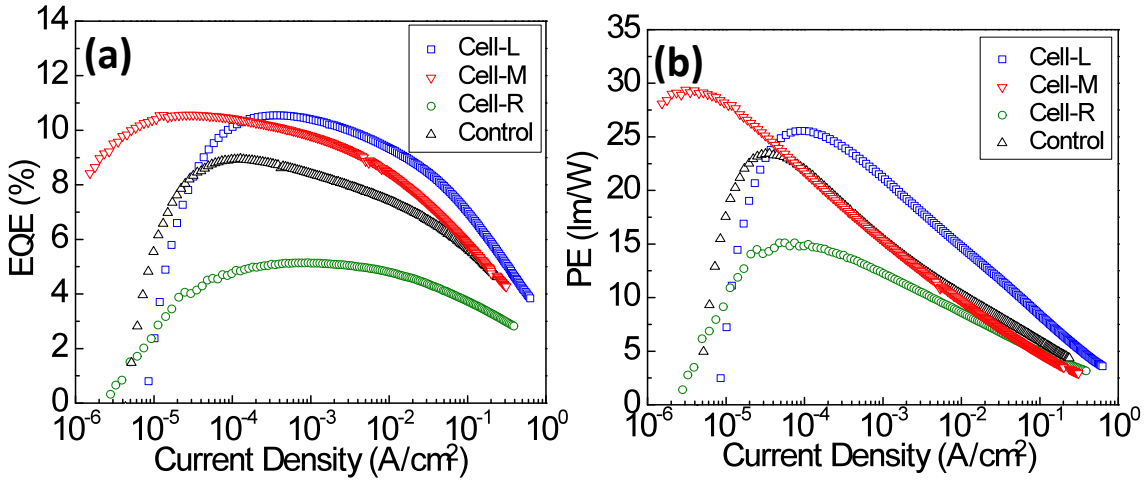

Figure 4.12: (a) EQEs and (b) PEs of Cell-L (open square), Cell-M (inverted triangle), Cell-R (open circle), and the control cell (triangle).

$$\gamma_{Cell-L} = \frac{J_{h,L} - J'_{h,L}}{J_{h,L}} = \frac{10.5\%}{EQE_{max}} \tag{4.5a}$$

$$\gamma_{Cell-M} = \frac{J_{h,M} - J'_{h,M}}{J_{h,M}} = \frac{10.1\%}{EQE_{max}} \tag{4.5b}$$

$$\gamma_{Cell-R} = \frac{J_{h,R} - J'_{h,R}}{J_{h,R}} = \frac{5.1\%}{EQE_{max}} \tag{4.5c}$$

Under charge neutrality at both electrodes, we have:

$$J_{h,L} = J_{e,R} + J'_{h,R} = J_{max} \sim 0.4 mA/cm^2 \tag{4.6}$$

Equation 4.5a- 4.5c then show that the charge balance factor of Cell-R is approximately 50% of that achieved in Cell-L and Cell-M, indicating a large hole current imbalance in Cell-R. With $EQE_{max} \sim 20\%$ achieved in Ir-based electrophosphorescence OLED, [17] we infer a hole leakage current of $J'_{h,R} = 0.30 mA/cm^2$, whose presence results in the significantly reduced EQE of that subelement.

To optimize Cell-R, the hole current was varied by using thicknesses of BCP

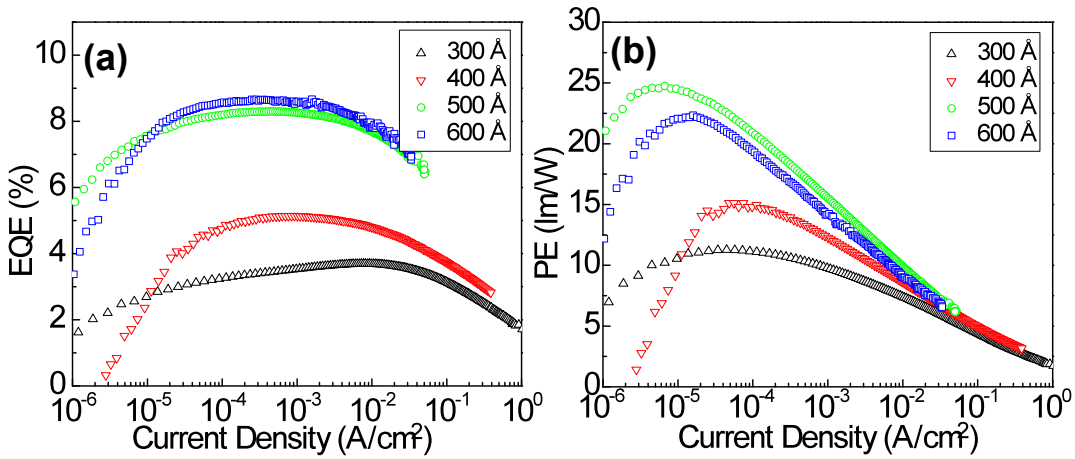

Figure 4.13: (a) EQEs and (b) PEs of Cell-R with various BCP thicknesses.

ranging from 300$\mathring{A}$ to 600$\mathring{A}$, as shown in Figure 4.13. Peak EQEs of $(3.7 \pm 0.2)\%$, $(5.1 \pm 0.2)\%$, $(8.3 \pm 0.2)\%$, and $(8.6 \pm 0.2)\%$ are observed for BCP thicknesses of 300$\mathring{A}$, 400$\mathring{A}$, 500$\mathring{A}$, and 600$\mathring{A}$, respectively. The corresponding power efficiencies have maximum values of (11 ± 1)lm/W, (15 ± 1)lm/W, (24 ± 1)lm/W, and (22 ± 1)lm/W. Increased EQEs and PEs are observed for the devices with BCP thicknesses of 500$\mathring{A}$ and 600$\mathring{A}$. Thus, by changing only the transport layer thickness (and hence its resistance), we are able to significantly improve cell efficiency, which supports the conclusion that charge imbalance in Cell-R is the primary mechanism for efficiency loss. Of the various means of achieving charge balance, ohmic hole and electron injection into the EML is optimal. Hence, employing charge blocking layers [128] as opposed to increasing layer resistance (as done here) provides the highest combination of PE and EQE for each element in the stack.

The EQEs and PEs of the GGG SOLEDs with varied BCP thicknesses in Cell-R, from 400$\mathring{A}$ to 600$\mathring{A}$, are shown in Figure 4.14 (a) and (b), respectively. Devices with 300$\mathring{A}$, 400$\mathring{A}$, 500$\mathring{A}$, and 600$\mathring{A}$-thick BCP exhibit forward-viewing EQEs peak at $(20.5 \pm 1.0)\%$, $(21.6 \pm 1.0)\%$, and $(24.3 \pm 1.0)\%$, and $(23.1 \pm 1.0)\%$, respectively,

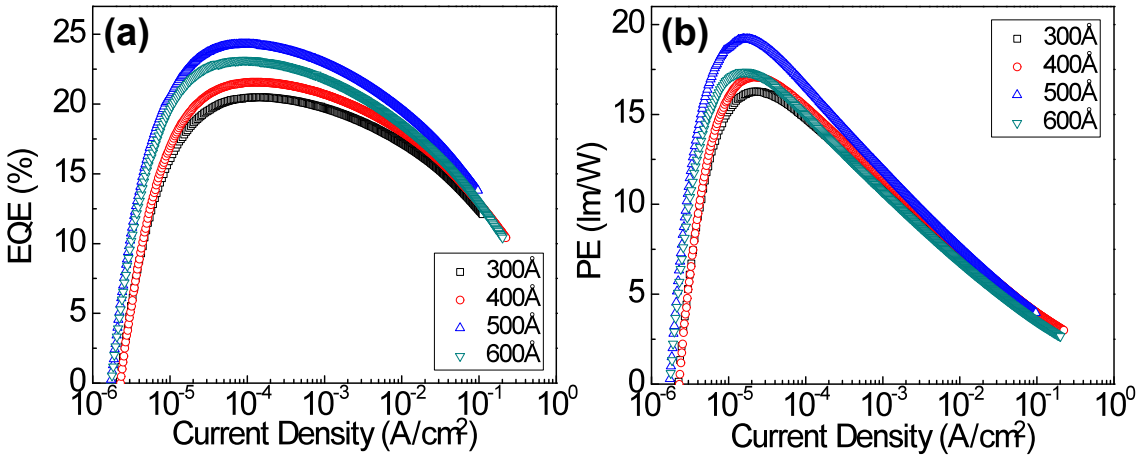

Figure 4.14: (a) EQEs and (b) PEs of GGG SOLED with various BCP thicknesses. Note that the results are consistent with the sum of a combination of the three discrete subelements in Figure 4.12 and 4.13.

at a current density of $J = 1.4 \times 10^{-4}$A/cm^2. The optimized GGG SOLED, with 500$\mathring{A}$-thick BCP in Cell-R, shows a peak forward-viewing PE=$(19 \pm 1)lm/W$ at the current density of $J = 1.7 \times 10^{-5}$A/cm^2, which rolls off to (12 ± 1)lm/W at 1000cd/m^2 corresponding to $J = 1.2 \times 10^{-3}$A/cm^2. The EQEs of the GGG SOLEDs are approximately the sum of the EQEs of the three individual OLEDs over a wide range of current densities, indicating that the losses at the transparent CGL are minimal.

Liao *et al.* [116] reported a similar Ir(ppy)$_3$-based GGG OLED where Li:tris(8-hydroxyquinoline)aluminum/$FeCl_3$:4, 4'-bis-(1-naphthyl-N-phenylamino)-biphenyl is used as the CGL. Comparison of our device performance with that of Liao et al., however, is difficult due to their use of cd/A for efficiency determination and the assumption that the SOLED is a pure Lambertian source (which is not accurate for devices that exhibit pronounced microcavity effects, as in this case). Nevertheless, it is reasonable to assume comparable efficiencies in both devices given that each stacked subelement is not expected to have an EQE$>$ 8$\sim$9%, as widely reported for discrete Ir(ppy)$_3$-based OLEDs.

We have modeled carrier generation from metal-oxide/doped organic interfaces

in SOLEDs based on electron injection via thermally assisted tunneling through a (1.2±0.2)eV barrier and an oxygen vacancy-induce trap level at (0.06±0.01)eV above the metal oxide (in this case, MoO_3) valence band maximum. Based on our model, we optimize a stacked green electrophosphorescent OLED with three sub-elements. The highest efficiency from all three elements in the stack is obtained when both carrier injection from the CGLs and the counter electrodes are all in balance. This requires different injection electrode combinations for each element, i.e. ITO anode/CGL cathode for the bottom (anode facing) element, CGL anode/CGL cathode for the central element, and CGL anode/Al cathode for the top (cathode facing) element. Charge balance was achieved by modifying the thickness of the carrier transport layer, although use of charge blocking layers to achieve balance in the sub-element emission layer should lead to higher PEs than obtained here.

4.3 Understanding MoO_3 Energetics

In our model, MoO_3 is assumed to be a p-type semiconductor with the valence band and conduction band located at 5.7eV and 2.3eV below vacuum level E_{vac}, respectively. However, Kröger et. al. recently reported a revised electronic structure of MoO_3, where the electron affinity and ionization energy of MoO_3 to be 6.7 and 9.68eV[133, 144], respectively, based on results obtained by UPS and IPES. With the deep lying conduction band at 6.7eV and a high work function of 6.9eV, their result suggests MoO_3 n-type, contradicting the thermally-assisted tunneling model we used to describe the charge generation in SOLED. Consequently, the CGL model in which the holes are claimed to be generated within the TMO has to be considered in this context.

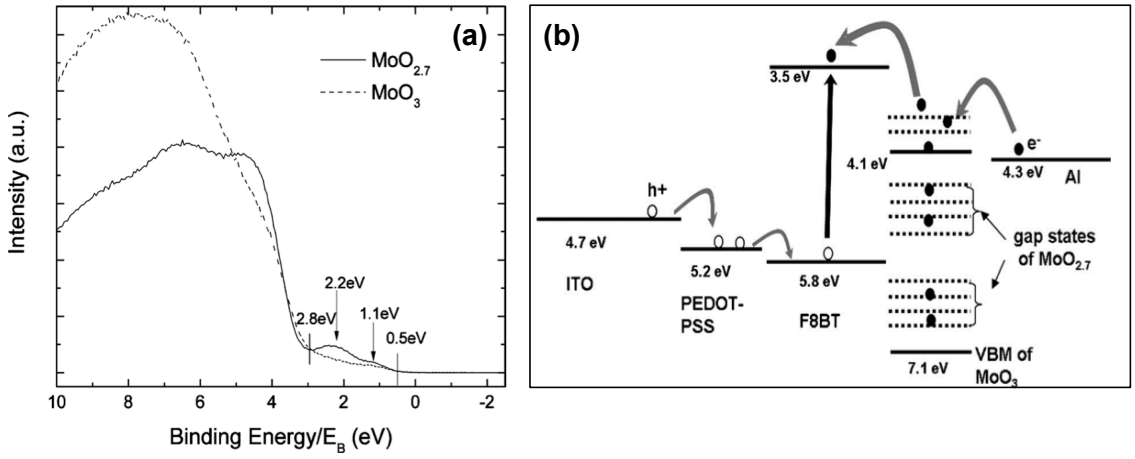

Figure 4.15: (a) UPS spectra of the MoO_3(dashed line) and the $MoO_{2.7}$(solid line) film on Al-coated Si-substrate. (b) Energy diagrams of MoO_3 and $MoO_{2.7}$ in an OLED architecture. (Image courtesy of Vasilopoulou[149])

4.3.1 Reduced Molybdenum Oxide

Formation of gap states above the valence band maximum occurs for oxygen-deficient MoO_{3-x}[145, 146], where x denotes the degree of reduction. There exist no gap states for a fully oxidized MoO_3 film. The gap states enhance the conductivity of MoO_3 and provide transition paths for carriers to assist in hole injection.[147].

Vasilopoulou et. al. recently reported an OLED performance study by comparing fully oxidized Molybdenum oxide, MoO_3 and partially reduced Molybdenum oxide, $MoO_{2.7}$. Figure 4.15(a) shows the low binding energy region of the UPS spectra of both MoO_3 and $MoO_{2.7}$. The main features appear at $\sim$4.5eV and $\sim$6.4eV below the Fermi level due to the orbital contributions from different oxygen species.[148] For $MoO_{2.7}$, two small peaks show up at $\sim$1.1eV and $\sim$2.2eV below the Fermi level. These gap states are due to the reduction of the Molybdenum atoms. The formation of oxygen vacancies leads to occupation of the Mo $4d$ orbitals with electrons, shown in the dotted lines in Figure 4.15(b).

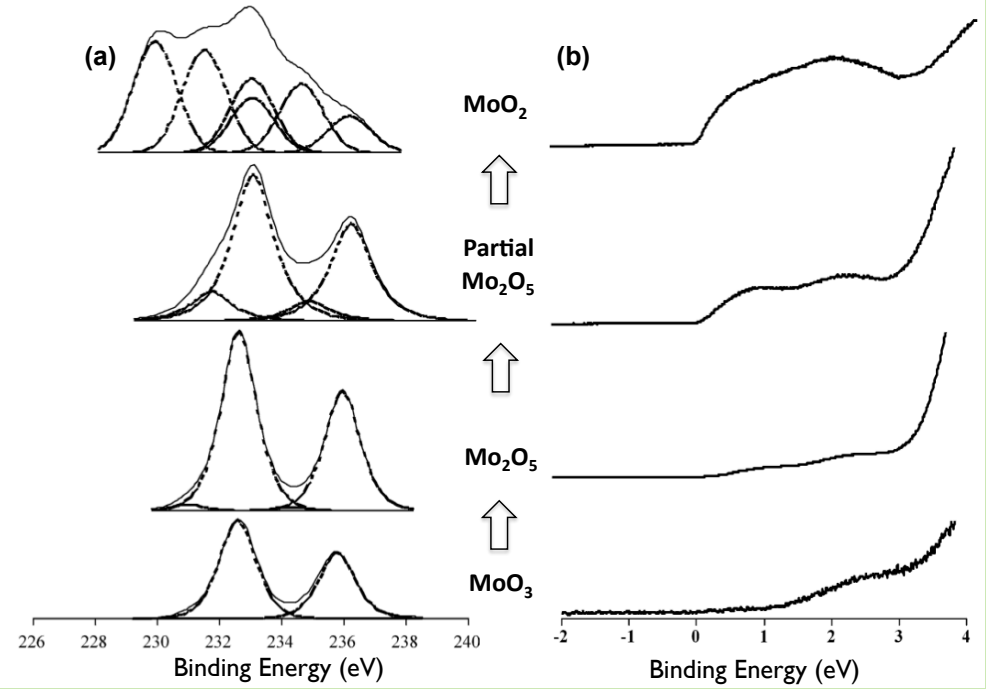

Figure 4.16: (a) The XPS spectra of the Mo 3*d* energy region of the *in situ* reduction by hydrogen of commercial bulk MoO_3 at consecutive temperatures (as received: MoO_3; 573K: Mo_2O_5; 623K: Partial Mo_2O_5; and 653K: MoO_2.) (b) The UPS of the σ and π bands of the corresponding *in situ* reduction. (Image courtesy of Al-Kandari[150])

4.3.2 Discussion

The MoO_3 of high purity (99.95%, metals basis) was purchased from Alfa Aesar. It is speculated that reduction might occur during deposition. Possible formation of Mo_2O_5 and MoO_2 could thus be possible. The use of UPS and XPS would provide valuable information in the characterization process.[150]. These XPS-UPS spectra of the reduction process of bulk MoO_3 are interpreted as follows:

$$MoO_3 \Rightarrow Mo_2O_5 \Rightarrow MoO_2.$$

Figure 4.16 shows the XPS spectra of the Mo (3d) energy region of the reduction at consecutive temperatures, with the corresponding UPS of the α and π bands of the in situ reduction. Since the reduction is sensitive to temperature and other in situ variables, the energy band data might vary from lab to lab. Therefore, a corresponding UPS and XPS study is necessary in order to have an systematic and in-depth understanding of the energy levels of MoO_3 during vacuum thermal deposition.

CHAPTER V

Thermal Management in High Intensity OLED Applications

In this chapter, we use a general transmission matrix formalism to determine the thermal response of OLEDs under high current normally encountered in ultra-bright illumination conditions. This approach, based on Laplace transforms, facilitates the calculation of transient coupled heat transfer in a multi-layer composite characteristic of OLEDs. Model calculations are compared with experimental data on 5cm×5cm green and red-emitting electrophosphorescent OLEDs (PHOLED) under various current drive conditions. This model can be extended to study other complex optoelectronic structures under a wide variety of conditions that include heat removal via conduction, radiation and convection. We apply the model to understand the effects of using high-thermal-conductivity substrates, and transient thermal response under pulsed-current operation.

This chapter is organized as follows: we start with the thermal problems associated with OLEDs, followed by introducing the transmission matrix approach along with some modifications that are specific for the PHOLED structure and thermal conditions described. The following section details the experimental methods used for the assessment of thermal power dissipation and the measurement of the transient temperature response. The comparison between model prediction and experimental

results are presented and analyzed. We also describe the application of these results to PHOLEDs to assess their potential for high intensity operation, including the use of substrates with a range of thermal conductivities, and under pulsed operation. We compare our results in this section with the more complex finite element method for solving complex differential equations, and find agreement between both approaches. Appendix B provides details of the calculation procedure.

5.1 An Overview on Thermal Problems

OLEDs have attracted attention due to their high efficiency, broad color gamut, ease of fabrication and mechanical flexibility when deposited on plastic or metal foil substrates.[17, 99] A particular challenge in achieving intense OLED sources for illumination or other applications is to efficiently remove heat that can accelerate degradation of the organic active materials under the high currents required.[151] This is a particular problem for large area devices where Joule heating can be substantial[152, 153], leading to a pronounced temperature rise during operation. An example of such heating is the electrophosphorescent stacked red-green-blue OLED that has been demonstrated as a high intensity white lighting source.[114] Under a current density of 40mA/cm^2 at an operating voltage of 10V, the optimized device demonstrates a luminance of $10{,}000\text{cd/m}^2$, corresponding to a PE of 12lm/W. This leads to a power dissipation of 4kW/m^2 that can result in a temperature rise in excess of 30^oC.

Since localized Joule heating degrades the efficiency, operational lifetime [154], and brightness homogeneity[155], it is important to quantitatively understand the thermal environment of the multilayer composite device under high current operation, and then to mitigate the effects of heating by optimized device and system design guided by this understanding. In this work, we calculate the thermal properties of OLEDs using an approach based on transmission matrix analysis that is generally applicable to complex, multilayer structures. Laplace transforms are used to determine the

response of the system to the combined effects of thermal radiation, conduction and convection, while also taking account of non-dissipative energy loss through OLED light emission. Our approach is an extension of the heat-transfer method introduced by Pipes[156] used to analyze heat flow across insulating walls, but in our approach we include (i) parallel and series pathways required for accurate consideration of losses by the combined processes of thermal convection, conduction, and radiation; (ii) thermal generation within the layers themselves; (iii) losses through light emission; (iv) heat flow across interfaces with finite thermal resistances between layers; and (v) response to a thermal impulse. This complex set of conditions is common in many multilayer optoelectronic devices.

The calculated results are found to accurately compare with thermal measurements for OLEDs obtained using time-resolved infrared imaging under various operating conditions. The model predictions agree with experimental data for two sets of PHOLEDs, one emitting in green and the other in red.

5.2 Main Channels for Thermal Dissipation

There are four main channels that a display could dissipate power: light, conduction, convection, and radiation. A free convection flow field is a self-sustained flow driven by the presence of a temperature gradient, as opposed to a forced convection flow where external means are used to provide the flow. As a result of the temperature difference, the density field is non-uniform. Buoyancy will induce a flow current due to the gravitational field and the variation in the density field. In general, free convection heat transfer is usually much smaller compared to forced convection heat transfer. It is therefore important only when there is no external flow. The transfer of heat from flat plates by free convection has long been studied under the condition that the flat plate is at a uniform temperature. Conventionally, a dimensionless quantity, the Rayleigh number is defined as

$$R_a = G_r P_r, \text{ where} \tag{5.1a}$$

$$G_r = g\beta\rho^2 L_c^3 \Delta T/\mu^2, \text{ and} \tag{5.1b}$$

$$P_r = \mu c_p/k_a \tag{5.1c}$$

where the Rayleigh number, R_a is defined as the product of two other dimensionless quantities, the Prandtl number, P_r, and the Grashof number, G_r, β is the thermal expansion coefficient, ρ is the density, μ is the viscosity, c_p is the heat capacity, k_a is the thermal conductivity, g is the gravitational constant, and L_c is the critical dimension of the display. The most important use of the Rayleigh number is to characterize the laminar to turbulence transition of a free convection boundary layer flow. For example, when $R_a \geq 10^9$, the vertical free convection boundary layer flow over a flat plate becomes turbulent.

The net thermal radiation from a surface depends on the temperature and emissivity of the surface as well as the ambient temperature. The net power dissipation per unit area due to radiation is:

$$Q_{rad} = \sigma\epsilon(T_m^4 - T_0^4) = \sigma\epsilon((T_0 + \Delta T)^4 - T_0^4) \approx 4\sigma\epsilon T_0^3 \Delta T \equiv h_{rad}\Delta T \tag{5.2}$$

where T_m is the display temperature, T_0 is the ambient temperature, ΔT is the rise in the display temperature above that of the ambient, σ is the Stefan-Boltzmann constant, and ϵ is the emissivity of the display surface. For the relatively small temperature rises (typically less that 40K) in this thesis, this may be approximated to be linear with ΔT with the heat transfer coefficient for radiation $h_r \equiv 4\sigma\epsilon T_0^3$.

5.3 Matrix Modeling

5.3.1 Laplace Transform

When a thin film with uniform thickness is subjected to an input heat flux, Q, incident on one surface, the one dimensional law of heat conduction, also known as Fouriers law, states that the heat flux is proportional to the negative of the local temperature gradient:

$$-\frac{\partial T(x,t)}{\partial x} = \frac{1}{K}Q(x,t) \tag{5.3}$$

where $T(x,t)$ is the temperature of the thin film at point x at time t, $Q(x,t)$ is the heat flux, and K is the thermal conductivity of the thin film. The continuity equation states that the heat flux at point x raises the temperature following:

$$-\frac{\partial Q(x,t)}{\partial x} = C\frac{\partial T(x,t)}{\partial t} \tag{5.4}$$

where $C = c_v\rho$ is the volumetric heat capacity, a product of specific heat at constant volume, c_v, and density, ρ. This equation expresses the conservation of heat in an infinitesimal thin film volume. Equations 5.3 and 5.4 are combined to yield:

$$\frac{\partial T(x,t)}{\partial t} - \alpha\frac{\partial^2 T(x,t)}{\partial^2 x} = 0 \tag{5.5}$$

where $\alpha = K/c_v\rho$ is the heat diffusivity of the material. Internal heat generation is not included, and the solution is subject to the boundary conditions of both heat and temperature incident at the material surface.

Now we take the Laplace transform for $T(x,t)$, and $Q(x,t)$, respectively:

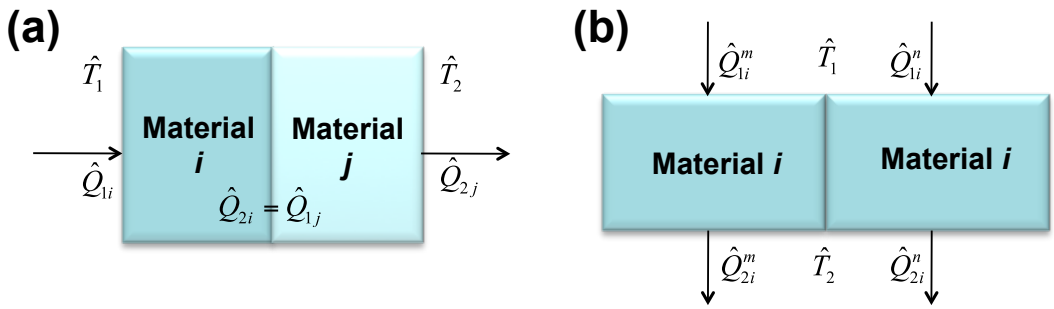

Figure 5.1: (a) Heat flow for layers in series. Here T_1 and T_2 denote the Laplace transformation of ambient temperatures on both sides of the composite. $\hat{Q}_{1i}/\hat{Q}_{2i}$, and $\hat{Q}_{1j}/\hat{Q}_{2j}$are the heat inflow/outflow of material i, and j, respectively. Here $\hat{Q}_{2i} = /\hat{Q}_{1j}$ is based on the continuity of the interface heat flux between adjacent layers. (b) Heat flow for layers in parallel, where $\hat{Q}^m_{1i}$ and $\hat{Q}^n_{1i}$ denote inflow heat flux carried by two thermal dissipation modes, and $\hat{Q}^m_{1i} + \hat{Q}^n_{1i}$ heat flux into material i.

$$\hat{T}(x,s) \equiv \mathcal{L}T(x,t) = \int_0^\infty e^{-st}T(x,t)dt \tag{5.6a}$$

$$\hat{Q}(x,s) \equiv \mathcal{L}Q(x,t) = \int_0^\infty e^{-st}Q(x,t)dt \tag{5.6b}$$

where $\mathcal{L}$ denotes the Laplace transform, s is the Laplace variable, $\hat{T}(x,s)$ and $\hat{Q}(x,s)$ are the Laplace transforms of the temperature and heat flux, which can be used to simplify the solutions to Equations 5.3 and 5.4:

$$-\frac{\partial \hat{T}(x,s)}{\partial x} = \frac{1}{K}\hat{Q}(x,s) \tag{5.7a}$$

$$-\frac{\partial \hat{Q}(x,s)}{\partial x} = sC\hat{T}(x,s) \tag{5.7b}$$

Pipes has shown that this system of equations has solutions expressed as follows:[156]

$$\begin{bmatrix} \hat{T}_1 \\ \hat{Q}_1 \end{bmatrix} = \begin{bmatrix} cosh(\theta_i) & Z_0 sinh(\theta_i) \\ \frac{sinh(\theta_i)}{Z_0} & cosh(\theta_i) \end{bmatrix} \cdot \begin{bmatrix} \hat{T}_2 \\ \hat{Q}_2 \end{bmatrix} = \begin{bmatrix} A_i & B_i \\ C_i & D_i \end{bmatrix} \cdot \begin{bmatrix} \hat{T}_2 \\ \hat{Q}_2 \end{bmatrix} = \begin{bmatrix} T(\theta_i) \end{bmatrix} \cdot \begin{bmatrix} \hat{T}_2 \\ \hat{Q}_2 \end{bmatrix} \tag{5.8}$$

where $\hat{T}_i(x,s)$, and $\hat{Q}_i(x,s)$ (i=1,2) are the Laplace transforms of the temperature and heat flux on two sides of the layer of interest, i (1 is for the heat flux input side, and 2 the output side), $\theta_i = L_i\sqrt{C_i s/K_i}$ is the operational propagation coefficient characterized by K_i, C_i, and L_i (the thickness of the ith material layer), $Z_i = \sqrt{1/(K_i C_i s)}$ is the operational characteristic impedance of the layer, and A_i, B_i, C_i, and D_i (D_i=A_i) denote the matrix elements.

Equation 5.8 represents a general approach to solve the transient thermal conduction problem for a multi-layer composite subject to certain boundary conditions, as described by either the temperature or the heat flux at a given surface or interface (denoted as $\hat{T}_1(x,s)$, $\hat{T}_2(x,s)$, $\hat{Q}_1(x,s)$, and $\hat{Q}_2(x,s)$). Since both the interface temperature and heat flux between adjacent layers are continuous, the entire composite can be described as the product of matrices in series:

$$\begin{bmatrix} T(\theta) \end{bmatrix} = \begin{bmatrix} T(\theta_1) \end{bmatrix} \begin{bmatrix} T(\theta_2) \end{bmatrix} \cdots \begin{bmatrix} T(\theta_n) \end{bmatrix} \tag{5.9}$$

where $\begin{bmatrix} T(\theta) \end{bmatrix}$ is the over-all transmission matrix of the entire composite, and $\begin{bmatrix} T(\theta_i) \end{bmatrix}$ is the transmission matrix of the ith layer. An example representation of a two-layer composite, with layers denoted as i, and j, is given in Figure 5.1(a). Note that we treat the term, internal heat generation, as boundary condition to simplify the calculation.

To account for interface resistances to the thermal flux between layers, we consider the interface to be a thin layer with negligible specific heat. That is, letting C_i=0

in 5.8, we include interface effects with the reduced transmission matrix.

$$\left[T(\theta)\right] = \begin{bmatrix} 1 & R_{int} \\ 0 & 1 \end{bmatrix} \tag{5.10}$$

where R_{int} is the total (empirical) thermal resistance (m^2K/W) of the interface.

The method can be further modified to incorporate radiation by introducing a parallel matrix describing power losses that additively combine, such as radiation and conduction. The parallel heat dissipation pathway is shown schematically in Figure 5.1(b), where $\hat{Q}^m_{1i}(x,s)$ and $\hat{Q}^n_{1i}(x,s)$ ($\hat{Q}^m_{2i}(x,s)$ and $\hat{Q}^n_{2i}(x,s)$) denote heat flux input (output) carried along two independent thermal dissipation pathways labeled, m and n. In this case, m and n correspond to thermal conduction and radiation, respectively. Once agin, following Pipes[156], we therefore take into account of both modes on a single layer of interest, i. Here $\hat{Q}^m_{1i} + \hat{Q}^n_{1i}$ is the Laplace transform of total heat flux into i. Then, Equation 5.8 can be rearranged as:

$$\begin{bmatrix} \hat{Q}^k_{1i} \\ \hat{Q}^k_{2i} \end{bmatrix} = \begin{bmatrix} A^k_i/B^k_i & -1/B^k_i \\ 1/B^k_i & -A^k_i/B^k_i \end{bmatrix} \cdot \begin{bmatrix} \hat{T}_1 \\ \hat{T}_2 \end{bmatrix} \tag{5.11a}$$

$$\begin{bmatrix} Q_{1i} \\ Q_{2i} \end{bmatrix} = \sum_{k=m,n} \begin{bmatrix} Q^k_{1i} \\ Q^k_{2i} \end{bmatrix} = \sum_{k=m,n} \begin{bmatrix} A^k_i/B^k_i & -1/B^k_i \\ 1/B^k_i & -A^k_i/B^k_i \end{bmatrix} \cdot \begin{bmatrix} \hat{T}_1 \\ \hat{T}_2 \end{bmatrix} \tag{5.11b}$$

where $k = m$ or n. Here, we assume the heat flux along the boundary plane between layers is negligible compared to the heat flux normal to layers.

5.3.2 Transmission Matrix Procedure

In a typical OLED, the heat source is assumed to be the EML combined with the HTL, the ETL and the exciton blocking layer (EBL), embedded inside of the multi-layer composite. That is, we need to consider the case where the layers themselves act

as heat sources, rather than perform simply as heat-transfer media. Since the thermal properties of these various organic thin films are often similar, for simplicity and without loss of generality, we assume only a single organic layer characterized by the average thermal constants of all such layers comprising the OLED active region. As shown in Figure 5.2(a), we characterize this feature by analyzing two sub-matrices, $M^L(\theta)$ and $M^R(\theta)$, one to the left and the other to the right of the heat source, respectively. We then separate the heat flux input into two parts, $Q^L_{src}(\theta)$ and $Q^R_{src}(\theta)$, following the boundary condition:

$$Q^L_{src}(\theta) + Q^R_{src}(\theta) = Q_{therm} = JV - Q_{opt} \tag{5.12}$$

where $Q^L_{src}(\theta)$ and $Q^R_{src}(\theta)$ are the heat fluxes input to the left and right matrices, respectively, Q_{therm} is the thermal power generation of the device, J and V are the current density and voltage required for device operation, and Q_{opt} is the power removed in the form of light. Thus Equation 5.8 becomes:

$$\begin{bmatrix} \hat{T}_{src} \\ \hat{Q}^{L,R}_{src} \end{bmatrix} = \begin{bmatrix} M^{L,R}(\theta) \end{bmatrix} \begin{bmatrix} \hat{T}_{src} \\ \hat{Q}^{L,R}_{src} \end{bmatrix} \tag{5.13}$$

where $\hat{T}_{src}$ and $\hat{T}_0$ are Laplace transform of the source and ambient temperature, respectively, $\hat{Q}^L_{src}$ and $\hat{Q}^R_{src}$ are Laplace transforms of heat flux dissipated through $M^L(\theta)$ and $M^R(\theta)$, respectively. In this study, $M^L(\theta)$ is composed of the conduction matrices for the ITO anode, glass substrate, and air in sequence, and $M^R(\theta)$ is composed of the thermal conduction matrices for a single composite organic layer, Al cathode, and air in sequence, as shown in Figure 5.2(b). For devices with encapsulation, the matrices for air gap $\left[T(\theta_{AirGap})\right]$ and glass cap $\left[T(\theta_{EnCap})\right]$have to be included in the sequence.

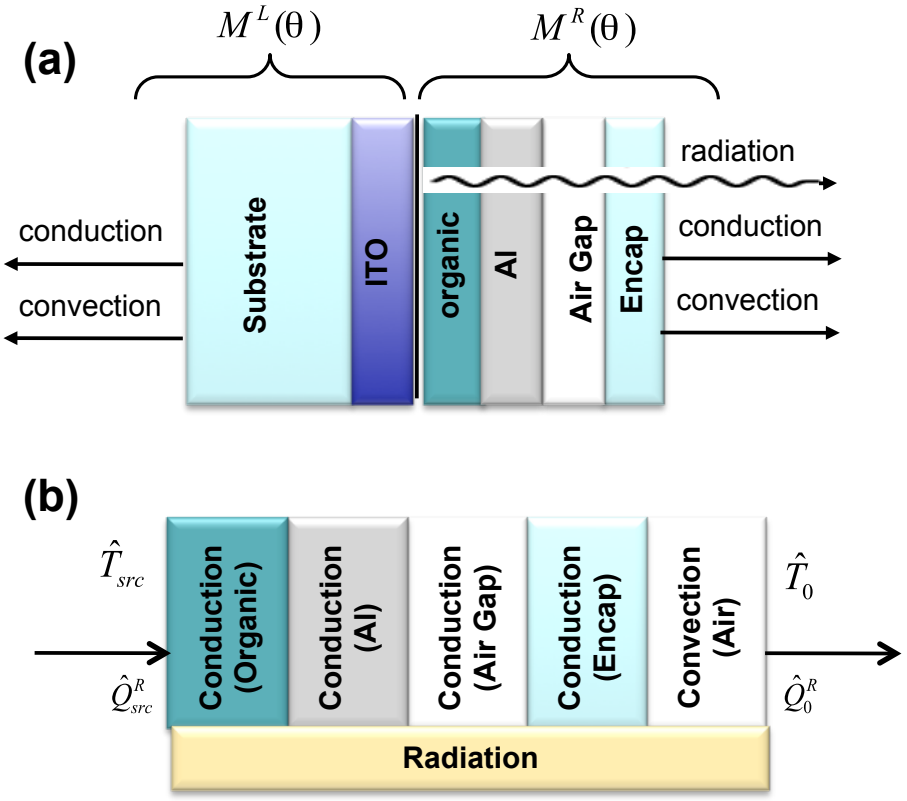

Figure 5.2: Matrix construction for OLED operation where heat source is in-between the layers. Displayed here are two sub-matrices, $M^L(\theta)$, and $M^R(\theta)$, the matrix to the left and right of the heat source, respectively, where $M^L(\theta)$ is composed of air, glass substrate, and ITO anode in sequence, and $M^R(\theta)$ is composed of organic layer, Al cathode and air in sequence. (b) The construction of $M^R(\theta)$, where $\hat{T}_{src}$ and $\hat{T}_0$ are source and ambient temperature, respectively, $\hat{Q}^L_{src}$ and $\hat{Q}^R_{src}$ are heat flux dissipated through the left and right matrices, and $\hat{Q}^L_{src} + \hat{Q}^L_{src}$=Laplace transform of total thermal power. There conduction matrices for organic, Al cathode and air are multiplied in sequence while radiation is incorporated as perturbation.

For radiation perturbation approximation, we use the Stefan-Boltzmann Law:

$$Q = \sigma\epsilon(T_{src}^4 - T_0^4) = \sigma\epsilon(T_{src}^2 + T_0^2)(T_{src} + T_0)(T_{src} - T_0) \simeq h_{rad}(T_{src} - T_0) \quad (5.14)$$

where the last term on the right is an approximation for $T_{src} \simeq T_0$=300K, the ambient tempearture. Here ϵ is the emissivity of the grey body(assumed to equal 0.5 for this study[152]), and σ is the Stefan-Boltzmann constant. Now h_{rad} $\simeq$5W/m^{2}K for an estimated 20^{o}C temperature rise. This linear radiation approximation is treated as a parallel matrix following Equation 5.10:

$$\left[T(\theta)\right] = \begin{bmatrix} 1 & R_{rad} \\ 0 & 1 \end{bmatrix} \quad (5.15)$$

where $R_{rad} = 1/h_{rad}$ is the thermal resistance of radiation. Combing Equation 5.8 and 5.15 into 5.11b, we obtain the total matrix, $M^R(\theta)$ that takes into account conduction, convection, and radiation:

$$\left[M^R(\theta)\right] = \begin{bmatrix} A^R & B^R(1-\gamma_{rad}) \\ C^R(1+\gamma_{rad}) & A^R \end{bmatrix} \quad (5.16)$$

where $\gamma_{rad} = B^R/R_{rad} \ll 1$ is the radiation perturbation term, and A^R, B^R, and C^R are elements of 2×2 matrices: $\left[T(\theta_{Org})\right]\left[T(\theta_{Al})\right]\left[T(\theta_{AirCap})\right]\left[T(\theta_{EnCap})\right]\left[T(\theta_{Air})\right]$. The left matrix, $M^L(\theta)$, can be similarly constructed. Convection in this case is treated analogously to conduction, where an effective conductance, K_{conv}, is used to characterize the heat removal at the boundary between the OLED surface and the ambient. Here, K_{conv} depends on the ambient conditions, varying significantly between cases such as stagnant or forced-air cooling.

5.4 Results and Discussion

5.4.1 Experimental

We studied two sets of PHOLEDs of different sizes: 1 mm×1 mm unencapsulated $Ir(ppy)_3$ devices on 1 cm×1 cm substrates, and 5cm×5cm large-area encapsulated devices (provided by Universal Display Corp., Ewing, NJ). The small devices were used to investigate two dimensional (2D) head spreading, whereas the larger devices allowed for direct comparison of experiment to our 1D model. Note that for lighting applications, devices are expected to be large (i.e. they occupy a significant fraction of the substrate area), and hence the 1D approach is more suitable, whereas small devices approximate point heat sources in such applications as intense light emitters (e.g. lasers).

The $1mm^2$ devices were prepared as follows. The 20Ω/sq pre-patterned (in 1mm stripes) ITO-coated glass substrates were degreased in detergent solution, followed by thorough rinsing in de-ionized water. The substrates were then boiled in trichloroethane, and rinsed in acetone in an ultrasonic tank, boiled in isopropanol, and dried in pure nitrogen gas. Next, the substrates were exposed to UV/ozone for 10 min prior to transfer into a high vacuum ($\sim 10^{-7}$ Torr) deposition chamber. A 40-nm-thick HTL of NPD was used as the hole transport layer, followed by a 25nm-thick $Ir(ppy)_3$ or PQIr doped at 8wt% in a 25nm-thick CBP host as the phosphorescent emission layer, a 40nm-thick BCP as the combined ETL and EBL followed by a 10nm-thick Li doped BCP in a 1:1 molar ratio, and finally capped by a 100-nm-thick Al cathode. Undoped BCP was used to prevent Li diffusion into the EML and to maintain the charge balance at a high bias. The 1 mm^2 device structure and the electrode patterning design are shown in Figure 5.3.

The large-area green and red PHOLEDs emit at peak wavelengths of λ=530nm and 630 nm, respectively. The structure of these two packaged devices is as fol-

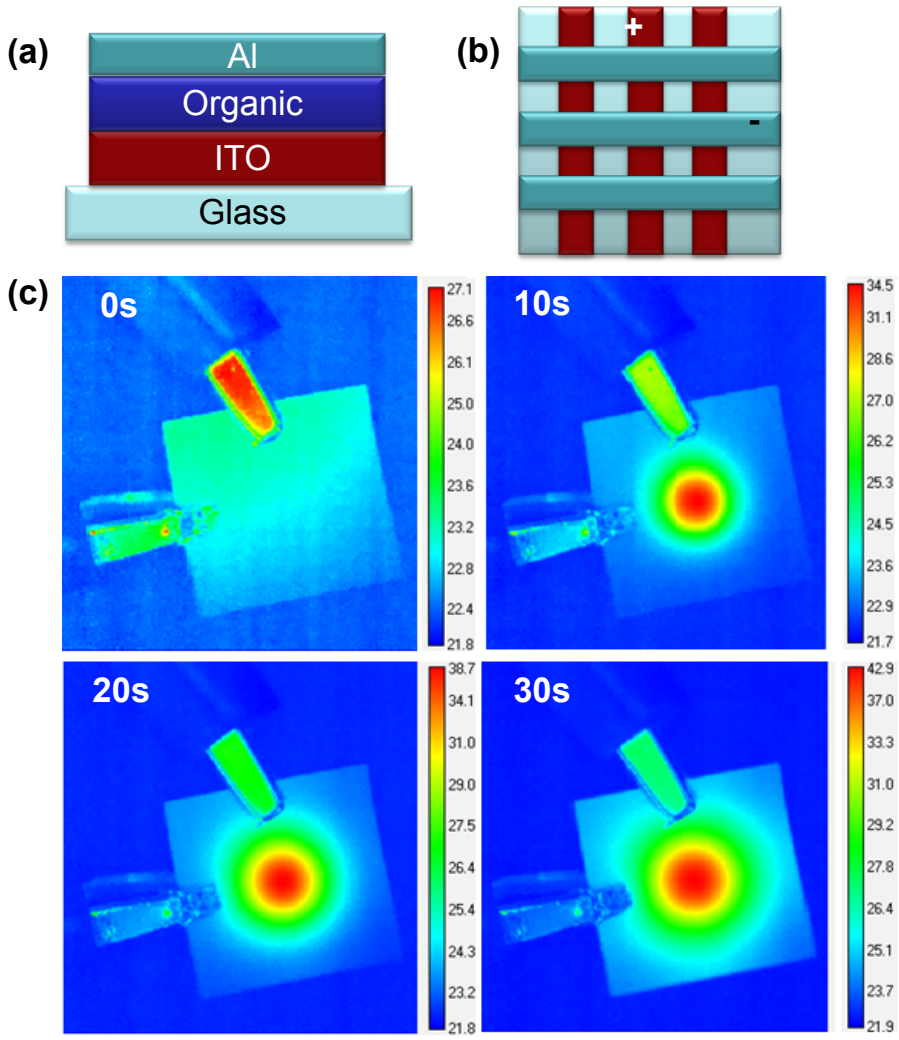

Figure 5.3: Device structure of small-area $Ir(ppy)_3$ devices: glass (1mm)/ITO (120nm)/organic layers (105nm)/Al cathode (100nm). (b) Patterning of ITO and Al stripes, each 1mm in width. (c) The thermal images of the $Ir(ppy)_3$ device under a fixed voltage of 10V (or a current density of $1A/cm^2$) after 10, 20, and 30s operation following the onset of the voltage ramp.

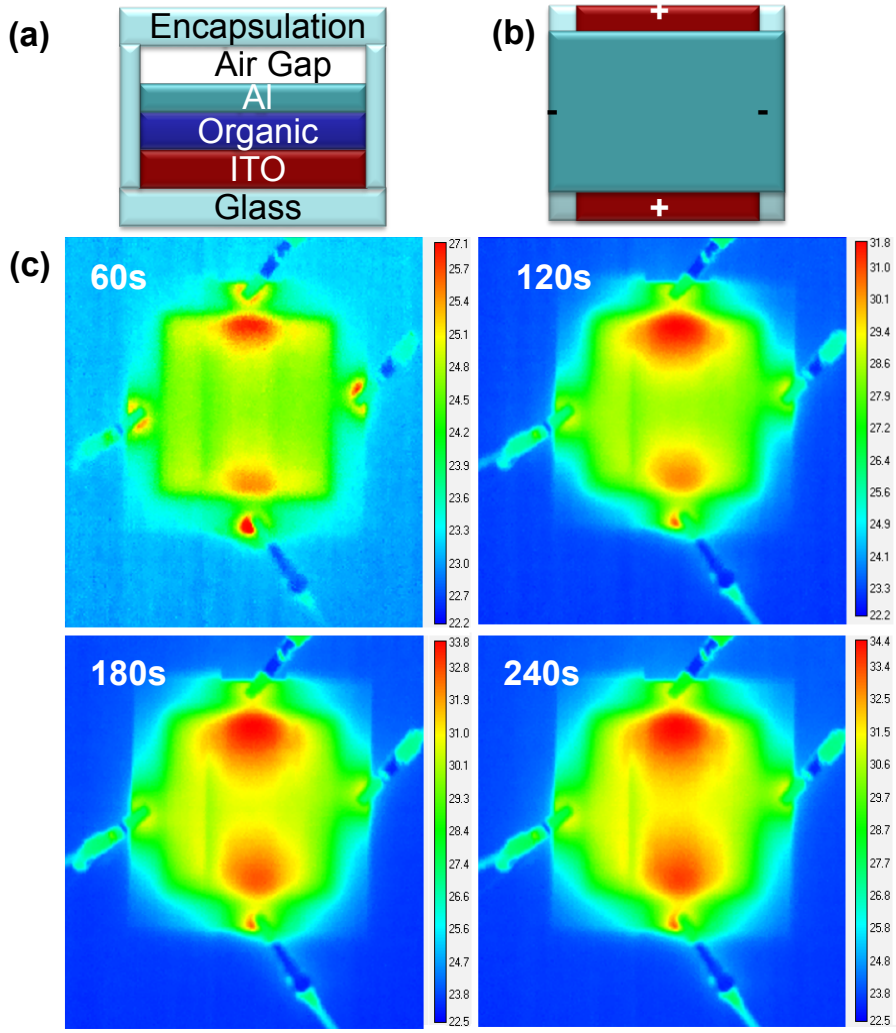

Figure 5.4: Device structure of large-area devices: glass (0.7mm)/ indium tin oxide (ITO) (120nm)/organic layers (120nm)/Al cathode (100nm)/Air gap (30μm)/Glass encapsulation (0.7mm). (b) Patterning of ITO and Al, both are 5cm in width. (c) The thermal images of large-area green device under a fixed voltage of 7V (or a current density of 3.4mA/cm^2) after 60, 120, 180, and 240s operation following the onset of the voltage ramp.

lows: glass (0.7mm)/ITO (120nm)/organic layers (120nm)/Al cathode (100nm)/air gap (30μm)/glass encapsulation (0.7mm) (see Figure 5.4a). Encapsulation prevents degradation of the devices due to contact with air or moisture over the extended testing sequence. Figure 5.4(b) shows the 5cm×5cm ITO and Al patterns on the glass substrate. It is important to provide uniform current injection to achieve homogeneous emission across the entire device area. The sheet resistivity of the ITO anode (20Ω/sq) is considerably greater than that of the Al cathode (0.3Ω/sq for 100nm-thick Al)[157][158], making uniform current injection from the anode particularly challenging. Hence, both the anode and cathode are pumped from two opposing contacts, as shown in Figure 5.4(b). Here, hole injection is via the top and bottom contacts in the figure, and electron injection is from the left and right contact pads.

The J-V characteristics of the completed devices were measured using a semiconductor parameter analyzer (HP 4145B). Optical characterization of the devices employed a calibrated reference detector using standard methods.[135] The fraction of the total input power removed through non-dissipative optical emission (Q_{opt}) was calculated based on output spectra and luminance at a fixed current density, i.e. $Q_{opt} = 1.7[I_{ph}/R_{\lambda}A]$. Here I_{ph} is the detector photocurrent corresponding to light output in the forward-viewing direction, R_{λ} is its wavelength-weighted-average responsivity over the PHOLED spectrum, and A is the PHOLED emitting area. The factor 1.7 adjusts for light emitted in all directions, including waveguide and glass-mode emission.[159] Thermal imaging measurements were acquired using a non-contact thermal camera (FLIR A325). To eliminate stray light and to provide a thermally stable environment where images were taken, samples were inserted into a box with a light absorbing black interior. The PHOLED current was provided via a Keithley 2400 source meter.

The transient temperature data for each sample were obtained by tracking their thermal images under various current densities. For this purpose, the frame rate of the

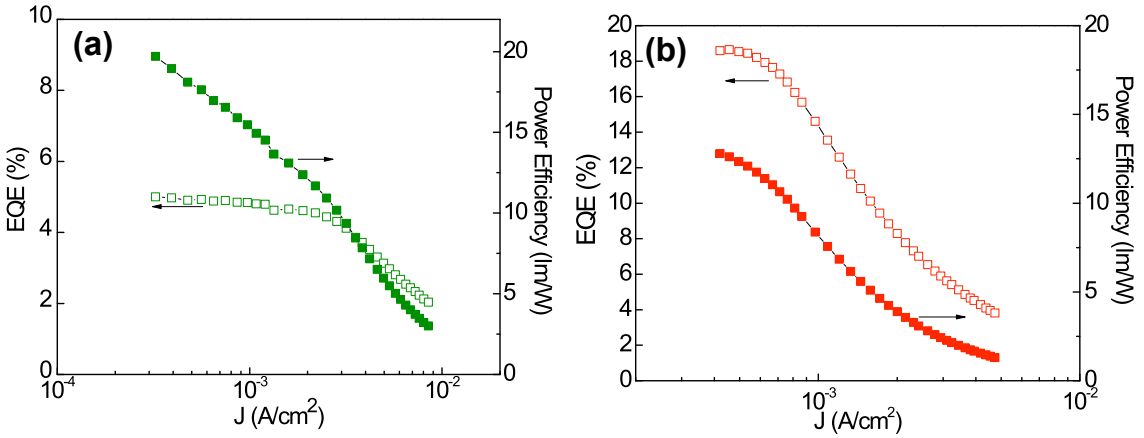

Figure 5.5: The EQE and PE for large-area green OLED. (b) The EQE and PE for large-area red OLED.

thermal imaging system was 60Hz, adequate for the purposes of these experiments. Two sets of data were recorded: device heat-up, and cool-down. To capture the transient temperature rise, devices were operated under constant voltage for 5 min until equilibrium was reached, with their thermal images captured at a frame rate of $2s^{-1}$. To observe the cool-off dynamics, the devices were turned off after reaching equilibrium at a fixed V, and the temperature transient was similarly obtained until room temperature was reached.

5.4.2 Results

Figure 5.3(c) shows the transient thermal images of the 1mm^2 Ir(ppy)$_3$ device after 10, 20, and 30s following the onset of a 10V step (corresponding to J=1A/cm^2). While the thermal distribution is localized around the light-emitting area, it is observed to spread out from the active device region. The temperature difference between the center of the device and the substrate edges after 60 s when equilibrium is established following the onset of the current step is 21^{o}C.

To model the relation of temperature vs. thermal flux using our one dimensional model, a uniformly distributed, well-defined temperature profile is needed. For this

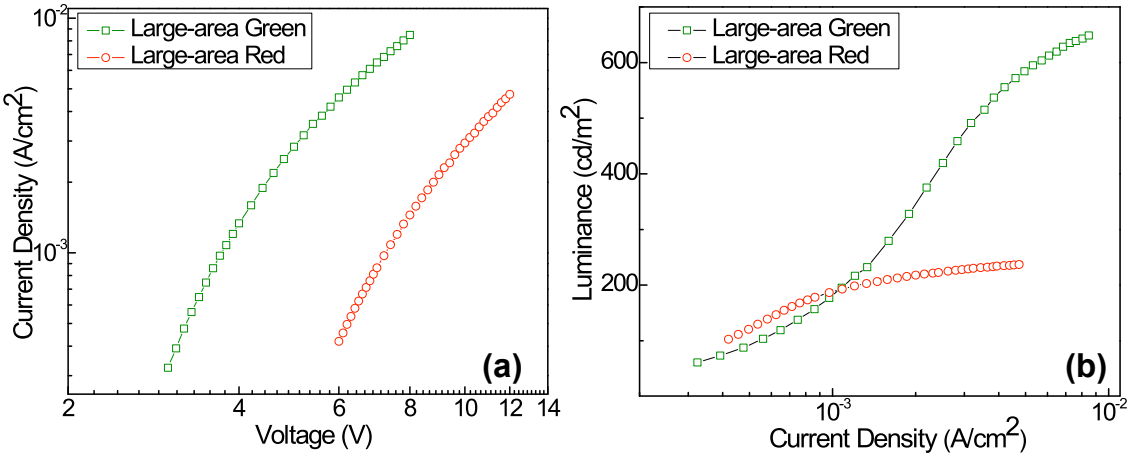

Figure 5.6: The (a)J-V and (b) L-V characteristics of large-area green and red OLEDs.

purpose we, therefore, use the large-area devices. Figure 5.4(c) shows the transient thermal images of the large-area green device at 7V (corresponding to J=9 mA/cm^2) after 60, 120, 180, and 240s following the onset of the voltage step. There is a pronounced temperature variation across the device area, with higher temperatures close to the anode contacts near the device edge. This results from the high ITO resistivity that provides less current near the device center than at its edges. The temperature variation across the surface is within 1.8 C when the devices are operated at 5.5V$\leq$V$\leq$7.0V, corresponding to a surface temperature from 24^{o}C to 36^{o}C. The temperatures reported in subsequent data are the median, thereby ignoring minor device thermal gradients.

Table 5.1: Summary of efficiency and thermal performance of large-area green device.

$Voltage$ (V)	$CurrentDensity$ (mA/cm^2)	Q_{tot} (W/m^2)	Q_{opt} (W/m^2)	Q_{therm} /Q_{tot}
5.5	3.69	203	6	97%
6.0	4.60	276	6	98%
6.5	5.52	359	6	98%
7.0	6.48	454	7	98%

The EQE and PE for large-area green and red emitting PHOLEDs are shown in

Figure 5.5. The corresponding J-V characteristics are shown in Figure 5.6, along withe the luminance-voltage (L-V) characteristics. The estimated thermal generations under each operating conditions are summarized for the large-area green device in Table 5.1) and the red device in Table 5.2).

Table 5.2: Summary of efficiency and thermal performance of large-area red device.

V(V)	J (mA/cm^2)	Q$_{tot}$ (W/m^2)	Q$_{opt}$ (W/m^2)	Q$_{therm}$ /Q$_{tot}$
9.0	2.15	194	6	97%
10.0	2.94	294	6	98%
11.0	3.81	419	6	99%
12.0	4.74	569	6	99%

Note that the total input power is $Q_{tot} = J \cdot V$. The thermal power dissipation is then given by $Q_{therm} = Q_{tot} - Q_{opt}$. For the green device at a luminance of between 540cd/m^2 and 620cd/m^2 and the analogous red device at a luminance of between 220cd/m^2 and 240cd/m^2, approximately 97% to 99% of the total power is dissipated through the several thermal channels including conduction, convection and radiation(see calculated values based on measured device efficiencies for Q_{therm}/Q_{tot} listed in Tables 5.1 and 5.2).

Figures 5.7 shows the device temperature under varied input voltages, V, for large-area green and red OLED following the onset of the voltage step (symbols). These results are compared with transmission matrix model calculations indicated by solid lines. For the green device (Figures 5.7(a)), temperature were obtained (in symbols) under constant voltage of 5.5V, 6.0V, 6.5V, and 7.0V, corresponding to Q_{therm}=197, 270, 353, and 447W/m^2, respectively. The data for red device is similarly shown in Figures 5.7(b) under the voltage of 9.0V, 10.0V, 11.0V, and 12.0V, corresponding to Q_{therm}=188, 288, 413, and 563W/m^2, respectively.

To compare the temperature of the heat-generating layer (i.e. the EML, at temperature, T_{src}) to the device surface temperature (corresponding to the calculations

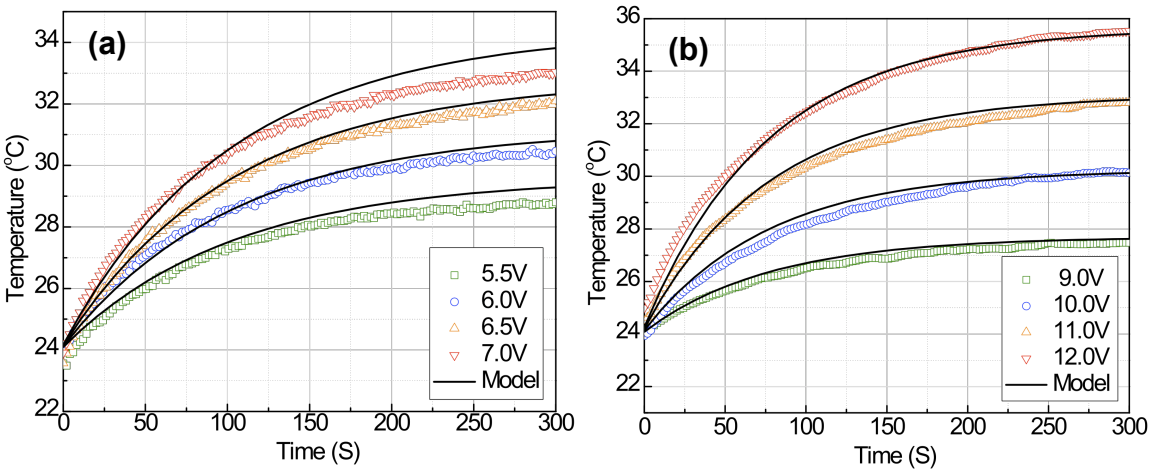

Figure 5.7: Surface temperature (open dots) under varied input voltages for large-area (a) green and (b) red OLED following the onset of the voltage ramp. Results are compared with transmission matrix model calculations (solid lines).

and measurements in Figure 5.7, respectively), we must calculate the thermal gradient across the device. The resulting gradient obtained using Equation 5.3 is shown in Figure 5.8 for the ITO and glass substrate, assuming thermal fluxes $Q_1 = 197$, $Q_2 = 270$, $Q_3 = 353$, and $Q_4 = 447 W/m^2$ for the green device under the same operation conditions as in Figure 5.7 and Table 5.1. For all power densities considered, a temperature difference of approximately 0.1^oC is observed between the source layer and the glass surface. This corresponds to 0.3% difference with the measured surface temperature of 30^oC, thereby contributing negligible error to fits in Figure 5.7. Note that the thermal gradient from EML to the top package surface is expected to be considerably larger due to the presence of the metal cathode, air gap, and glass encapsulation layer (c. f. Figure 5.2).

Figures 5.9 shows the device surface temperature under various voltages following the end of the voltage pulse (data points), in which case the device cools to the ambient temperature of $T \simeq 25^oC$. As in Figures 5.7, results are similarly compared with transmission matrix model calculations (solid lines).

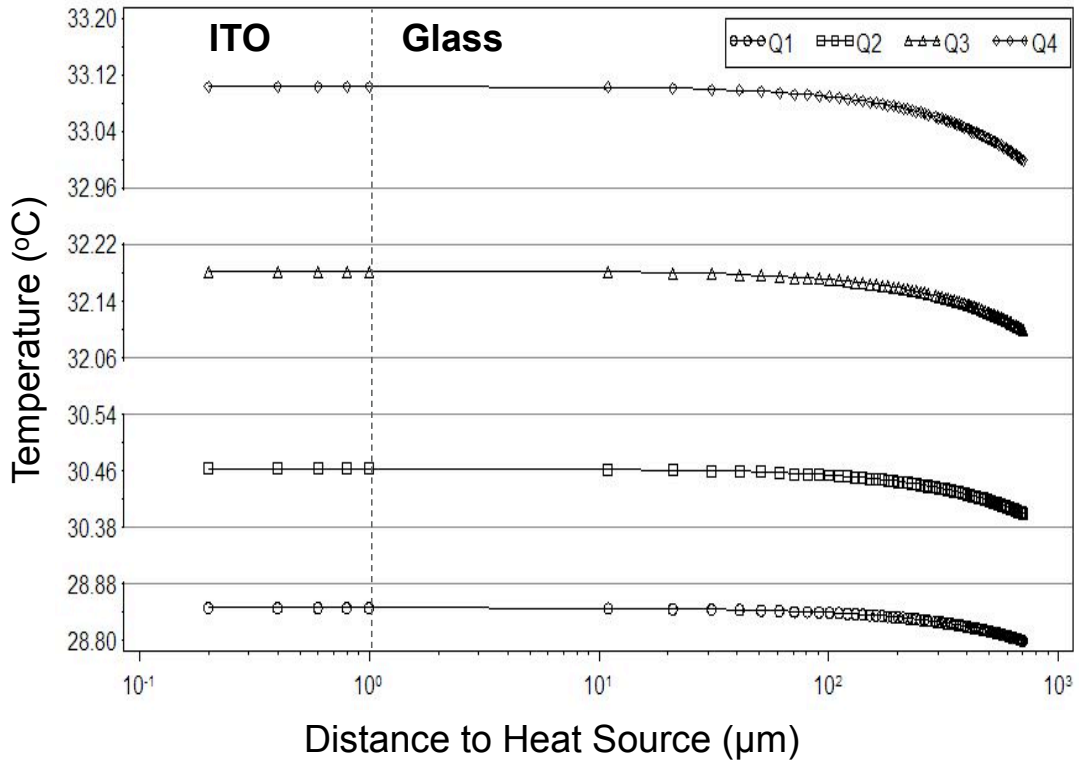

Figure 5.8: Calculated temperature gradient across the ITO and glass layers for heat fluxes of $Q_1 = 197$, $Q_2 = 270$, $Q_3 = 353$, and $Q_4 = 447 W/m^2$ generated in the PHOLED light emitting layer (EML). The surface temperatures at each heat flux is obtained from measurements using infrared imaging. The small thermal gradient suggests that the thermal measurements made at the glass surface are an accurate determination of the temperature of the EML.

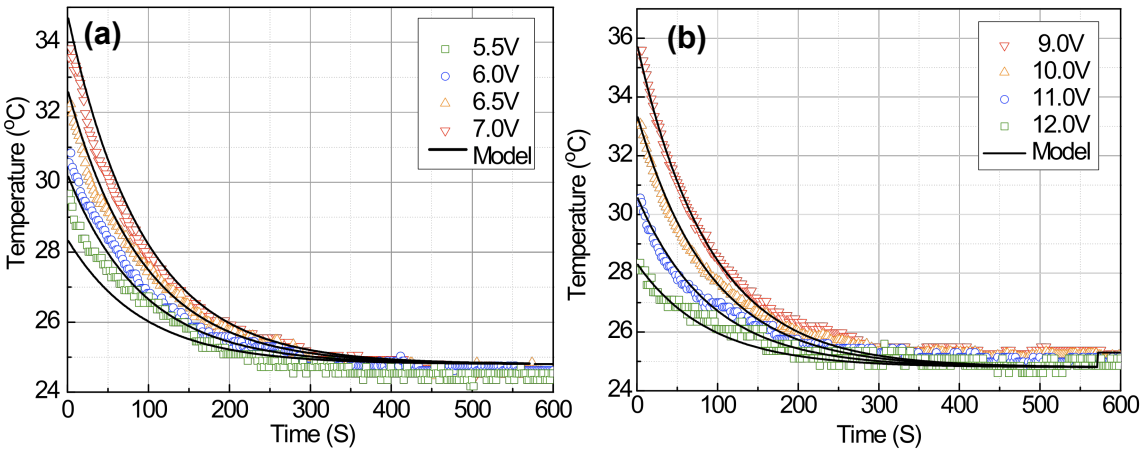

Figure 5.9: Surface temperature (open dots) under varied input voltages for large-area (a) green and (b) red OLED upon device cooling-off. Devices were operated under a fixed voltage until temperature equilibriums were reached. The point t=0 corresponds to the moment when the devices were turned off. Results are compared with transmission matrix model calculations (solid lines).

5.4.3 Discussion

One thing that needs to be tested is the validity of the calculations for matrices in series. This is important especially for the wide range of parameters (thickness, conductivity, etc.) employed in the OLED structure. Figure 5.10 shows the temperature transient under a constant thermal flux of Q_{therm}=1kW/m^2 for the distinct thicknesses of 200nm (organic films) and 2mm (glass substrate), and thermal conductivities of 0.26W/Km (organic films) and 3.0W/Km (glass substrate). For each parameter set, the plots provide calculated data for 1-layer, as well as 2- and 3-layer composites. The total thicknesses of the multi-layer composites are fixed to be the same as the 1-layer structure, *i.e.* 2mm for glass (Figure 5.10(a)) and 2μm for organic layers (Figure 5.10(b)). In both cases, the calculated temperature is independent of the number of layers. The interface resistance is not considered here for the contact between same materials. This agreement in a large range of parameter inputs ensures stable results for the composite structure in this study.

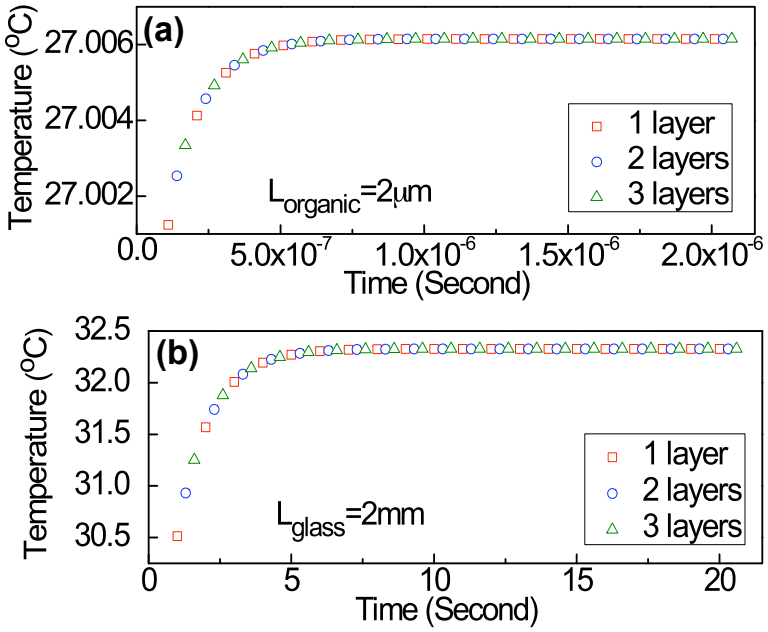

Figure 5.10: Model calculation for (a) glass and (b) organic thin film composites with one (squares), two (dots), and three (triangles) layers.

Based on OLED emission simulation considering microcavity effects, we calculated the fraction of the optical power, i.e. air/substrate mode for OLED of various thicknesses. The layers are optically described by standard matrix techniques, and the dipole is included by using additive source terms for the electric eld that depend on dipole orientation and wave polarization (see Appendix A). We integrated the optical intensity in the spherical coordinate and obtained a weighted average over representative green and red OLED emissions. Here we use the spectra of $Ir(ppy)_3$ and PQIr respectively. The optical power is calculated as $\sum_i (I_i \times \phi_i) / \sum_i \phi_i$, where I_i is the integrated optical intensity, and ϕ_i is the spectra as a function of wavelength. With the total optical power similarly calculated for source terms used in this simulation, we obtained the ratio of optical power/total power.

The simulation results for $Ir(ppy)_3$ and PQIr optical power ratio are plotted in Figure 5.11. In agreement with the calculations shown in Table 5.1 and 5.2, more than 80% of total power has to be thermally dissipated via various channels, e.g. waveguide

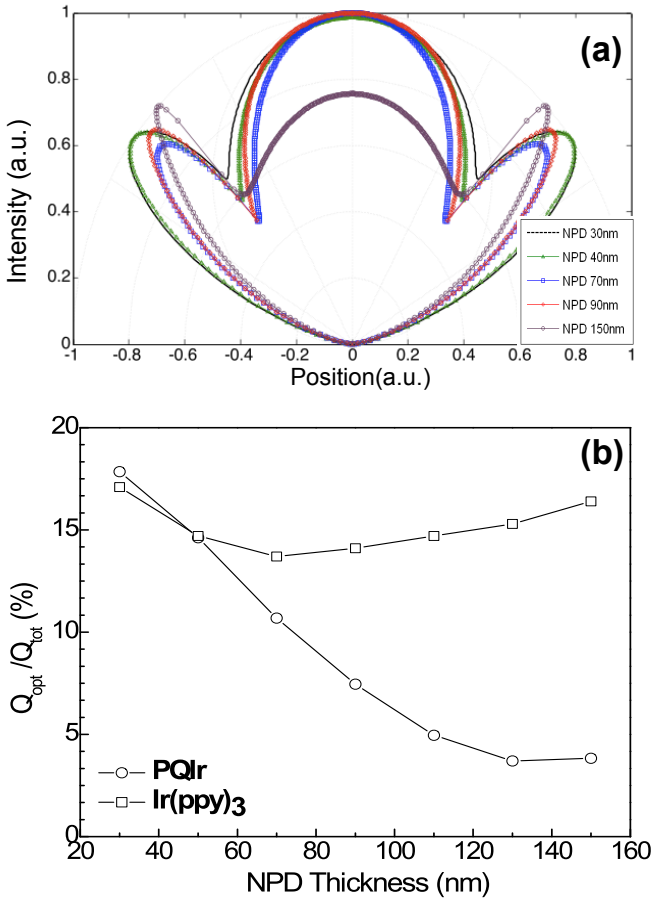

Figure 5.11: (a) Emission patterns for OLEDs under various NPD thicknesses. Simulation is based on the modification of dipole emission embedded in planar layered structures considering a completely isotropic source with 2/3 horizontal dipole and 1/3 vertical dipoles. (b) The calculated optical power percentages for $Ir(ppy)_3$- and PQIr-based OLEDs under varied NPD thicknesses.

modes, cathode modes, and absorption, etc. An observation is that microcavity effects are much stronger for PQIr-based OLED compared with $Ir(ppy)_3$-based OLED in which the optical power drops from 18% with NPD thickness of $300\mathring{A}$, to roughly 4% at $1500\mathring{A}$.

The results of the thermal power calculations under selected drive conditions are provided in Tables 5.1 and 5.2. The results as a function of time are shown in Figure 5.7, in both cases using the materials thermal properties summarized in Table 5.3. The temperatures are found by inverting the matrix in Equation 5.11b, given the thermal input vector, $\hat{Q}$. This is accomplished through a polynomial expansion whose order is determined by meeting the convergence criterion, as discussed in Appendix B. We find that a 4^{th} order polynomial results in an error of only $\pm 2\%$ compared to higher order solutions, and hence is used for all results discussed here.

From Figure 5.7, the maximum temperature increase for the green PHOLED is 10^oC at 7.0 V (corresponding to J=6.48 mA/cm^2, or Q_{tot}=454 W/m^2), and 11.5^oC for the somewhat less efficient red device at 12.0 V (corresponding to J=4.74mA/cm^2, or Q_{tot}=569 W/m^2). There are no adjustable parameters used in the calculation with the exception of those used to model convective losses; i.e. the thermal conductivity and the thickness of the air gap, as discussed below. There are only small discrepancies between the model prediction and the experimental results. The largest disagreement is for the green device at 7.0 V, where the steady-state calculated temperature is 0.9^oC higher than observed. This difference is possibly due to uncertainties in measuring device temperature arising from thermal inhomogeneities introduced by the resistive ITO contact apparent in Figure 5.3(c).

An advantage of the matrix methodology is the simplification of the calculation of the thermal transient response. For example, the response of the devices following the current pulse is modeled by introducing the Laplace transform of a step function into the heat source term. In this case, we define the thermal input function, $f(t)$,

Table 5.3: Summary of the thermal parameters for modeling.

Materials	Thickness (m)	Density (Kg/m^3)	Capacity $(J/(kg \cdot K))$	Conductivity $(W/(K \cdot m))$	Reference
Air	–	1.2	1.0×10^3	2.5×10^{-2}	[160][161]
Glass	1.0×10^{-3}	2.6×10^3	8.2×10^2	3.0	[162]
ITO	1.0×10^{-6}	7.2×10^3	3.4×10^2	8.0	[163]
Organic	1.0×10^{-7}	1.2×10^3	1.7×10^3	2.6×10^{-1}	[164]
Al	1.0×10^{-7}	3.9×10^3	9.0×10^2	2.7×10^{-1}	[165][166]
Air Gap	3.0×10^{-5}	1.2	1.0×10^3	2.5×10^{-2}	[160][161]
Encap	7.0×10^{-4}	2.6×10^3	8.2×10^2	3.0	[162]

as:

$$f(t) = \begin{cases} 0, & -\infty < t < -t_0 \\ Q, & -t_0 \leq t < 0 \\ 0, & 0 \leq t < +\infty \end{cases} \tag{5.17}$$

where t is time in second, t_0 is the duration of a constant heat flux pulse, Q. The corresponding Laplace transform is:

$$\begin{aligned} L\{f(t)\} &= Q \cdot L\{u(t+t_0)\} - Q \cdot L\{u(t)\} \\ &= Q \cdot (\frac{e^{t_0 s}}{s} - \frac{1}{s}) = \frac{Q}{s} \cdot \sum_{k=1}^{+\infty} \frac{(t_0 s)^k}{k!} \end{aligned} \tag{5.18}$$

where $u(t)$ is the unit step function. Figure 5.9 shows the thermal transient response for t_0=120s as measured for the green (Figure 5.9a) and red (Figure 5.9b) PHOLEDs using time-resolved thermal imaging (data points) compared to the transmission matrix model calculations. The measurement and the model predictions are in reasonable agreement for the duration of the cooling transient under the same bias conditions as employed in Figure 5.7, where we modeled the device turn-on transients.

To obtain the fits in Figures 5.7 and 5.9, both radiation and convection are included into the matrices that describe the composite thermal system. Indeed, R_{rad} and t_{air} are two fitting parameters in this study, where the equilibrium temperature

is sensitive to t_{air}, and the thermal transient response is somewhat sensitive to out choice of R_{rad}. The fits yield the radiative resistance, which is a parallel heat loss to both conduction and convection, giving $R_{rad} \simeq 0.2m^2K/W$ for the green device, and $R_{rad} \simeq 0.4m^2K/W$ for the red device, which agree with the ideal grey-body estimate of $1/R_{rad} = h_{rad} \simeq 5W/m^2K$. The higher thermal resistance for the red device is consistent with its lower efficiency (with PE= 4.3lm/W to 7.8lm/W for green vs. 1.3lm/W to 3.6lm/W for red; see Tables 5.1 and 5.2), and hence lower emissivity. Table 5.3 summaries the thermal parameters used for modeling the structure in Figure 5.4(a), e.g. layer thickness, material density, heat capacity, and thermal conductivity.

Developing an accurate model for convection depends strongly on the ambient conditions surrounding the device (e.g. forced air vs. a stagnant, or free, air layer, and whether a heat sink is employed, etc.). In our case, we assume free convection[167], where the thermal boundary between the device radiating surface and the ambient is modeled by an effective thermal conductivity, k_{air}, and boundary layer thickness, tair. To approximate these parameters for the PHOLEDs used in our experiments, we simulated the thermal conditions by positioning a thermometer at different distances from a semi-infinite heat surface (i.e. a hot plate) maintained at 30^oC to 40^oC. In contrast to radiation, which only depends on the temperature and emissivity of the surface, convection depends on the orientation of the hot surface, e.g. whether it is horizontal and vertical. In our case, the hot plate was positioned vertically to be comparable with the OLED orientation, although orientation was not found to significantly affect our measurements over the temperature range studied. By measuring temperature vs. distance we obtain tair is 2cm to 5cm. For matrix fitting under the conditions listed in Table 5.1 and 5.2, we assume t_{air}=1.1cm is obtained for the green device, and t_{air}=1.2cm for the somewhat hotter red PHOLED for these fits. Also, k_{air}=0.025W/K-m (see Table 5.3).

Although we have measured the specific convection conditions that apply in our

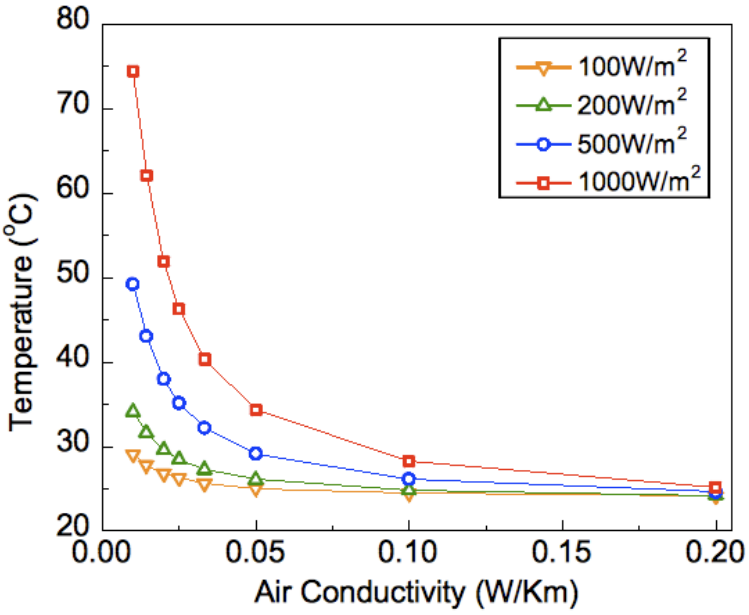

Figure 5.12: Model calculation of equilibrium temperature as a function of air conductivity under fixed heat fluxes of 100, 200, 500, and 1000W/m^2.

experiments, the sensitivity of the calculations to the parameters, especially kair, is a potentially significant source of error. This is apparent from the plot in Figure 5.12, where we calculate the device temperature as a function of $0.01<k_{air}<0.20$W/K-m for a constant thermal flux input of 100, 200, 500, and 1000W/m^2 and an ambient temperature of 25^{o}C. A sensitive dependence on the air conductivity is observed over the range: $0.01<k_{air}<0.05$W/K-m. Considering the fitted k_{air}=0.025W/K-m under free convection, this result suggests that to avoid unacceptable thermal increases at very high OLED operating powers, forced air convection is required.

Finally, we also consider the effects of thermal contact resistances, R_{int}, between the various interfaces. Its incorporation is analytically straightforward by the inclusion of interface matrices in the series product following Equation 5.10. However, the accurate measurement of R_{int} in complex composite systems such as PHOLEDs and other multilayer devices can be problematic. For the devices shown in Figure 5.4, the

most resistive interfaces are at the boundaries between ITO and the organic composite, and between the organics and the Al cathode. Previously, it has been shown[168] that for these systems, R_{int}=1×10^{-8}m^{2}K/W. Although the nonlinear dependence of the interface resistances on temperature has also been reported[169], such effects have been neglected here for simplicity.

5.4.4 Model Applications

Given that the model introduced is both straightforward to implement and is accurate for a well-defined set of thermal parameters, it is useful to apply it to PHOLEDs operating under a range of practical conditions. For example, we have applied this model to explore the effects of substrates with a variety of thermal conductivities. These include sapphire (K=35W/K-m) and Si (K=150W/K-m), as shown in Figure 5.13. Compared to glass substrates, the device temperature rise considerably smaller for a thermal power input >1kW/m^2. For example, at 5kW/m^2, the temperature rise is only 1.3^{o}C for Si, 9.8^{o}C for sapphire, and 82^{o}C for glass.

For comparison, the corresponding results obtained using conventional finite element analysis (FEA) to solve the system of partial differential equations describing the multilayer PHOLEDs are also shown in Figure 5.13 . For the FEA calculation, we use the Comsol Multiphysics solver as a test of our matrix-based approach. The systematically higher temperature obtained from FEA above 40^{o}C is possibly due to the 2D geometry assumed, where a device area of 1 mm×1 mm is employed to accommodate the grid for the ultra-thin film structure. Compared to FEA, the matrix calculation is far less computationally intensive for calculating temperature profiles of large-area devices since it simplifies the complex and time consuming calculations needed for arbitrary multi-layer structures. Furthermore, physical parameters are easily identified, and their corresponding effects on the total thermal dissipation can be efficiently analyzed. Ultimately, the matrix model allows for rapid iteration of

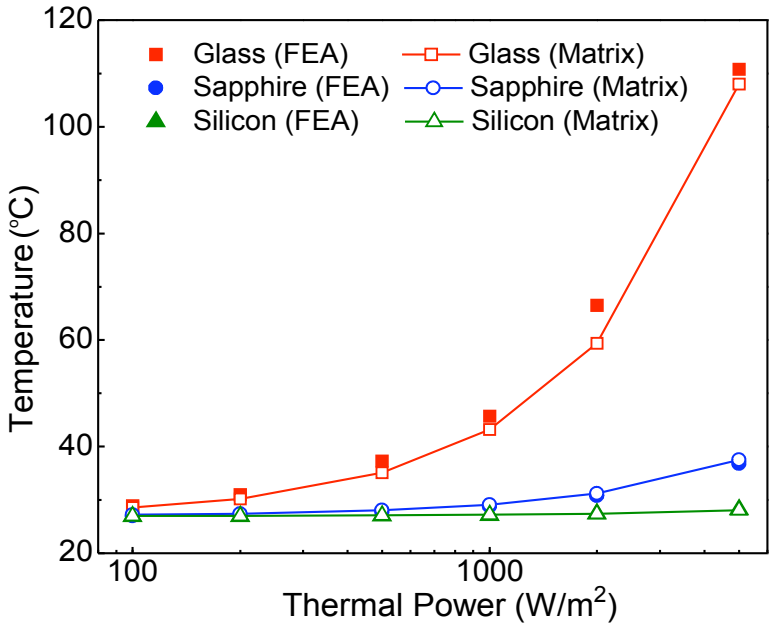

Figure 5.13: Calculated device temperature (open dots) with glass, sapphire, and silicon as substrates. Results are compared with finite element analysis (FEA, solid dots).

both structure and materials properties that can be used to optimize thermal management in complex structures. This capability has proven invaluable in the design of the optical properties of multilayer structures using an analogous, optical matrix approach.[143]

A second application is to estimate the temperature increase under very high current pulses required for high intensity illumination or even electrically driven organic lasers.[170] Figure 5.14 shows the thermal response following 1, 5, and 10 ms pulses for an ultrahigh thermal flux of 106 W/m^2. For each case, the thermal parameters and device structures are the same with the large-area devices. Here, ? is used, similar to that used for the large-area red device. Also, for these calculations, we assume t_{air}=5 mm compared to that used under lower power, steady-state operation of the large-area devices (where we measure t_{air}=1.1 cm to 1.2 cm). In this case, we assume that an equilibrium air boundary does not fully develop over the very short duration

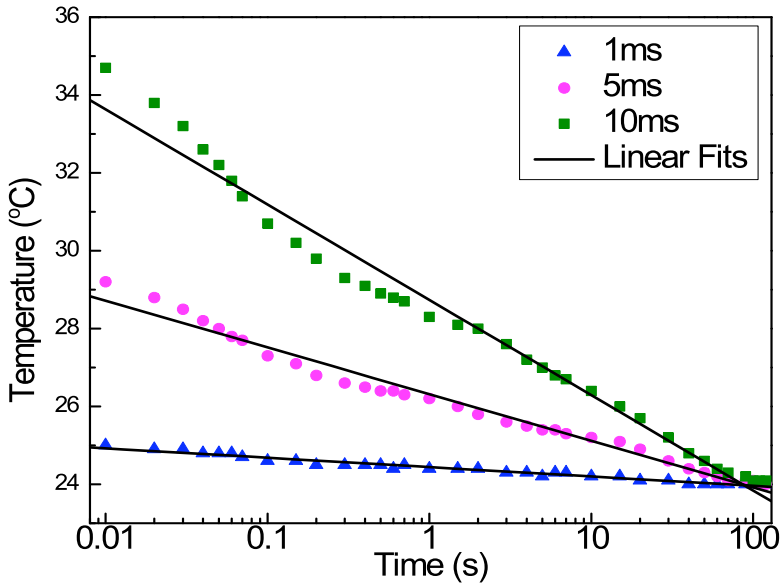

Figure 5.14: Time response of PHOLED temperature (solid dots) at various pulse widths of 1ms, 5ms, and 10ms under fixed, ultrahigh thermal input power of 10^6W/m^2. Linear fits are displayed as solid lines. The physical and thermal parameters are the same as for the large-area devices. Now, $R_{rad} \approx 0.4$m^{2}K/W, whereas t_{air} ≈5mm is used here compared to that of the large-area devices (2 to 4cm) due to the short pulse duration.

of the heat pulse.

While the thermal response is somewhat sensitive to the choice of tair, we observe a nearly logarithmic decay in temperature is observed, as shown the solid lines in Figure 5.14. Maximum temperatures of 25.0, 28.9, and 33.9^{o}C for pulse durations of 1, 5 and 10 ms, respectively. Clearly, the effects of convection under both steady-state and pulsed operation are complex, and are beyond the scope of this study. Hence, it is important that further study of these effects are required to fully understand thermal transients under very high device excitation.

To expand the results in white lighting sources, we now focus on a pair of all-phosphorescent 15cm×15cm OLED light panels with high power efficiency and long lifetime. Shown in Figure 5.15, Panel 1 has 62 lm/W power efficiency, CRI=81 and

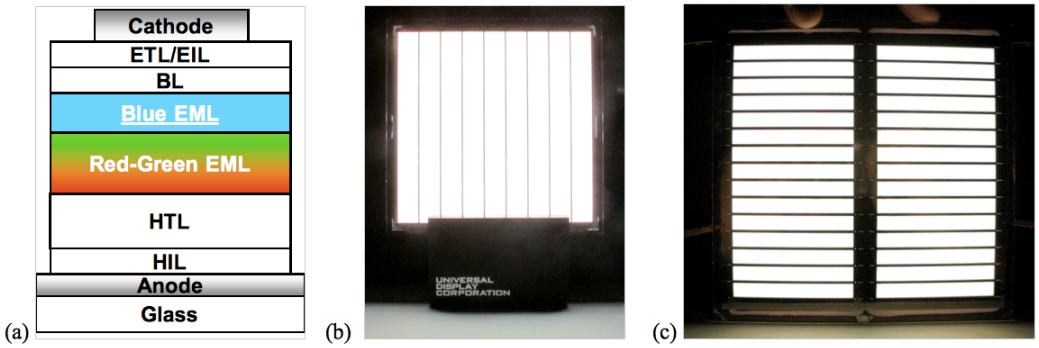

Figure 5.15: (a)Structure of all-phosphorescent OLED; (b) Panel 1; (c) Panel 2. [176]

lifetime of 18,000 hrs at 1,000cd/m^2, and Panel 2 has 58 lm/W power efficiency, CRI=82 and lifetime of 30,000 hrs at 1,000cd/m^2.[176]

Low operating temperature is demonstrated in Figure 5.16, where surface temperature at the center of the emissive region for each 15 cm×15 cm panel is plotted against luminous emittance. Data are also included for a smaller (approximately 8 cm x 8 cm) commercial fluorescent panel. At 3,000 cd/m^2, the panels with all-phosphorescent emitters both have 49 lm/W power efficiency, with surface temperature = 29.4^{o}C for Panel 1 and surface temperature = 27.2^{o}C for Panel 2. Ambient temperature was 20.0^{o}C for these measurements. It is likely that temperature is higher for Panel 1 due to its larger aperture ratio, which results in higher power density. At the same luminance, the panel with all-fluorescent emitters has power efficiency of 16 lm/W and surface temperature = 40.5^{o}C. All panels use bus lines and multiple electrode contacts to minimize Joule heating.

5.4.5 Conclusions

In this work, we introduce a transmission matrix formalism to accurately model the thermal response of multilayer composite structures typical of OLEDs and other optoelectronic devices. The model, based on Laplace transforms, is used to determine the steady-state and transient thermal response of multilayer PHOLEDs used in display and lighting applications. The model results are compared with measurements

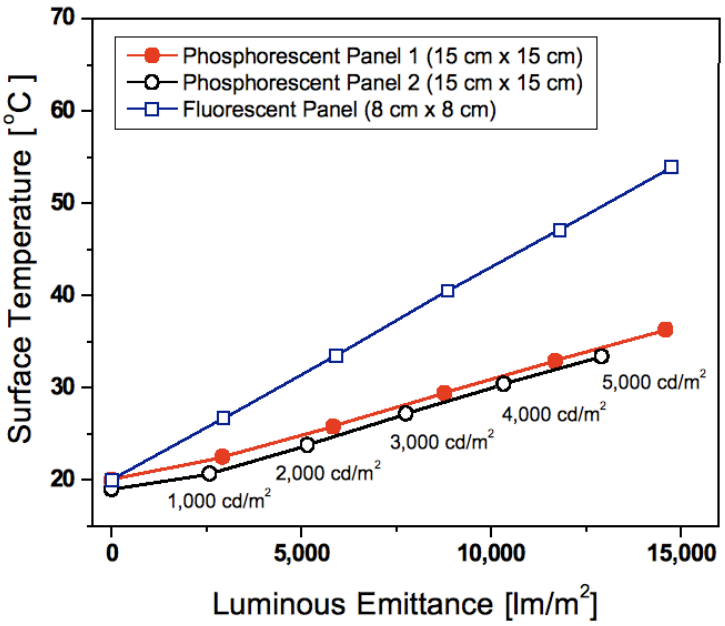

Figure 5.16: Surface temperature of Panel 1 and 2. A well-designed commercial fluorescent panel is shown as comparison.[176]

of encapsulated large-area PHOLEDs obtained via thermal imaging. The formalism is used to account for diverse series and parallel power loss channels including conduction, convection, light emission and thermal radiation. Agreement is obtained between the model and observation using only measured properties such as thermal conduction, interface thermal resistance, and convective boundary layers, thereby validating the approach.

The results offer insights for temperature management of organic electronic devices, and in particular of OLEDs employed at high intensity, as required for lighting applications. For example, forced convection can lead to doubling of the effective air conductivity, thereby lowering device temperature at high drive currents. The model, which is similar to transmission matrix formalisms used to calculate optical fields in multilayer composites, can be adapted to the study of a variety of thermal conditions and device structures, making this work a significant advance in understanding and controlling the temperature response of a range of important optoelectronic devices.

CHAPTER VI

Conclusions and Future Outlook

The commercialization of OLEDs for solid-state lighting has accelerated during the last several years, and the field is still expanding. In this concluding chapter, we provide perspective on several challenges that remain, primarily efficiency improvement, and thermal management in large-area applications.

Conventional OLEDs discussed in this thesis are limited to thin un-doped electron- and hole-transporting layers. The conductivity of the charge carrier transport layer is low, leading to ohmic losses. Also the driving voltage is high due to the high barrier from the electrode into the transport layers. Aiming for highest possible power efficiency, a *p-i-n* structure employs doped transport layers.

Shown in Figure 6.1, the *p-i-n* bottom emission OLEDs consist of five organic layers: hole-transporting layer(HTL), electron transporting layer(ETL), electron-blocking layer(EBL), hole-blocking layer(HBL), and emission layer(EML).[171] A good choice of *p*-type doping is ZnPc as matrix, doped by F_4-TCNQ, as presented by Pfeiffer et al.[172] A stable and highly conductive *n*-doping is reported by Novaled AG, consisting of a matrix NET5 and a dopant NDN1.[171] As a result of doping, hole and electron transport (conductivities above $\sim 10^{-5}$S/cm) as well as charge carrier injection (due to band bending) are dramatically enhanced. The operating voltage is decreased by several volts by doping the transport layer of the device. Additionally,

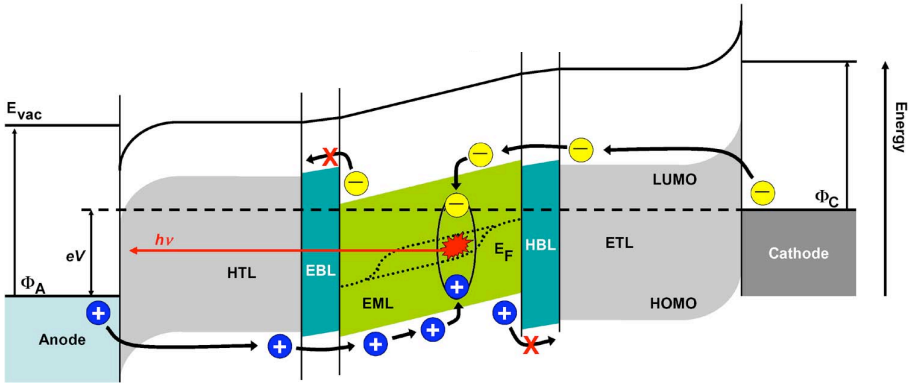

Figure 6.1: *p-i-n* OLED structure. Bend bending is observed at the doped organic/electrod interfaces. (R. Meerheim [171])

a larger selection of electrode materials becomes available due to the very low driving voltage from p and n doping.

Besides optimized charge transport and injection, the efficiency of white OLEDs can be further increased by improving the light out-coupling. In a conventional OLED, over 50% of the emitted light is trapped in the high-index organic and ITO layers reducing the efficiency of the device. Schwarts et al. reported η_p=28lm/W at 1000cd/m^2 by using microlens [173]; and Sun et al. realized η_p=38lm/W at 500cd/m^2 with a low-index grid (LIG) on the bottom electrode [174]. Other than the two commonly used backside patterning, frontside patterning (e.g. Aerogel) also has demonstrated potential enhancement.[175]

Another important issue is the thermal management. We have introduced a systematic analysis on the thermal properties of OLEDs. Although the amount of heat generated during panel operation has been dramatically reduced by adopting optimized structures and phosphorescent materials, operating at high brightness and over large areas may still lead to increases in the operating temperature of a panel. This increase of temperature is demonstrated in Chapter V where power is lost due to the resistance of ITO. A low resistance gold bus line has been introduced at the anode side to increase the light uniformity and control the temperature rise.[176]

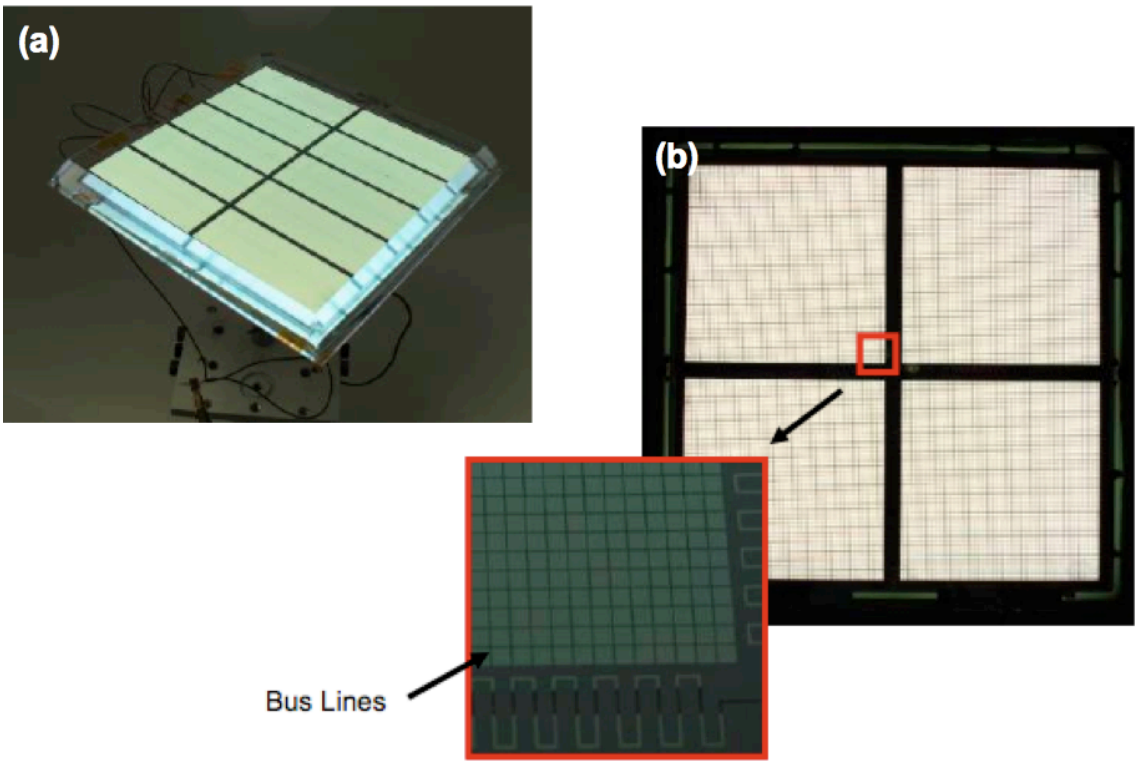

Figure 6.2: (a) 15cm×15cm lighting panel with a performance of 42.6lm/W at 1000cd/m^2 using an outcoupling block with index matching fluid (measured in an integrating sphere). (b) WOLED panel with four pixels in series circuit. There are small buss lines through out each pixels to improve the uniformity (inset). (Universal Display Corp.)

Shown in Figure 6.2, the 15cm×15cm lighting panel has a performance of 42.6lm/W at 1000cd/m^2 using an outcoupling block with index matching fluid (measured in an integrating sphere), and there are small buss lines through out each pixels to improve the uniformity

Research and development in the field of OLEDs is proceeding rapidly and may lead to future applications in heads-up displays, automotive dashboards, billboard-type displays, home and office lighting and flexible displays. With the promise of being ten times more efficient than incandescent lighting, OLEDs will change the way we light our homes and businesses. Many solid-state lighting products are beginning to appear on the market, and DOE supported research and development continues to attack many issues that limit performance.

Power consumption is also the reason why OLED is a better choice for portable devices than its LED counterpart. Light sources based on organic electroluminiscent materials offer the potential to make a high light intensity possible at a low energy consumption on mechanically flexible substrates. Key advantages of the organic luminescence are the chemical variability of the organic light-emitting diodes, allowing virtually any color including white, and the thin film system, allowing large-area and low-cost deposition, and the possibility to use thin and even flexible substrates to realize a novel class of lighting and display solutions not possible for other technologies.

APPENDICES

APPENDIX A

Optical Matrix based on Dipole Emission

In Chapter V, we applied the standard matrix techniques for optical simulation in multi-layer structures, where the dipole is included by using additive source terms for the electric eld that depend on dipole orientation and wave polarization. Here we provide some details on the techniques.

In the plane-wave basis, fields depend on layer indices n_j only through their complex z-wave-vector component $k_{z,j}$, which obeys the wave equation

$$k_{z,j}^2 + k_{||}^2 = \frac{\omega^2}{c^2} n_j^2 \tag{A.1}$$

where $k_{z,j} = \omega n_j (cos\theta_j)/c$ is the perpendicular component of the wave vector, θ_j is the angle between the wave vector and the z axis. $k_{z,j}$ is real for plane waves and becomes purely imaginary for evanescent waves in a lossless dielectric. The use of $k_{z,j}$ is thus convenient to treat plane and evanescent waves on the same footing, and $k_{||}$ is conserved throughout all interfaces. Both plane and evanescent waves are subject to reflections, transmission, etc.

The radiation pattern of electric dipoles in an unbounded medium is needed in order to deduce source terms for an electric field based on k_z. There are three basic configurations of radiation patterns for electric dipoles, as shown in Figure. The

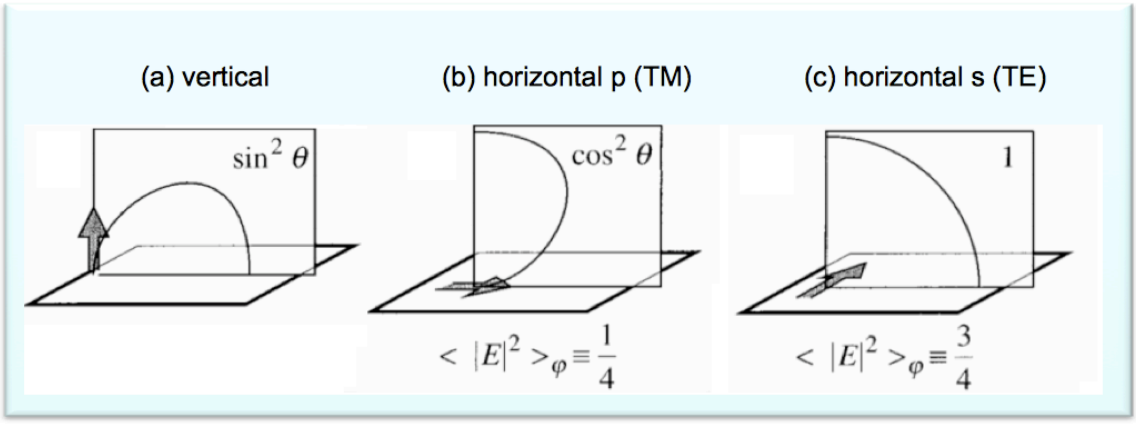

Figure A.1: Bare emission pattern of (a) a vertical dipole in p (TM)modes, (b) a horizontal dipole in p (TM) modes, and (c) a horizontal dipole in s (TE) modes. (inset) The azimuthal average for horizontal dipoles.

vertical dipole, denoted v, radiates only p (TM) waves. For the horizontal dipole, denoted h radiates both p (TM) and s (TE) waves.

$$(\frac{dP}{d\Omega})^{(v)} = \frac{3}{8\pi} sin^2\theta_i \tag{A.2a}$$

$$(\frac{dP}{d\Omega})^{(h),s} = \frac{3}{16\pi} \tag{A.2b}$$

$$(\frac{dP}{d\Omega})^{(h),p} = \frac{3}{16\pi} cos^2\theta_i \tag{A.2c}$$

where $\frac{dP}{d\Omega}$ is power per unit solid angle, θ_1 is the off-normal emission angle in medium i, and $sin\theta_1 = k_{||}/k_1$. The total power through 4π solid angle is unity, and the ratio of s to p power is 3:1. When the above source terms, propagating along $\pm z$, are expressed as a function of $k_{||}$ and $k_{z,i}$, we have normalized source terms for the horizontal and vertical dipoles.

$$A_{\uparrow,\downarrow}^{(v),p} = \sqrt{\frac{3}{8\pi}}\sin\theta_i = \sqrt{\frac{3}{8\pi}}\frac{k_{||}}{k_i} \tag{A.3a}$$

$$A_{\uparrow,\downarrow}^{(v),s} = 0 \tag{A.3b}$$

$$A_{\uparrow,\downarrow}^{(h),p} = \pm\sqrt{\frac{3}{16\pi}}cos\theta_i = \pm\sqrt{\frac{3}{16\pi}}\frac{k_{z,i}}{k_i} \tag{A.3c}$$

$$A_{\uparrow,\downarrow}^{(h),p} = \pm\sqrt{\frac{3}{16\pi}} \tag{A.3d}$$

where $\uparrow$ and $\downarrow$ denote the $+z$ and $-z$ directions. For a completely isotropic source, one obvious rule is:

$$P^{(iso)} = \frac{2}{3}P^{(h)} + \frac{1}{3}P^{(v)} \tag{A.4}$$

Consider the source terms as additive between field vectors on each side of the source layer, outside fields are easily calculated for the desired modes:

$$\begin{bmatrix} a_{11} & a_{12} \\ a_{21} & a_{22} \end{bmatrix} \cdot \begin{bmatrix} 0 \\ E_0(\theta_0) \end{bmatrix} = \begin{bmatrix} E_{10\uparrow} \\ E_{10\downarrow} \end{bmatrix} \tag{A.5a}$$

$$\begin{bmatrix} b_{11} & b_{12} \\ b_{21} & b_{22} \end{bmatrix} \cdot \begin{bmatrix} E_2(\theta_2) \\ 0 \end{bmatrix} = \begin{bmatrix} E_{12\uparrow} \\ E_{12\downarrow} \end{bmatrix} \tag{A.5b}$$

We now deduct the outside field from multilayer matrices as shown in Figure A.2. With simple algebra, the fields in any layer of the structure can be obtained. Spectral spread of the source can be accounted for by summation of normalized patterns at each wavelength with adequate weighting.

$$P_{out} = \int_0^{\pi/2} 2\pi\Pi(\theta)sin\theta d\theta \tag{A.6}$$

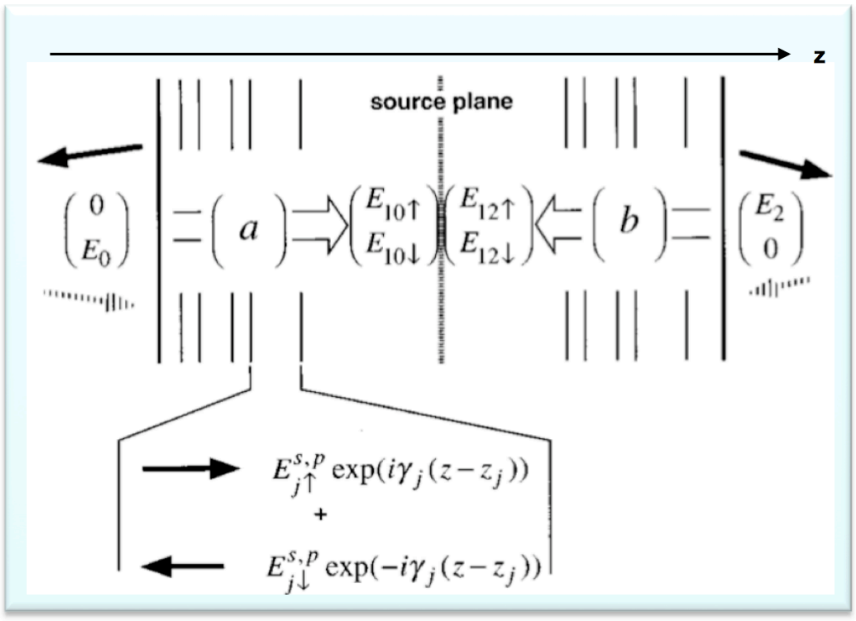

Figure A.2: Sketch of a layered structure with a source plane inside and matrices describing the propagation of electric fields from the outside to the source.

where $\Pi = dP/d\Omega dS$ is the power per unit solid angle and unit surface. and P_{out} is the extracted power on the chosen side.

APPENDIX B

Numerical System Stability

Numerical system stability is important for obtaining an accurate calculation of the inverse Laplace transform. Here, the matrix elements in Equation 5.8 are calculated using a series expansion of the form: [177]

$$A_i = D_i = cosh(L_i\sqrt{s/a_i}) = \sum_{k=0}^{\infty} \frac{L_i^{2k}}{(2k)!a_i^k} s^k \tag{B.1a}$$

$$B_i = R_i sinh(L_i\sqrt{s/a_i})/(L_i\sqrt{s/a_i}) = R_i \sum_{k=0}^{\infty} \frac{L_i^{2k}}{(2k+1)!a_i^k} s^k \tag{B.1b}$$

$$C_i = L_i\sqrt{s/a_i} sinh(L_i\sqrt{s/a_i})/R_i = \frac{1}{R_i} \sum_{k=1}^{\infty} \frac{L_i^{2k}}{(2k-1)!a_i^k} s^k \tag{B.1c}$$

where s is the Laplace variable, A_i, B_i, and C_i are the matrix elements of the i^{th} layer as defined in Equation 5.8. Also L_i, R_i, and a_i are the thickness, thermal resistance, and the thermal diffusivity of the i^{th} layer.

The convergence of these polynomial expansions must be tested for convergence to be rigorously valid and free from large errors. A convergence problem originates from the instability of the inverse Laplace transformation function obtained from the power series in Equation B.1.[177] As shown in Figure B.1, the temperature

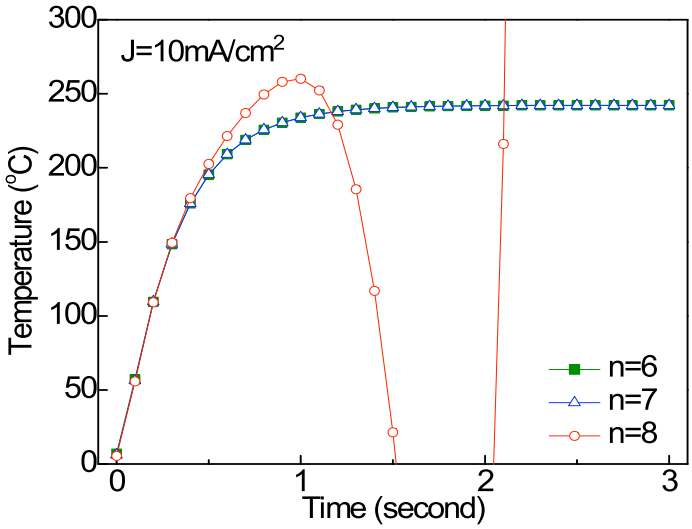

Figure B.1: Heat transfer for the given composite is calculated in difference orders (n=6,7,8), where a normalized scale is presented to show when the fluctuation happens. With proper manipulation of complex numbers, the method guarantees a stable calculation with sufficient accuracy.

rise for a model, 1-mm-thick glass slab where $Q_{therm} = 200W/m^2$ is calculated for various polynomial orders (n=6, 7, 8), with the roots of the truncated polynomial provided in Table B.1. A stable solution requires that all poles have a negative real part in the case of n=6, and 7. For n=8, two roots have a positive real part, corresponding to the fluctuation shown in Figure B.1. From the figure, the truncated denominator polynomial guarantees a stable solution with an error of $\leq$2% for $n \leq$7. For calculations in this study, we find that n=4 provides sufficient accuracy while being computationally efficient.

Table B.1: Roots of the truncated denominator polynomial.

Root	n=6	n=7	n=8
1st	-0.87	-0.86	-0.86
2nd	-7.73	-7.81	-7.81
3rd	-5.65+24.25i	-16.2	-18.82+21.4i
4th	-5.65-24.25i	-16.3+13.09i	-18.82-21.4i
5th	-13.27+6.49i	-16.3-13.09i	-19.87+4.51i
6th	-13.27-6.49i	-3.21+34.5i	-19.87-4.51i
7th		-3.21-34.5i	0.814+46.2i
8th			0.814-46.2i

APPENDIX C

Matrix Code in Maple

```
> restart :
> with(inttrans) :
> with(LinearAlgebra) :
>
> ################Parameter Setup#################
>  # sig: thermal diffusivity
>  # r: thermal resistance
>  # t: film thickness
>  # Rrad: thermal resistance to radiation, 0.002 for green, 0.004 for red
>  # riface: interface resistance, value taken from literature
>  # n: polynomial order
> sigair := 1·10^-5 : rair := 50 : tair := 0.0011 :
> sigglass := 1.4·10^-6 : rglass := 0.4 : tglass := 0.0007 :
> sigITO := 3.3·10^-6 : rITO := 0.2 : tITO := 1·10^-6 :
> sigOrg := 1.3·10^-7 : rOrg := 5.0 : tOrg := 1·10^-7 :
> sigAl := 7.7·10^-6 : rAl := 0.04 : tAl := 10^-7 :
> Rrad := 0.002 :
> riface := 1·10^-8 :
> n := 4 :
>
```

> ##############**Building Matrices**###############

> $A0 := \sum_{k=0}^{n} \frac{tair^{2k}}{(2k)!\,(\text{sigair})^{k}} s^{k} : \quad B0 := tair \cdot rair \sum_{k=0}^{n} \frac{tair^{2k}}{(2k+1)!\,(sigair)^{k}} s^{k} : C0$

$:= \frac{1}{tair \cdot \text{rair}} \sum_{k=1}^{n} \frac{tair^{2k}}{(2k-1)!\,(\text{sigair})^{k}} s^{k} : D0 := \sum_{k=0}^{n} \frac{tair^{2k}}{(2k)!\,(\text{sigair})^{k}} s^{k}$: ***#Air Matrix***

> $A1 := \sum_{k=0}^{n} \frac{tglass^{2k}}{(2k)!\,(sigglass)^{k}} s^{k} : \quad B1 := \text{tglass} \cdot \text{rglass} \sum_{k=0}^{n} \frac{tglass^{2k}}{(2k+1)!\,(sigglass)^{k}} s^{k} : C1$

$:= \frac{1}{\text{tglass} \cdot \text{rglass}} \sum_{k=1}^{n} \frac{tglass^{2k}}{(2k-1)!\,(sigglass)^{k}} s^{k} : D1 := \sum_{k=0}^{n} \frac{tglass^{2k}}{(2k)!\,(sigglass)^{k}} s^{k}$: ***#Glass Matrix***

> $A2 := \sum_{k=0}^{n} \frac{(tITO)^{2k}}{(2k)!\,(sigITO)^{k}} s^{k} : \quad B2 := rITO \cdot tITO \sum_{k=0}^{n} \frac{(tITO)^{2k}}{(2k+1)!\,(sigITO)^{k}} s^{k} : C2$

$:= \frac{1}{tITO \cdot rITO} \sum_{k=1}^{n} \frac{(tITO)^{2k}}{(2k-1)!\,(sigITO)^{k}} s^{k} : D2 := \sum_{k=0}^{n} \frac{(tITO)^{2k}}{(2k)!\,(sigITO)^{k}} s^{k}$: ***#ITO Matrix***

> $A3 := \sum_{k=0}^{n} \frac{(tOrg)^{2k}}{(2k)!\,(sigOrg)^{k}} s^{k} : B3 := rOrg \cdot tOrg \sum_{k=0}^{n} \frac{(tOrg)^{2k}}{(2k+1)!\,(sigOrg)^{k}} s^{k} : C3$

$:= \frac{1}{\text{tOrg} \cdot rOrg} \sum_{k=1}^{n} \frac{(tOrg)^{2k}}{(2k-1)!\,(sigOrg)^{k}} s^{k} : D3 := \sum_{k=0}^{n} \frac{(tOrg)^{2k}}{(2k)!\,(sigOrg)^{k}} s^{k}$: ***#Organic Matrix***

> $A4 := \sum_{k=0}^{n} \frac{(tAl)^{2k}}{(2k)!\,(sigAl)^{k}} s^{k} : \quad B4 := tAl \cdot rAl \sum_{k=0}^{n} \frac{(tAl)^{2k}}{(2k+1)!\,(sigAl)^{k}} s^{k} : C4$

$:= \frac{1}{\text{tAl} \cdot rAl} \sum_{k=1}^{n} \frac{(tAl)^{2k}}{(2k-1)!\,(sigAl)^{k}} s^{k} : D4 := \sum_{k=0}^{n} \frac{(tAl)^{2k}}{(2k)!\,(sigAl)^{k}} s^{k}$: ***#Al Matrix***

> $A5 := \sum_{k=0}^{n} \frac{(3 \cdot 10^{-5})^{2k}}{(2k)!\,(\text{sigair})^{k}} s^{k} : \quad B5 := 3 \cdot 10^{-5} \cdot rair \sum_{k=0}^{n} \frac{(3 \cdot 10^{-5})^{2k}}{(2k+1)!\,(sigair)^{k}} s^{k} : C5$

$:= \frac{1}{3 \cdot 10^{-5} \cdot \text{rair}} \sum_{k=1}^{n} \frac{(3 \cdot 10^{-5})^{2k}}{(2k-1)!\,(\text{sigair})^{k}} s^{k} : D5 := \sum_{k=0}^{n} \frac{(3 \cdot 10^{-5})^{2k}}{(2k)!\,(\text{sigair})^{k}} s^{k}$: ***#Air Gap Marix***

> $A6 := \sum_{k=0}^{n} \frac{tglass^{2k}}{(2k)!\,(sigglass)^{k}} s^{k} : \quad \text{B6} := \text{tglass} \cdot \text{rglass} \sum_{k=0}^{n} \frac{tglass^{2k}}{(2k+1)!\,(sigglass)^{k}} s^{k} : C6$

$:= \frac{1}{\text{tglass} \cdot \text{rglass}} \sum_{k=1}^{n} \frac{tglass^{2k}}{(2k-1)!\,(sigglass)^{k}} s^{k} : D6 := \sum_{k=0}^{n} \frac{tglass^{2k}}{(2k)!\,(sigglass)^{k}} s^{k}$: ***#Glass Matrix***

> $A7 := \sum_{k=0}^{n} \frac{tair^{2k}}{(2k)!\,(\text{sigair})^{k}} s^{k} : \quad B7 := tair \cdot rair \sum_{k=0}^{n} \frac{tair^{2k}}{(2k+1)!\,(\text{sigair})^{k}} s^{k} : C7$

$:= \frac{1}{rair \cdot tair} \sum_{k=1}^{n} \frac{tair^{2k}}{(2k-1)!\,(\text{sigair})^{k}} s^{k} : D7 := \sum_{k=0}^{n} \frac{tair^{2k}}{(2k)!\,(\text{sigair})^{k}} s^{k}$: ***#Air Matrix***

> $Aiface := 1 : \quad Biface := riface : Ciface := 0 : Diface := 1 : \#Aiface := \sum_{k=0}^{n} \frac{tiface^{2k}}{(2k)!\,(\text{sigiface})^{k}} s^{k} :$

$Biface := tiface \cdot riface \sum_{k=0}^{n} \frac{tiface^{2k}}{(2k+1)!\,(sigiface)^{k}} s^{k} : Ciface$

$:= \frac{1}{tiface \cdot riface} \sum_{k=1}^{n} \frac{tiface^{2k}}{(2k-1)!\,(\text{sigiface})^{k}} s^{k} : Diface := \sum_{k=0}^{n} \frac{tiface^{2k}}{(2k)!\,(\text{sigiface})^{k}} s^{k} :$

#Interface Marix

```
> V0 := Matrix([[A0, B0], [C0, D0]]) : V1 := Matrix([[A1, B1], [C1, D1]]) : V2 := Matrix([[A2,
    B2], [C2, D2]]) : V3 := Matrix([[A3, B3], [C3, D3]]) : V4 := Matrix([[A4, B4], [C4, D4]]) :
    V5 := Matrix([[A5, B5], [C5, D5]]) : V6 := Matrix([[A6, B6], [C6, D6]]) : V7
     := Matrix([[A7, B7], [C7, D7]]) : Viface := Matrix([[Aiface, Biface], [Ciface, Diface]]) :
> Mm := Multiply(Multiply(V3, Viface), Multiply(V2, Viface)) : ML := Multiply(Mm, Multiply(V1,
    V0)) : Mn := Multiply(Multiply(V5, V6), V7) : MR := Multiply(Multiply(Multiply(V3, Viface),
    V4), Mn) :
> AL := simplify(ML[1, 1]) : BL := simplify(ML[1, 2] − Rrad) : CL := simplify(ML[2, 1]) : DL
     := simplify(ML[2, 2]) : AR := simplify(MR[1, 1]) : BR := simplify(MR[1, 2] − Rrad) : CR
     := simplify(MR[2, 1]) : DR := simplify(MR[2, 2]) :
>
>
> ##############Device Heat-up###############
> Q1 := 166 : Q2 := 228 : Q3 := 294 : Q4 := 376 : #This is calculated Qtherm, green
> #Q1:=161: Q2:=243: Q3:=345: Q4:=470: #This is calculated Qtherm, red
> Ts1 := simplify( 1/(DR/BR + DL/BL) · Q1/s + 300/s ) : Tt1 := invlaplace(Ts1, s, t) : Ct1 := Tt1 − 276 :
> Ts2 := simplify( 1/(DR/BR + DL/BL) · Q2/s + 300/s ) : Tt2 := invlaplace(Ts2, s, t) : Ct2 := Tt2 − 276 :
> Ts3 := simplify( 1/(DR/BR + DL/BL) · Q3/s + 300/s ) : Tt3 := invlaplace(Ts3, s, t) : Ct3 := Tt3 − 276 :
> Ts4 := simplify( 1/(DR/BR + DL/BL) · Q4/s + 300/s ) : Tt4 := invlaplace(Ts4, s, t) : Ct4 := Tt4 − 276 :
> plot([Re(eval(Ct1)), Re(eval(Ct2)), Re(eval(Ct3)), Re(eval(Ct4))], t = 1 ..300)
```

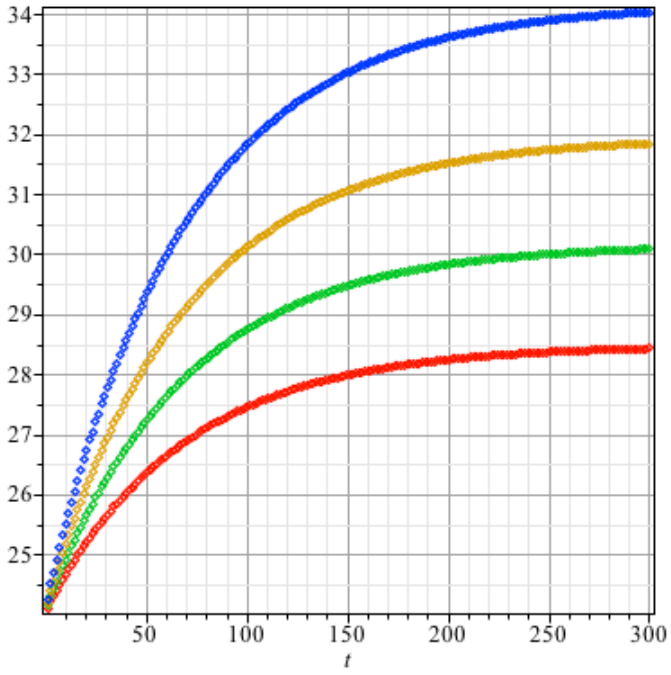


```
> #for i from 1 by 5 to 300 do print(Re(eval(Ct4, t = i))) end do #use this line to obtain data list
>
```

> **##########Device Cool-down################**

> $a := 180 : b := 200 : c := 170 : d := 180 : \#green$

> $\#a := 190: \ b := 185 : c := 180 : d := 177 : \#red$

> $$TsK1 := simplify\left(\frac{1}{\frac{DR}{BR}+\frac{DL}{BL}}\cdot\frac{Q1}{s}\left(a\cdot s+\frac{(a\cdot s)^2}{2!}+\frac{(a\cdot s)^3}{3!}+\frac{(a\cdot s)^4}{4!}+\frac{(a\cdot s)^5}{5!}+\frac{(a\cdot s)^6}{6!}\right)+\frac{300}{s}\right) : TtK1 := invlaplace(TsK1, s, t) : CtK1 := TtK1 - 276 :$$

> $$TsK2 := simplify\left(\frac{1}{\frac{DR}{BR}+\frac{DL}{BL}}\cdot\frac{Q2}{s}\left(b\cdot s+\frac{(b\cdot s)^2}{2!}+\frac{(b\cdot s)^3}{3!}+\frac{(b\cdot s)^4}{4!}+\frac{(b\cdot s)^5}{5!}+\frac{(b\cdot s)^6}{6!}\right)+\frac{300}{s}\right) : TtK2 := invlaplace(TsK2, s, t) : CtK2 := TtK2 - 276 :$$

> $$TsK3 := simplify\left(\frac{1}{\frac{DR}{BR}+\frac{DL}{BL}}\cdot\frac{Q3}{s}\left(c\cdot s+\frac{(c\cdot s)^2}{2!}+\frac{(c\cdot s)^3}{3!}+\frac{(c\cdot s)^4}{4!}+\frac{(c\cdot s)^5}{5!}+\frac{(c\cdot s)^6}{6!}\right)+\frac{300}{s}\right) : TtK3 := invlaplace(TsK3, s, t) : CtK3 := TtK3 - 276 :$$

> $$TsK4 := simplify\left(\frac{1}{\frac{DR}{BR}+\frac{DL}{BL}}\cdot\frac{Q4}{s}\left(d\cdot s+\frac{(d\cdot s)^2}{2!}+\frac{(d\cdot s)^3}{3!}+\frac{(d\cdot s)^4}{4!}+\frac{(d\cdot s)^5}{5!}+\frac{(d\cdot s)^6}{6!}\right)+\frac{300}{s}\right) : TtK4 := invlaplace(TsK4, s, t) : CtK4 := TtK4 - 276 :$$

> $plot([\mathrm{Re}(eval(CtK1)), \mathrm{Re}(eval(CtK2)), \mathrm{Re}(eval(CtK3)), \mathrm{Re}(eval(CtK4))], t = 25..600)$

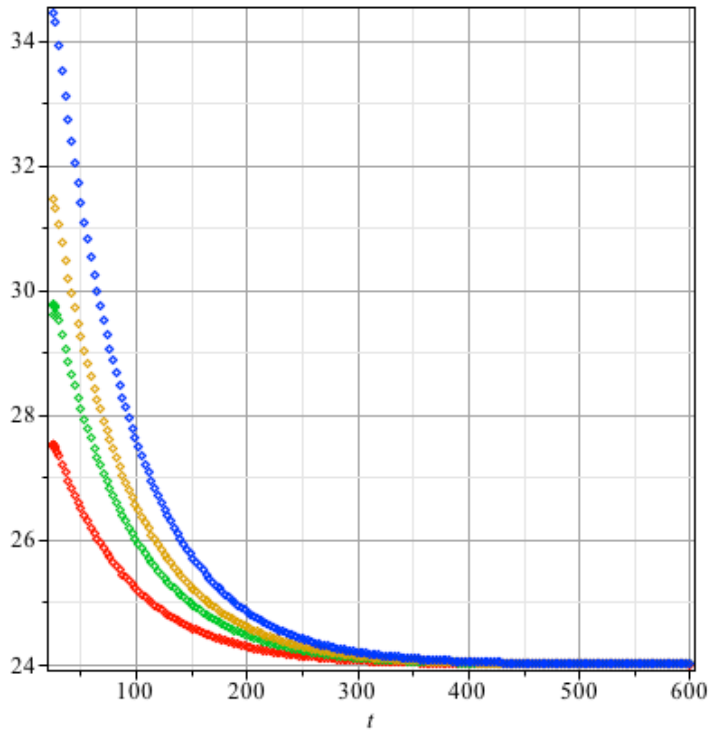

> **###############Pulse Operation###############**

> $Q_{pulse} := 1000000$:

> $a := 0.001 : b := 0.005 : c := 0.01$:

> $TsK1 := simplify\left(\frac{1}{\frac{DR}{BR} + \frac{DL}{BL}} \cdot \frac{Q_{pulse}}{s} \left(a \cdot s - \frac{(a \cdot s)^2}{2!} + \frac{(a \cdot s)^3}{3!} - \frac{(a \cdot s)^4}{4!} + \frac{(a \cdot s)^5}{5!} - \frac{(a \cdot s)^6}{6!} + \frac{(a \cdot s)^7}{7!} - \frac{(a \cdot s)^8}{8!} + \frac{(a \cdot s)^9}{9!} \right) + \frac{300}{s} \right) : TtK1 := invlaplace(TsK1, s, t) : CtK1 := TtK1 - 276$:

> $TsK2 := simplify\left(\frac{1}{\frac{DR}{BR} + \frac{DL}{BL}} \cdot \frac{Q_{pulse}}{s} \left(b \cdot s - \frac{(b \cdot s)^2}{2!} + \frac{(b \cdot s)^3}{3!} - \frac{(b \cdot s)^4}{4!} + \frac{(b \cdot s)^5}{5!} - \frac{(b \cdot s)^6}{6!} + \frac{(b \cdot s)^7}{7!} - \frac{(b \cdot s)^8}{8!} + \frac{(b \cdot s)^9}{9!} \right) + \frac{300}{s} \right) : TtK2 := invlaplace(TsK2, s, t) : CtK2 := TtK2 - 276$:

> $TsK3 := simplify\left(\frac{1}{\frac{DR}{BR} + \frac{DL}{BL}} \cdot \frac{Q_{pulse}}{s} \left(c \cdot s - \frac{(c \cdot s)^2}{2!} + \frac{(c \cdot s)^3}{3!} - \frac{(c \cdot s)^4}{4!} + \frac{(c \cdot s)^5}{5!} - \frac{(c \cdot s)^6}{6!} + \frac{(c \cdot s)^7}{7!} - \frac{(c \cdot s)^8}{8!} + \frac{(c \cdot s)^9}{9!} \right) + \frac{300}{s} \right) : TtK3 := invlaplace(TsK3, s, t) : CtK3 := TtK3 - 276$:

> $plot([\mathrm{Re}(eval(CtK1)), \mathrm{Re}(eval(CtK2)), \mathrm{Re}(eval(CtK3))], t = 0.1 \ldots 150)$

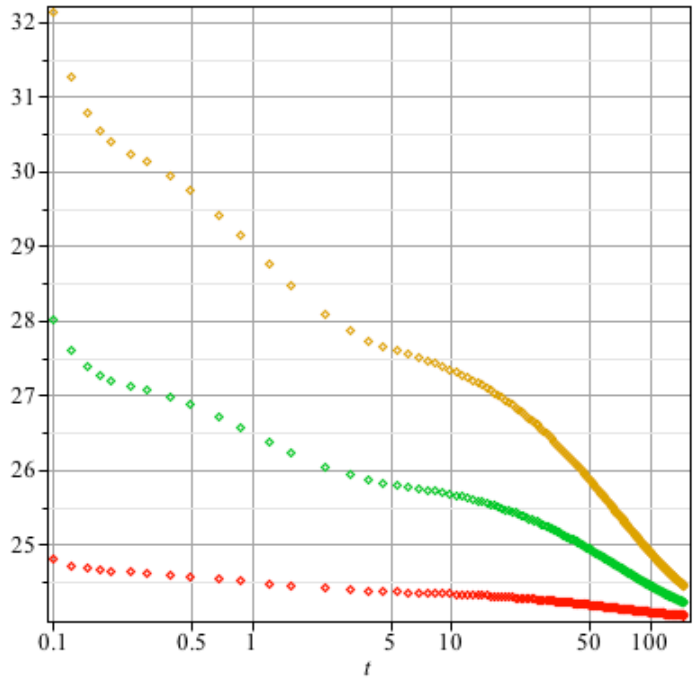

>

BIBLIOGRAPHY

BIBLIOGRAPHY

[1] P. K. Kaiser. *Luminance and brightness*. APPLIED OPTICS, 1971.

[2] G.A. Klein. *Industrial color physics*. Springer-Verlag, New York, 2010.

[3] US Energy Information Administration. *US HouseHOld Electricity Report*. 2005.

[4] A. Zukauskas. *Introduction to Solid State Lighting*. Wiley, New York, 2002.

[5] T. Smith and J. Guild. The cie colorimetric standards and their use. *TRANS. OPT. SOC.*, 33:73, 1931.

[6] W.A.Thornton. Luminosity and color-rendering capability of white light. *JOURNAL OF THE OPTICAL SOCIETY OF AMERICA*, 61:1155, 1971.

[7] P. Mottier. *LED for lighting applications*. Wiley, New York, 2009.

[8] G. Held. *Introduction to light emitting diode technology and applications*. CRC Press, 2008.

[9] J. Brodrick. Next-generation lighting initiative at the us department of energy: Catalyzing science into the marketplace. *JOURNAL OF DISPLAY TECHNOLOGY*, 3:91, 2007.

[10] R. L. Doty. Attachment a to tussing-williamson petition: Led projects. Technical report, 2008.

[11] C. W. Tang. Two-layer organic photovoltaic cell. *APPLIED PHYSICS LETTERS*, 48:183, 1986.

[12] C. W. Tang and S. VanSlyke. Organic electroluminescent diodes. *APPLIED PHYSICS LETTERS*, 51:913, 1987.

[13] H. Yersin. *Highly Efficient OLEDs with Phosphorescent Materials*. Wiley-VCH, 2007.

[14] J. Bardsley. Internaltional oled technology roadmap. *IEEE J. SELECT. TOPICS QUANTUM ELECTRON*, 10:3, 2004.

[15] C. C. Chang, C. L. Pai, W. C. Chen, and S. A. Jenekhe. Spin coating of conjugated polymers for electronic and optoelectronic applications. *THIN SOLID FILMS*, 479:254, 2005.

[16] V. Bulovic, A. Shoustikov, M. A. Baldo, E. Bose, V. G. Kozlov, M. E. Thompson, and S. R. Forrest. Bright, saturated, red-to-yellow organic light-emitting devices based on polarization-induced spectral shifts. *CHEMICAL PHYSICS LETTERS*, 287:455, 1998.

[17] C Adachi, MA Baldo, ME Thompson, and SR Forrest. Nearly 100% internal phosphorescence efficiency in an organic light-emitting device. *JOURNAL OF APPLIED PHYSICS*, 90(10):5048–5051, NOV 15 2001.

[18] L. S. Hung and C. H. Chen. Recent progress of molecular organic electroluminescent materials and devices. *MATERIS SCIENCE AND ENGINEERING R*, 39:143, 2002.

[19] H. Shirakawa, E. J. Louis, A. G. Macdiarmid, C. K. Chang, and A. J. Heeger. Synthesis of electrically conducting organic polymers-halogen derivatives of polyacetylene, (ch)x. *JOURNAL OF THE CHEMICAL SOCIETY-CHEMICAL COMMUNICATIONS*, 16:578, 1977.

[20] C. Kittel. *Introduction to Solid State Physics*. Wiley, New York, 1976.

[21] M. Pope and C. Swenberg. *Electronic Processes in Organic Crystals and Polymers*. Oxford University Press, New York, 2nd edition, 1999.

[22] F. Gutmann, L. E. Lyons, and H. Keyzer. *Organic Semiconductors*. R. E. Kreiger, Malabar, FL, 1981.

[23] P.W. Atkins and J. De Paula. *Physical Chemistry*. Oxford University Press, New York, 2006.

[24] R. L. Dekock and H. B. Gary. *Chemical structure and bonding*. University Science Books, 1989.

[25] G. S. Rohrer. *Sturcture and bonding in crystalline materials*. Cambridge University Press, 2001.

[26] I. Fleming. *Molecular orbitals and organic chemical reactions: refernce edition*. Wiley, New York, 2010.

[27] J. Farges. *Organic Conductors: Fundamentals and Applications*. Marcel Dekker, New York, 1994.

[28] A. Esptein. *Introduction to electronic polymers: Influence of nanostructure on electronic phenomena*. Springer-Verlag, New York, 2001.

[29] N. J. Turro. *Modern Molecular Photochemistry*. University Science Books, 1991.

[30] P. W. Atkins. *Quanta*. Oxford University Press, New York, 1991.

[31] P. W. Atkins. *Molecular Quantum Mechanics*. Clarendon Press, Oxford, 1970.

[32] E. A. Silinsh and V. Capek. *Organic Molecular Crystals*. American Institute of Pysics Press, New York, 1994.

[33] J. Singh and K. Shimakawa. *Advances in amorphous semiconductors (advances in condensed matter science)*. CRC Press, 2003.

[34] S. R. Forrest. The path to ubiquitous and low-cost organic electronic appliances on plastic. *NATURE*, 428:911, 2004.

[35] R. F. Salzman, J. G. Xue, B. P. Rand, A. Alexander, M. E. Thompson, and S. R. Forrest. The effects of copper phthalocyanine purity on organic solar cell performance. *ORGANIC ELECTRONICS*, 6:242, 2005.

[36] T. D. Anthopoulos and T. S. Shafal. Influence of oxygen doping on the electrical and photovoltaic properties of schottky type solar cells based on alpha-nickel phthalocyanine. *Thin Solid Films*, 441(207), 2003.

[37] S. R. Forrest. Ultrathin organic films grown by organic molecular beam deposition and related techniques. *CHEMICAL REVIEW*, 97:1793, 1997.

[38] W. G. Phann. *Zone Melting*. Wiley, New York, 1958.

[39] N. Karl. Organic semiconductors-purification and crystal growth. *MOLECULAR CRYSTALS AND LIQUID CRYSTALS*, 171:157, 1989.

[40] D. L. Smith. *Thin-Film Deposition: Principles and Practive*. McGraw-Hill, New York, 1985.

[41] M. Baldo, M. Deutsch, P. E. Burrows, H. F. Gossenberger, M. Gerstenberg, V. S. Ban, and S. R. Forrest. Organic vapor phase depostition. *ADVANCED MATERIALS*, 10:1505, 1998.

[42] M. Baldo, V. G. Kozlov, P. E. Burrows, S. R. Forrest, V. S. Ban, B. Koene, and M. E. Thompson. Low pressure organic vapor phase deposition of small molecular weight organic light emitting device structures. *APPLIED PHYSICS LETTERS*, 71:3033, 1997.

[43] M. Shtein, H. F. Gossenberger, J. B. Benziger, and S. R. Forrest. Material transport regimes and mechanisms for growth of molecular organic thin films using low-pressure organic vapor phase deposition. *JOURNAL OF APPLIED PHYSICS*, 89:1470, 2001.

[44] F. Yang, M. Shtein, and S. R. Forrest. Morphology control and material mixing by high-temperature organic vapor-phase deposition and its application to thin-film solar cells. *JOURNAL OF APPLIED PHYSICS*, 98:014906, 2005.

[45] M. Shtein, P. Peumans, J. B. Benziger, and S. R. Forrest. Direct, mask- and solvent-free printing of molecular organic semiconductors. *ADVANCED MATERIALS*, 16:1615, 2004.

[46] Y. R. Sun, M. Shtein, and S. R. Forrest. Direct patterning of organic light-emitting devices by organic-vapor jet printing. *APPLIED PHYSICS LETTERS*, 86:113504, 2005.

[47] S. Y. Chou, P. R. Krauss, and P. J. Renstrom. Imprint lithography with 25-nanometer resolution. *SCIENCE*, 272:85, 1996.

[48] R. Fabian Pease. Lithography and other pqtterning techniques for future electronics. *FELLOW IEEE*, 96(248), 2008.

[49] T. ITO and S. Okazaki. Pushing the limits of lithography. *NATURE*, 406:1027, 2000.

[50] J. Greer, A. Korkin, and J. Labanowski. *Nano and giga challenges in microelectronics*. ELSEVIER SCIENCE, 2003.

[51] C. W. Gwyn, R. Stulen, D. Sweeney, and D. Attwood. Extreme ultraviolet lithography. *J. Vac. Sci. Technol. B*, 16:3142, 1998.

[52] S. Y Chou, P. R. Krauss, and P. J. Renstrom. Nanoimprint lithography. *J. Vac. Sci. Technol. B*, 14:4129, 1998.

[53] E. Betzig and J. K. Trautman. Near-field optics: microscopy, spectroscopy, and surface modification beyond the diffraction limit. *SCIENCE*, 257:189, 1992.

[54] C. Kim, P. E. Burrows, and S. R. Forrest. Micropatterning of organic electronic devices by cold-welding. *SCIENCE*, 288:831, 2000.

[55] C. Kim. *Patterning of organic electronic devices*. PhD thesis, Princeton University, 2005.

[56] C. Kim, M Shtein, and S. R. Forrest. Nanolithography based on patterned metal transfer and its application to organic electronic devices. *APPLIED PHYSICS LETTERS*, 80:4051, 2002.

[57] J. A Rogers, Z. Bao, A. Makhija, and P. Braun. Printing process suitable for reel-to-reel production of high-performance organic transistors and circuits. *ADVANCED MATERIALS*, 11:741, 1999.

[58] L. D. Laudau and E. M. Lifshitz. *Quantum Mechanics*. Butterworth-Heinemann, NY, 3rd edition, 2003.

[59] A. Rajagopal and A. Kahn. Photoemission spectroscopy investigation of magnesium-alq(3) interfaces. *JOURNAL OF APPLIED PHYSICS*, 84:355, 1998.

[60] Gordon W. F. Drake. *Springer handbook of atomic, molecular and optical physics*. Springer, 2005.

[61] I. G. Hill, A. Kahn, J. Cornil, D. A. Santos, and J. L. Bredas. Occupied and unoccupied electronic levels in organic pi-conjugated molecules: comparison between experiment and theory. *CHEMICAL PHYSICS LETTERS*, 317:444, 2000.

[62] T. Sogimoto and K Fukutani. Electric-field-induced nuclear-spin flips mediated by enhanced spin-orbit coupling. *NATURE PHYSICS*, 7:307, 2011.

[63] J. P. Lowe. *Quantum Chemistry*. Academic Press, NY, 2nd edition, 1993.

[64] R. Daudel, G. Leroy, D. Peeters, and M. Sana. *Quantum Chemistry*. Wiley, New York, 2nd edition, 1983.

[65] MA Baldo, DF O'Brien, Y You, A Shoustikov, S Sibley, ME Thompson, and SR Forrest. Highly efficient phosphorescent emission from organic electroluminescent devices. *NATURE*, 395(6698):151–154, SEP 10 1998.

[66] J. R. Lakowicz. *Principles of fluorescence spectroscopy*. Springer, 3rd edition, 2006.

[67] MA Baldo, ME Thompson, and SR Forrest. High-efficiency fluorescent organic light-emitting devices using a phosphorescent sensitizer. *NATURE*, 403(6771):750–753, FEB 17 2000.

[68] K. Harada, A. G. Werner, M. Pfeiffer, C. J. Bloom, C. M. Elliott, and K. Leo. Organic homojunction diodes with a high built-in potential: Interpretation of the current-voltage characteristics by a generalized einstein relation. *PHYSICAL REVIEW LETTERS*, 94:036601, 2005.

[69] R. Farchioni and G. Grosso. *Organic electronic materials: conjugated polymers and low molecular weight organic solids (Springer series in materials science)*. Springer, 2001.

[70] T. Forster. *Delocalized excitation and excitation transfer in modern quantum chemistry*. Academic Press, NY, 1965.

[71] D. L. Dexter. A theory of sensitized luminescence in solids. *JOURNAL OF CHEMICAL PHYSICS*, 21:836, 1953.

[72] K. Itano, H. Ogawa, and Y. Shirota. Exciplex formation at the organic solid-state interface: Yellow emission in organic light-emitting diodes using green-fluorescent tris(8-quinolinolato)aluminum and hole-transporting molecular materials with low ionization potentials. *APPLIED PHYSICS LETTERS*, 72:1998, 1997.

[73] J. A. Osaheni and S. A. Jenekhe. Efficient blue luminescence of a conjugated polymer exciplex. *MACROMOLECULES*, 27:739, 1994.

[74] F. Hirayama. Intramolecular excimer formation. i. diphenyl and triphenyl alkanes. *JOURNAL OF CHEMICAL PHYSICS*, 42:3163, 1964.

[75] J Brooks, Y Babayan, S Lamansky, PI Djurovich, I Tsyba, R Bau, and ME Thompson. Synthesis and characterization of phosphorescent cyclometalated platinum complexes. *INORGANIC CHEMISTRY*, 41(12):3055–3066, JUN 17 2002.

[76] WY Wong, Z He, SK So, KL Tong, and ZY Lin. A multifunctional platinum-based triplet emitter for OLED applications. *ORGANOMETALLICS*, 24(16):4079–4082, AUG 1 2005.

[77] Ze He, Wai-Yeung Wong, Xiaoming Yu, Hoi-Sing Kwok, and Zhenyang Lin. Phosphorescent platinum(II) complexes derived from multifunctional chromophores: Synthesis, structures, photophysics, and electroluminescence. *INORGANIC CHEMISTRY*, 45(26):10922–10937, DEC 25 2006.

[78] BW Ma, J Li, PI Djurovich, M Yousufuddin, R Bau, and ME Thompson. Synthetic control of Pt center dot center dot center dot Pt separation and photophysics of binuclear platinum complexes. *JOURNAL OF THE AMERICAN CHEMICAL SOCIETY*, 127(1):28–29, JAN 12 2005.

[79] SW Lai, MCW Chan, KK Cheung, SM Peng, and CM Che. Synthesis of organoplatinum oligomers by employing N-donor bridges with predesigned geometry: Structural and photophysical properties of luminescent cyclometalated platinum(II) macrocycles. *ORGANOMETALLICS*, 18(20):3991–3997, SEP 27 1999.

[80] Biwu Ma, Peter I. Djurovich, Simona Garon, Bert Alleyne, and Mark E. Thompson. Platinum binuclear complexes as phosphorescent dopants for monochromatic and white organic light-emitting diodes. *ADVANCED FUNCTIONAL MATERIALS*, 16(18):2438–2446, DEC 4 2006.

[81] Masako Kato. Luminescent platinum complexes having sensing functionalities. *BULLETIN OF THE CHEMICAL SOCIETY OF JAPAN*, 80(2):287–294, FEB 15 2007.

[82] SW Lai, HW Lam, W Lu, KK Cheung, and CM Che. Observation of low-energy metal-metal-to-ligand charge transfer absorption and emission: Electronic spectroscopy of cyclometalated platinum(II) complexes with isocyanide ligands. *ORGANOMETALLICS*, 21(1):226–234, JAN 7 2002.

[83] T Koshiyama, A Omura, and M Kato. Redox-controlled luminescence of a cyclometalated dinuclear platinum complex bridged with pyridine-2-thiolate ions. *CHEMISTRY LETTERS*, 33(10):1386–1387, OCT 5 2004.

[84] Frank Neese. Importance of direct spin-spin coupling and spin-flip excitations for the zero-field splittings of transition metal complexes: A case study. *JOURNAL OF THE AMERICAN CHEMICAL SOCIETY*, 128(31):10213–10222, AUG 9 2006.

[85] WJ Finkenzeller and H Yersin. Emission of Ir(ppy)3. Temperature dependence, decay dynamics, and magnetic field properties. *CHEMICAL PHYSICS LETTERS*, 377(3-4):299–305, AUG 15 2003.

[86] RJ Holmes, BW D'Andrade, SR Forrest, X Ren, J Li, and ME Thompson. Efficient, deep-blue organic electrophosphorescence by guest charge trapping. *APPLIED PHYSICS LETTERS*, 83(18):3818–3820, NOV 3 2003.

[87] MA Baldo, C Adachi, and SR Forrest. Transient analysis of organic electrophosphorescence. II. Transient analysis of triplet-triplet annihilation. *PHYSICAL REVIEW B*, 62(16):10967–10977, OCT 15 2000.

[88] WJ Finkenzeller, P Stossel, and H Yersin. Emission and absorption of Ir(ppy)(2)(CO)(Cl) - temperature dependence, phosphorescence decay dynamics, and assignment of excited states. *CHEMICAL PHYSICS LETTERS*, 397(4-6):289–295, OCT 21 2004.

[89] H Yersin. Organometallic triplet emitters for OLED applications. Controlling of emission properties by chemical variation. In Kafafi, ZH and Lane, PA, editor, *ORGANIC LIGHT-EMITTING MATERIALS AND DEVICES VII*, volume 5214 of *PROCEEDINGS OF THE SOCIETY OF PHOTO-OPTICAL INSTRUMENTATION ENGINEERS (SPIE)*, pages 124–132, 2004. Conference on Organic Light-Emitting Materials and Devices VII, San Diego, CA, AUG 04-06, 2003.

[90] D. R. Stripling and G. A. Crosby. Excited-states of homonuclear-bridged and heteronuclear-bridged bimetallic complexes of Rhodium(I), Iridium(I), Platinum(II), and gold(I) - triplet manifold splittings, state assignments, and symmetry correlations. *JOURNAL OF PHYSICAL CHEMISTRY*, 99(20):7977–7984, MAY 18 1995.

[91] R. H. Fowler and L. Nordheim. Electron emission in intense electric field. *PROCEEDINGS OF THE ROYAL SOCIETY OF LONDON. SERIES A*, 119:173, 1928.

[92] E. L. Murphy and R. H. Fowler. Thermionic emission, field emission, and the transition region. *PHYSICAL REVIEW*, 102:1464, 1956.

[93] W. D. Gill. Drift mobilities in amorphous charge-transfer complexes of trinitrofluorenone and poly-n-vinylcarbazole. *JOURNAL OF APPLIED PHYSICS*, 43:5033, 1972.

[94] K. C. Kao and W. Hwang. *Electrical Transport in Solids*. Pergamon Press, Oxford, 1981.

[95] G. A. Crosby and J. N. Demas. Quantum efficiencies on transition metal complexes. ii. charge transfer luminescence. *J. AM. CHEM. SOC.*, 93:2841, 1971.

[96] T. J. Meyer. Photochemistry of metal coordination complexes: metal to ligand charge transfer excited states. *PURE AND APPL. CHEM.*, 58:1193, 1986.

[97] J. Kalinowski, L. C. Picciolo, H. Murata, and Z. H. Kafafi. Effect of emitter disorder on the recombination zone and the quantum yield of organic electroluminescent diodes. *JOURNAL OF APPLIED PHYSICS*, 89:1866, 2001.

[98] I. Juric, I. Batistic, and E. Tutis. Recombination at heterojunctions in disordered organic media: Modeling and numerical simulations. *PHYSICAL REVIEW B*, 77:165304, 2008.

[99] BW D'Andrade and SR Forrest. White organic light-emitting devices for solid-state lighting. *ADVANCED MATERIALS*, 16(18):1585–1595, SEP 16 2004.

[100] JH Jou, MC Sun, HH Chou, and CH Li. Efficient pure-white organic light-emitting diodes with a solution-processed, binary-host employing single emission layer. *APPLIED PHYSICS LETTERS*, 88(14), APR 3 2006.

[101] BW D'Andrade, RJ Holmes, and SR Forrest. Efficient organic electrophosphorescent white-light-emitting device with a triple doped emissive layer. *ADVANCED MATERIALS*, 16(7):624+, APR 5 2004.

[102] Ji Hoon Seo, Il Houng Park, Gu Young Kim, Kum Hee Lee, Min Kyu Kim, Seung Soo Yoon, and Young Kwan Kim. Hybrid spacer for high-efficiency white organic light-emitting diodes. *APPLIED PHYSICS LETTERS*, 92(18), MAY 5 2008.

[103] Yiru Sun and Stephen R. Forrest. High-efficiency white organic light emitting devices with three separate phosphorescent emission layers. *APPLIED PHYSICS LETTERS*, 91(26), DEC 24 2007.

[104] Hiroshi Kanno, Noel C. Giebink, Yiru Sun, and Stephen R. Forrest. Stacked white organic light-emitting devices based on a combination of fluorescent and phosphorescent emitters. *APPLIED PHYSICS LETTERS*, 89(2), JUL 10 2006.

[105] H Kanno, RJ Holmes, Y Sun, S Kena-Cohen, and SR Forrest. White stacked electrophosphorescent organic light-emitting devices employing MoO3 as a charge-generation layer. *ADVANCED MATERIALS*, 18(3):339+, FEB 3 2006.

[106] ZL Shen, PE Burrows, V Bulovic, SR Forrest, and ME Thompson. Three-color, tunable, organic light-emitting devices. *SCIENCE*, 276(5321):2009–2011, JUN 27 1997.

[107] J Drechsel, M Pfeiffer, X Zhou, A Nollau, and K Leo. Organic Mip-diodes by p-doping of amorphous wide-gap semiconductors: CV and impedance spectroscopy. *SYNTHETIC METALS*, 127(1-3, Sp. Iss. SI):201–205, MAR 26 2002. E-MRS 2001 Spring Meeting, STRASBOURG, FRANCE, JUN 05-08, 2001.

[108] X. D. Gao, J. Zhou, Z. T. Xie, B. F. Ding, Y. C. Qian, X. M. Ding, and X. Y. Hou. Mechanism of charge generation in p-type doped layer in the connection unit of tandem-type organic light-emitting devices. *APPLIED PHYSICS LETTERS*, 93(8), AUG 25 2008.

[109] C. W. Law, K. M. Lau, M. K. Fung, M. Y. Chan, F. L. Wong, C. S. Lee, and S. T. Lee. Effective organic-based connection unit for stacked organic light-emitting devices. *APPLIED PHYSICS LETTERS*, 89(13), SEP 25 2006.

[110] Tae-Woo Lee, Taeyong Noh, Byoung-Ki Choi, Myeong-Suk Kim, Dong Woo Shin, and Junji Kido. High-efficiency stacked white organic light-emitting diodes. *APPLIED PHYSICS LETTERS*, 92(4), JAN 28 2008.

[111] Henk J. Bolink, Eugenio Coronado, Diego Repetto, Michele Sessolo, Eva M. Barea, Juan Bisquert, Germa Garcia-Belmonte, Jan Prochazka, and Ladislav Kavan. Inverted solution processable OLEDs using a metal oxide as an electron injection contact. *ADVANCED FUNCTIONAL MATERIALS*, 18(1):145–150, JAN 11 2008.

[112] G Parthasarathy, C Shen, A Kahn, and SR Forrest. Lithium doping of semiconducting organic charge transport materials. *JOURNAL OF APPLIED PHYSICS*, 89(9):4986–4992, MAY 1 2001.

[113] N. C. Giebink and S. R. Forrest. Quantum efficiency roll-off at high brightness in fluorescent and phosphorescent organic light emitting diodes. *PHYSICAL REVIEW B*, 77(23), JUN 2008.

[114] Xiangfei Qi, Michael Slootsky, and Stephen Forrest. Stacked white organic light emitting devices consisting of separate red, green, and blue elements. *APPLIED PHYSICS LETTERS*, 93(19), NOV 10 2008.

[115] J Kido, T Matsumoto, T Nakada, J Endo, K Mori, N Kawamura, and A Yokoi. High efficiency organic el devices having charge generation layers. *SID INT SYMP DIG TECH PAPER*, 34:964, 2003.

[116] LS Liao, KP Klubek, and CW Tang. High-efficiency tandem organic light-emitting diodes. *APPLIED PHYSICS LETTERS*, 84(2):167–169, JAN 12 2004.

[117] TY Cho, CL Lin, and CC Wu. Microcavity two-unit tandem organic light-emitting devices having a high efficiency. *APPLIED PHYSICS LETTERS*, 88(11), MAR 13 2006.

[118] Dong-Seok Leem, Jae-Hyun Lee, Jang-Joo Kim, and Jae-Wook Kang. Highly efficient tandem p-i-n organic light-emitting diodes adopting a low temperature evaporated rhenium oxide interconnecting layer. *APPLIED PHYSICS LETTERS*, 93(10), SEP 8 2008.

[119] CC Chang, JF Chen, SW Hwang, and CH Chen. Highly efficient white organic electroluminescent devices based on tandem architecture. *APPLIED PHYSICS LETTERS*, 87(25), DEC 19 2005.

[120] CW Chen, YJ Lu, CC Wu, EHE Wu, CW Chu, and Y Yang. Effective connecting architecture for tandem organic light-emitting devices. *APPLIED PHYSICS LETTERS*, 87(24), DEC 12 2005.

[121] JZ Li, M Yahiro, K Ishida, H Yamada, and K Matsushige. Enhanced performance of organic light emitting device by insertion of conducting/insulating WO3 anodic buffer layer. *SYNTHETIC METALS*, 151(2):141–146, JUN 14 2005.

[122] Michael Kroger, Sami Hamwi, Jens Meyer, Thomas Dobbertin, Thomas Riedl, Wolfgang Kowalsky, and Hans-Hermann Johannes. Temperature-independent field-induced charge separation at doped organic/organic interfaces: Experimental modeling of electrical properties. *PHYSICAL REVIEW B*, 75(23), JUN 2007.

[123] CC Chang, SW Hwang, CH Chen, and JF Chen. High-efficiency organic electroluminescent device with multiple emitting units. *JAPANESE JOURNAL OF APPLIED PHYSICS PART 1-REGULAR PAPERS SHORT NOTES & REVIEW PAPERS*, 43(9A):6418–6422, SEP 2004.

[124] T Tsutsui and M Terai. Electric field-assisted bipolar charge spouting in organic thin-film diodes. *APPLIED PHYSICS LETTERS*, 84(3):440–442, JAN 19 2004.

[125] Benjamin Krummacher, Mathew K. Mathai, Vi-En Choong, Stellos A. Choulis, Franky So, and Albrecht Winnacker. Influence of charge balance and microcavity effects on resultant efficiency of organic-light emitting devices. *ORGANIC ELECTRONICS*, 7(5):313–318, OCT 2006.

[126] S. Fleischer, P. T. Lai, and Y. C. Cheng. simplied closed-form trap-assisted tunneling model applied to nitrided oxide dielectric capacitors. *JOURNAL OF APPLIED PHYSICS*, 72(12):5711–5715, DEC 15 1992.

[127] DM Sathaiya and S Karmalkar. Thermionic trap-assisted tunneling model and its application to leakage current in nitrided oxides and AlGaN/GaN high electron mobility transistors. *JOURNAL OF APPLIED PHYSICS*, 99(9), MAY 1 2006.

[128] TW Hickmott. Temperature-dependent Fowler-Nordheim tunneling and a composition effect in anodized Al-Al2O2-Au diodes. *JOURNAL OF APPLIED PHYSICS*, 97(10, Part 1), MAY 15 2005.

[129] C Adachi, MA Baldo, SR Forrest, S Lamansky, ME Thompson, and RC Kwong. High-efficiency red electrophosphorescence devices. *APPLIED PHYSICS LETTERS*, 78(11):1622–1624, MAR 12 2001.

[130] B Ruhstaller, SA Carter, S Barth, H Riel, W Riess, and JC Scott. Transient and steady-state behavior of space charges in multilayer organic light-emitting diodes. *JOURNAL OF APPLIED PHYSICS*, 89(8):4575–4586, APR 15 2001.

[131] K Sugiyama, H Ishii, Y Ouchi, and K Seki. Dependence of indium-tin-oxide work function on surface cleaning method as studied by ultraviolet and x-ray photoemission spectroscopies. *JOURNAL OF APPLIED PHYSICS*, 87(1):295–298, JAN 1 2000.

[132] Toshinori Matsushima, Guang-He Jin, and Hideyuki Murata. Marked improvement in electroluminescence characteristics of organic light-emitting diodes using an ultrathin hole-injection layer of molybdenum oxide. *JOURNAL OF APPLIED PHYSICS*, 104(5), SEP 1 2008.

[133] M. Kroeger, S. Hamwi, J. Meyer, T. Riedl, W. Kowalsky, and A. Kahn. Role of the deep-lying electronic states of MoO3 in the enhancement of hole-injection in organic thin films. *APPLIED PHYSICS LETTERS*, 95(12), SEP 21 2009.

[134] Ning Li, Brian E. Lassiter, Richard R. Lunt, Guodan Wei, and Stephen R. Forrest. Open circuit voltage enhancement due to reduced dark current in small molecule photovoltaic cells. *APPLIED PHYSICS LETTERS*, 94(2), JAN 12 2009.

[135] SR Forrest, DDC Bradley, and ME Thompson. Measuring the efficiency of organic light-emitting devices. *ADVANCED MATERIALS*, 15(13):1043–1048, JUL 4 2003.

[136] R. S. Muller and T. I. Kamins. *Device Electronics for Integrated Circuits*. Wiley, New York, 2002.

[137] Frank Lindner, Karsten Walzer, and Karl Leo. Organic heterostructure device with nonvolatile memory behavior using electrically doped layers. *APPLIED PHYSICS LETTERS*, 93(23), DEC 8 2008.

[138] Kenji Nakamura, Takuya Hata, Atsushi Yoshizawa, Katsunari Obata, Hiroyuki Endo, and Kazuhiro Kudo. Metal-insulator-semiconductor-type organic light-emitting transistor on plastic substrate. *APPLIED PHYSICS LETTERS*, 89(10), SEP 4 2006.

[139] B. L. Anderson and R. L. Anderson. *Fundamentals of Semiconductor Devices*. McGraw-Hill, New York, 2004.

[140] Y Matsuo, T Suzuki, Y Yokoi, and S Ikehata. Stage structure in cesium doped pentacene. *JOURNAL OF PHYSICS AND CHEMISTRY OF SOLIDS*, 65(2-3):619–621, FEB-MAR 2004. 12th International Symposium on Intercalation Compounds, POZNAN, POLAND, JUN 01-05, 2003.

[141] M. G. Helander, Z. B. Wang, J. Qiu, and Z. H. Lu. Band alignment at metal/organic and metal/oxide/organic interfaces. *APPLIED PHYSICS LETTERS*, 93(19), NOV 10 2008.

[142] MA Baldo, S Lamansky, PE Burrows, ME Thompson, and SR Forrest. Very high-efficiency green organic light-emitting devices based on electrophosphorescence. *APPLIED PHYSICS LETTERS*, 75(1):4–6, JUL 5 1999.

[143] H Benisty, R Stanley, and M Mayer. Method of source terms for dipole emission modification in modes of arbitrary planar structures. *JOURNAL OF THE OPTICAL SOCIETY OF AMERICA A-OPTICS IMAGE SCIENCE AND VISION*, 15(5):1192–1201, MAY 1998.

[144] Michael Kroger, Sami Hamwi, Jens Meyer, Thomas Riedl, Wolfgang Kowalsky, and Antoine Kahn. P-type doping of organic wide band gap materials by transition metal oxides: A case-study on Molybdenum trioxide. *ORGANIC ELECTRONICS*, 10(5):932–938, AUG 2009.

[145] V Bhosle, A Tiwari, and J Narayan. Epitaxial growth and properties of MoOx films. *JOURNAL OF APPLIED PHYSICS*, 97(8), APR 15 2005.

[146] MAKL DISSANAYAKE and LL CHASE. OPTICAL-PROPERTIES OF CRO2, MOO2, AND WO2 IN THE RANGE 0.2-6 EV. *PHYSICAL REVIEW B*, 18(12):6872–6879, 1978.

[147] Po-Sheng Wang, I-Wen Wu, Wei-Hsuan Tseng, Mei-Hsin Chen, and Chih-I Wu. Enhancement of current injection in organic light emitting diodes with sputter treated molybdenum oxides as hole injection layers. *APPLIED PHYSICS LETTERS*, 98(17), APR 25 2011.

[148] Irfan, Huanjun Ding, Yongli Gao, Do Young Kim, Jegadesan Subbiah, and Franky So. Energy level evolution of molybdenum trioxide interlayer between indium tin oxide and organic semiconductor. *APPLIED PHYSICS LETTERS*, 96(7), FEB 15 2010.

[149] Maria Vasilopoulou, Leonidas C. Palilis, Dimitra G. Georgiadou, Panagiotis Argitis, Stella Kennou, Labrini Sygellou, Ioannis Kostis, Giorgos Papadimitropoulos, Nikos Konofaos, Agis A. Iliadis, and Dimitris Davazoglou. Reduced molybdenum oxide as an efficient electron injection layer in polymer light-emitting diodes. *APPLIED PHYSICS LETTERS*, 98(12), MAR 21 2011.

[150] H Al-Kandari, F Al-Kharafi, N Al-Awadi, OM El-Dusouqui, SA Ali, and A Katrib. The catalytic active sites in partially reduced MoO3 for the hydroisomerization of 1-pentene and n-pentane. *APPLIED CATALYSIS A-GENERAL*, 295(1):1–10, 2005.

[151] H. Aziz, Z. D. Popovic, and N. Hu. Organic light emitting devices with enhanced operational stability at elevated temperatures. *APPLIED PHYSICS LETTERS*, 81:370, 2002.

[152] JC Sturm, F Pschenitzka, TR Hebner, MH Lu, CC Wu, and W Wilson. Patterning approaches and system power efficiency considerations for organic LED displays. In Kafafi, ZH, editor, *ORGANIC LIGHT-EMITTING MATERIALS AND DEVICES II*, volume 3476 of *PROCEEDINGS OF THE SOCIETY OF PHOTO-OPTICAL INSTRUMENTATION ENGINEERS (SPIE)*, pages 208–216, 1998. Conference on Organic Light-Emitting Materials and Devices II, SAN DIEGO, CA, JUL 21-23, 1998.

[153] J. W. Park, D. C. Shin, and S. H. Park. Large-area OLED lightings and their applications. *SEMICONDUCTOR SCIENCE AND TECHNOLOGY*, 26(3), MAR 2011.

[154] Seungjun Chung, Jae-Hyun Lee, Jaewook Jeong, Jang-Joo Kim, and Yongtaek Hong. Substrate thermal conductivity effect on heat dissipation and lifetime improvement of organic light-emitting diodes. *APPLIED PHYSICS LETTERS*, 94(25), JUN 22 2009.

[155] C. Gaerditz, A. Winnacker, F. Schindler, and R. Paetzold. Impact of Joule heating on the brightness homogeneity of organic light emitting devices. *APPLIED PHYSICS LETTERS*, 90(10), MAR 5 2007.

[156] Pipes L. A. Matrix analysis of heat transfer problems. *JOURNAL OF THE FRANKLIN INSTITUTE*, 263:195, 1957.

[157] H Kim, CM Gilmore, A Pique, JS Horwitz, H Mattoussi, H Murata, ZH Kafafi, and DB Chrisey. Electrical, optical, and structural properties of indium-tin-oxide thin films for organic light-emitting devices. *JOURNAL OF APPLIED PHYSICS*, 86:6451, 1999.

[158] H Kim, A Pique, JS Horwitz, H Mattoussi, H Murata, ZH Kafafi, and DB Chrisey. Indium tin oxide thin films for organic light-emitting devices. *APPLIED PHYSICS LETTERS*, 74:3444, 1999.

[159] V Bulovic, VB Khalfin, G Gu, PE Burrows, DZ Garbuzov, and SR Forrest. Weak microcavity effects in organic light-emitting devices. *PHYSICAL REVIEW B*, 58:3730, 1998.

[160] I. Hatta. Heat-capacity measurements by means of thermal relaxation method in medium temperature-range. *REVIEW OF SCIENTIFIC INSTRUMENTS*, 50:292, 1979.

[161] EW Lemmon and RT Jacobsen. Viscocity and thermal conductivity equations for nitrogen, oxygen, argon, and air. *INTERNATIONAL JOURNAL OF THERMOPHYSICS*, 25:21, 2004.

[162] W. H. Tanttila. Anomalous thermal-properties of glasses. *PHYSICAL REVIEW LETTERS*, 39:554, 1977.

[163] T Yagi, K Tamano, Y Sato, N Taketoshi, T Baba, and Y Shigesato. Analysis on thermal properties of tin doped indium oxide films by picosecond thermoreflectance measurement. *JOURNAL OF VACUUM SCIENCE AND TECHNOLOGY A*, 23:1180, 2005.

[164] H. Lee. Rapid measurement of thermal-conductivity of polymer-films. *REVIEW OF SCIENTIFIC INSTRUMENTS*, 53:884, 1982.

[165] T. E. Pochapsky. Heat capacity and resistance measurements for aluminum and lead wires. *ACTA METALLURGICA*, 1:747, 1953.

[166] AL Woodcraft. Recommended values for the thermal conductivity of aluminium of different purities in the cryogenic to room temperature range, and a comparison with copper. *CRYOGENICS*, 45(626), 2005.

[167] R Codina. On stabilized finite element methods for linear systems of convection-diffusion-reaction equations. *COMPUTER METHODS IN APPLIED MECHANICS AND ENGINEERING*, 188:61, 2000.

[168] Y. Jin, A. Yadav, K. Sun, H. Sun, K. P. Pipe, and M. Shtein. Thermal boundary resistance of copper phthalocyanine-metal interface. *APPLIED PHYSICS LETTERS*, 98:093305, 2011.

[169] K. Ramadan and M. A. Al-Nimr. Analysis of transient heat transfer in multilayer thin films with nonlinear thermal boundary resistance. *INTERNATIONAL JOURNAL OF THERMAL SCIENCES*, 48:1718, 2009.

[170] Toshinori Matsushima and Chihaya Adachi. Observation of extremely high current densities on order of ma/cm(2) in copper phthalocyanine thin-film devices with submicron active areas. *JAPANESE JOURNAL OF APPLIED PHYSICS PART 2-LETTERS AND EXPRESS LETTERS*, 46:L1179, 2007.

[171] R. Meerheim, B. Lussen, and K. Leo. Efficiency and stability of p-i-n type organic light emitting diodes for display and lighting applications. *PROCEEDINGS OF THE IEEE*, 97:1606, 2009.

[172] J. Blochwitz, T. Fritz, M. Pfeiffer, K. Leo, D. M. Alloway, P. A. Lee, and N. R. Armstrong. Interface electronic structure of organic semiconductors wit controlled doping levels. *ORGANIC ELECTRONICS*, 2:97, 2001.

[173] G. Schwartz, M. Pfeiffer, S. Reineke, K. Walzer, and K. Leo. Harvesting triplet excitons from fluorescent blue emitters in white organic light-emitting diodes. *ADVANCED MATERIALS*, 19:3672, 2007.

[174] Y. Sun and S. Forrest. Enhanced light out-coupling of organic light-emitting devices using embedded low-index grids. *NATURE*, 2:483, 2008.

[175] T. Tsutsui, M. Yahiro, H. Yokogawa, and K. Kawano. Organic light-emitting device with an ordered monolayer of silica microspheres as a scattering medium. *ADVANCED MATERIALS*, 13:1149, 2001.

[176] P. A. Levermore, A. B. Dyatkin, Z. Elshenawy, H. Pang, J. Silvernail, E. Krall, R. C. Kwong, R Ma, M. S. Weaver, J. J. Brown, X. Qi, and S. R. Forrest. Phosphorescent oleds for high efficacy long lifetime solid state lighting. *SPIE 2011 proceeding to Journal of Photonic for Energy*, 2011 (submitted).

[177] C Zhang and Ding G. A stable series expansion method for calculating thermal response factors of multi-layer walls. *BUILDING AND ENVIRONMENT*, 38:669, 2003.